

1

High Energy Resummation at Hadronic 2 Colliders



3

Jack J. Medley

4 A thesis submitted in fulfilment of the requirements
5 for the degree of Doctor of Philosophy
6 to the
7 University of Edinburgh

8 March 2016

⁹ Abstract

¹⁰ Abstract abstract abstract abstract abstract abstract abstract abstract abstract
¹¹ abstract abstract abstract abstract abstract abstract abstract abstract abstract
¹² abstract abstract abstract abstract abstract abstract abstract abstract abstract
¹³ abstract abstract abstract abstract abstract abstract abstract abstract abstract
¹⁴ abstract abstract abstract abstract abstract abstract abstract abstract abstract
¹⁵ abstract abstract abstract abstract abstract abstract abstract abstract abstract
¹⁶ abstract abstract abstract abstract abstract abstract abstract abstract abstract
¹⁷ abstract abstract abstract abstract abstract abstract abstract abstract abstract
¹⁸ abstract abstract abstract abstract.

¹⁹ Declaration

²⁰ Except where otherwise stated, the research undertaken in this thesis was the unaided
²¹ work of the author. Where the work was done in collaboration with others, a significant
²² contribution was made by the author.

²³

J. Medley

²⁴

March 2016

²⁵ Acknowledgements

²⁶ Cheers guys!

Contents

²⁷	Abstract	i
²⁸	Declaration	ii
²⁹	Acknowledgements	iv
³⁰	Contents	vi
³¹	List of figures	x
³²	List of tables	xiii
³³		
³⁴	1 Introduction	1
³⁵	1.1 A Little History	1
³⁶	1.2 Thesis Outline	2
³⁷	2 Quantum Chromodynamics at hadronic colliders	5
³⁸	2.1 The QCD Lagrangian	5
³⁹	2.2 The Partonic Cross-Section	7
⁴⁰	2.3 Divergences and Regularisation	12
⁴¹	2.3.1 Ultraviolet divergences	12
⁴²	2.3.2 Infrared and collinear divergences	13
⁴³	2.3.3 Regularising divergences	14
⁴⁴	2.4 Renormalising the QCD Lagrangian	15
⁴⁵	2.5 The QCD Beta function	15
⁴⁶	2.6 QCD Factorisation at Hadronic Colliders	17
⁴⁷	2.7 From Partons to Jets	18
⁴⁸	2.8 Perturbative QCD and Resummation	20
⁴⁹	2.8.1 Fixed-order Perturbation	20
⁵⁰	2.8.2 An Example Fixed-Order Calculation	21
⁵¹	2.8.3 Resumming Higher-Order Corrections	34
⁵²	2.9 Parton showers for Monte-Carlo generators	35
⁵³	2.10 Spinor-Helicity Notation	35
⁵⁴	2.10.1 Spinor-Helicity Calculations with Massive Partons	37
⁵⁵	2.11 Monte Carlo Techniques	42
⁵⁶	2.11.1 One Dimensional Integration	42

57	2.11.2 Higher Dimensional Integration	44
58	2.11.3 Variation Reduction Techniques	45
59	3 High Energy QCD	51
60	3.1 The High Energy Limit of $2 \rightarrow 2$ QCD scattering	51
61	3.1.1 Mandelstam Variables in the High Energy Limit	51
62	3.1.2 HE limit of the three-gluon vertex	52
63	3.1.3 At Leading Order in α_s	52
64	3.1.4 At Next-to-Leading Order in α_s	53
65	3.1.5 High Energy Jets ‘Currents’	53
66	3.1.6 Effective Vertices For Real Emissions	53
67	3.2 High Energy Jets	53
68	3.2.1 The Multi-Regge Kinematic limit of QCD amplitudes	53
69	3.2.2 Logarithms in HEJ observables	53
70	3.2.3 HEJ currents	53
71	3.2.4 High Energy Phase-space Integration	53
72	4 Z/γ^*+Jets at the LHC	55
73	4.1 Z -jets	57
74	4.1.1 Formulation in terms of currents	60
75	4.1.2 To High Multiplicity Final States	60
76	4.1.3 Z^0 Emission Interference	60
77	4.1.4 Photonic Interference	60
78	4.1.5 The $2 \rightarrow n$ Matrix Element	60
79	4.1.6 The Differential Z/γ Cross-Section	60
80	4.2 Regularising the Z/γ^* +Jets Matrix Element	60
81	4.2.1 Soft Emissions	60
82	4.2.2 $V^2(q_{tj}, q_{t(j+1)})$ Terms	61
83	4.2.3 $V(q_{ti}, q_{t(i+1)}) \cdot V(q_{bi}, q_{b(i+1)})$ Terms	62
84	4.2.4 Integration of soft diverences	63
85	4.2.5 Virtual Emissions	64
86	4.2.6 Cancellation of Infrared Contributions	65
87	4.2.7 Example: $2 \rightarrow 4$ Scattering	68
88	4.3 Subtractions and the λ_{cut} scale	70
89	4.4 Z/γ^* +Jets at the ATLAS Experiment	70
90	4.4.1 CMS - Z + Jets Measurements	75
91	5 High Multiplicity Jets at ATLAS	79
92	6 The W^\pm to Z/γ^* Ratio at ATLAS	85
93	7 Z/γ^*+Jets at 100TeV	87
94	8 Conclusions and Outlook	95
95	A The Faddeev-Popov Trick	97

CONTENTS

96	Bibliography	99
97	Publications	102

CONTENTS

List of Figures

<p>99 2.1 The evolution of α_s over several orders of magnitude in the scale of 100 the process Q^2. The data points fitted are of varying degrees of formal 101 accuracy ranging from next-to-leading order in α_s (NLO) to next-to- 102 next-to-next-to-leading order in α_s (N^3LO). Fig. from [20].</p> <p>103 2.2 Simulations of the average number of jets as a function of the sum of the 104 transverse momenta in the event, H_T, for inclusive dijets at a 7TeV LHC. 22</p> <p>105 2.3 Feynman diagrams for calculating the $O(\alpha_s)$ correction to $\gamma^* \rightarrow q\bar{q}$. Fig. 106 (2.3a) is the leading order contribution. Figs. (2.3b - 2.3d) are the virtual 107 corrections and lastly figs. (2.3e - 2.3f) are the real emission contributions. 23</p> <p>108 2.4 The ratio of the inclusive Higgs plus three jet cross-section to inclusive 109 Higgs plus two jet cross-section shown for centre-of-mass energies of 110 14TeV (similar to the current LHC), 33TeV and 100TeV (possible energy 111 scales for a hadronic future circular collider).</p> <p>112 2.5 A simple importance sampling example (see equation 2.126). The 113 integrand, $f(x)$, is shown in blue, the importance sampling distribution 114 is shown in green and, for comparison, the uniform probability density 115 function used in the naive case of no importance sampling is also shown 116 (in red).</p> <p>117 2.6 The absolute value squared of the Z^0 propagator for a range of values 118 of the invariant mass squared of the Z^0, p_Z^2. We can see it is strongly 119 peaked at the Z^0 mass and, as such, is an ideal candidate for using 120 importance sampling.</p> <p>121 2.7 Recent parton distribution function fits from the HERA experiment. 122 The observed variation in $f(x_{a/b}, Q^2)$, especially at high $x_{a/b}$, can be 123 exploited when computing the equation ?? by using an importance 124 sampling approach</p> <p>125 4.1 The possible emission sites for a neutral weak boson.</p> <p>126 4.2 Examples of diagrams contributing to $2 \rightarrow 4$ scattering. In fig. 4.2a 127 the p_2 has been drawn with a dashed line to denote it is not resolvable. 128 In fig. 4.2b the final state momenta have been labelled in a seemingly 129 strange way - this was done to make clear the cancellation when working 130 through the algebra.</p>	<p>17</p> <p>22</p> <p>23</p> <p>36</p> <p>47</p> <p>48</p> <p>49</p> <p>58</p> <p>89</p>
--	---

LIST OF FIGURES

131	4.3	The effect of varying λ_{cut} on the differential distribution in the rapidity gap between the two leading jets in p_T with the $N_{jet} = 2, 3, 4$ exclusive selections shown from left to right. $\lambda_{cut} = 0.2$ (red), 0.5 (blue), 1.0 (green), 2.0 (purple).	71
132	4.4	These plots show the inclusive jet rates from (a) HEJ and (b) other theory descriptions and data [3]. HEJ events all contain at least two jets and do not contain matching for 5 jets and above, so these bins are not shown.	74
133	4.5	These plots show the invariant mass between the leading and second-leading jet in p_T . As in Fig. 4.4, predictions are shown from (a) HEJ and (b) other theory descriptions and data [3]. These studies will inform Higgs plus dijets analyses, where cuts are usually applied to select events with large m_{12}	74
134	4.10	The transverse momentum distribution of the third hardest jet in inclusive dijet events in [51], compared to (a) the predictions from HEJ and (b) the predictions from other theory descriptions.	76
135	4.6	The comparison of (a) HEJ and (b) other theoretical descriptions and data [3] to the distribution of the absolute rapidity difference between the two leading jets. HEJ and Blackhat+Sherpa give the best description.	77
136	4.7	These plots show the differential cross section in the ratio of the leading and second leading jet in p_T from (a) HEJ and (b) other theory descriptions and data [3].	77
137	4.8	The inclusive jet rates as given by (a) the HEJ description and (b) by other theoretical descriptions, both plots compared to the CMS data in [51].	78
138	4.9	The transverse momentum distribution of the second hardest jet in inclusive dijet events in [51], compared to (a) the predictions from HEJ and (b) the predictions from other theory descriptions.	78
139	5.1	80
140	5.2	80
141	5.3	81
142	5.4	81
143	5.5	82
144	5.6	82
145	5.7	83
146	5.8	83
147	7.1	12a	89
148	7.2	12a	90
149	7.3	11a	91
150	7.4	11b	92
151	7.5	93
152	7.6	94

¹⁷³ List of Tables

¹⁷⁴ 1.1	The fermion content of the standard model.	2
¹⁷⁵ 2.1	A graphical summary of the Feynman rules. The solid lines indicate ¹⁷⁶ a fermion (anti-fermion) propagator with momentum flowing parallel ¹⁷⁷ (anti-parallel) to the direction of the arrow. Similarly for the dashed ¹⁷⁸ lines which represent the ghost (anti-ghost) propagating and lastly the ¹⁷⁹ twisted lines depict a propagating gluon. As in the preceding equations ¹⁸⁰ i and j represent fundamental colour indices, a and b represent adjoint ¹⁸¹ colour indices and, where present, f and f' represent fermion flavour. ¹⁸² All Greek indices are Lorentz indices.	¹⁰
¹⁸³ 2.2	The Monte-Carlo approximation to equation 2.126 as we vary the number ¹⁸⁴ of sampled points, N , shown in the naive sampling case and in the ¹⁸⁵ importance sampled case.	⁴⁶
¹⁸⁶ 4.1	The total cross-sections for the 2, 3 and 4 jet exclusive rates with asso- ¹⁸⁷ ciated statistical errors shown for different values of the regularisation ¹⁸⁸ parameter λ_{cut} . The scale choice was the half the sum over all traverse ¹⁸⁹ scales in the event, $H_T/2$	⁷⁰
¹⁹⁰ 4.2	Cuts applied to theory simulations in the ATLAS Z -plus-jets analysis ¹⁹¹ results shown in Figs. 4.4–4.7.	⁷²
¹⁹² 4.3	Cuts applied to theory simulations in the CMS Z -plus-jets analysis ¹⁹³ results shown in Figs. 4.8–4.10	⁷⁵

¹⁹⁴ **Chapter 1**

¹⁹⁵ **Introduction**

¹⁹⁶ **1.1 A Little History**

¹⁹⁷ The Standard Model is a gauge quantum field theory describing three of the four
¹⁹⁸ observed fundamental forces - with the inclusion of gravity remaining elusive. Its local
¹⁹⁹ gauge structure is given by:

$$SU(3)_c \times SU(2)_L \times U(1)_Y. \quad (1.1)$$

²⁰⁰ The subscripts on the groups are simply a convenient notation. The ‘c’ on $SU(3)$
²⁰¹ indicates that it is the strong ‘colour’ coupling being described. The ‘L’ on $SU(2)$
²⁰² indicates that all right-handed states are in the trivial representation of the group
²⁰³ and the ‘Y’ on the $U(1)$ indicates that this is the hypercharge group and not the
²⁰⁴ electromagnetic group. The $SU(3)_c$ group describes the strong nuclear force (Quantum
²⁰⁵ Chromodynamics or QCD) and its 8 gauge generators give us the massless spin-1 gluons,
²⁰⁶ $G_a^\mu(x)$, $a = 1, \dots, 8$, present in the standard model. There are three weak boson states,
²⁰⁷ $W_a^\mu(s)$, $a = 1, \dots, 3$, associated with the $SU(2)_L$ group and a further one, $B^\mu(x)$, which
²⁰⁸ comes from the $U(1)_Y$ group.

²⁰⁹ The only remaining boson to complete the standard model arises from the complex
²¹⁰ scalar Higgs field whose ground state is not invariant under the action of $SU(2)_L \times$
²¹¹ $U(1)_Y$. This field breaks the standard model gauge symmetry to

$$SU(3)_c \times U(1)_{em}, \quad (1.2)$$

where the $U(1)_{em}$ refers to the electromagnetic charge. After this ‘Spontaneous Symmetry Breaking’ occurs three of the four aforementioned bosons, $W_a^\mu(s)$ and $B^\mu(x)$ acquire mass and combinations of them are physically realised as the experimentally observer electroweak boson; The massive states W^\pm, Z^0 and the massless photon, γ . The photon and the Z^0 bosons are of particular importance in the work that follows.

The fundamental particle content of the Standard Model also includes fermions. These are spin-1/2 particles which obey the spin-statistics theorem (and hence the Pauli exclusion principle) and comprise, along with the gluons which binds the nucleus together, all known visible matter in the universe. The fermions are structured in three so-called ‘generations’, shown in tab. 1.1 and can be further subdivided into quarks and leptons. Quarks are colour triplets under QCD but are also charged under the electroweak group. The up (u), charm (c) and top (t) quarks have electric charge $+\frac{2}{3}$ while the down (d), strange (s) and bottom (b) quarks have $-\frac{1}{3}$. Leptons are singlets under $SU(3)$ and so do not couple to the strong sector. The charged leptons e, μ and τ have electric charge -1 and the neutrinos are neutral.

	First Generation	Second Generation	Third Generation
Quarks	u, d	c, s	$t,$
Leptons	e, ν_e	μ, ν_μ	τ, ν_τ

Table 1.1: The fermion content of the standard model.

1.2 Thesis Outline

The aim of this thesis is to detail the importance of a certain class of perurbatively higher-order terms in events with QCD radiation in the final state. In particular we will consider corrections to parton-parton collisions with a Z^0 or γ in association with high energy QCD radiation in the final state.

In chapter 2 I will begin by introducing quantum chromodynamics, the theory of the strong sector in the standard model, and detail how we might use this to calculate physical observables (such as cross-sections and differential distributions) at hadron colliders such as the Large Hadron Collider. I will discuss how these observables fall prey to divergences in QCD-like quantum field theories with massless states and mention briefly how such divergences can be handled. I will then describe how the computationally expensive integrals derived in subsequent chapters may be efficiently evaluated using Monte-Carlo techniques.

In chapter 3 the details of QCD in the ‘High Energy’ limit are discussed. After

- 241 completing a few instructive calculations we will see how, in this limit, the traditional
242 fixed-order perturbation theory view of calculating cross-sections fades as another
243 subset of terms, namely the ‘Leading Logarithmic’ terms in $\frac{s}{t}$, become more important.
244 I will discuss previous work in the High Energy limit of QCD and how this can be used to
245 factorise complex parton-parton scattering amplitudes into combinations of ‘currents’
246 which, when combined with gauge-invariant effective gluon emission terms can be used
247 to construct approximate high-multiplicity matrix elements.
- 248 In chapter 4 the work of the previous chapter is extended to the case where there is
249 a massive Z^0 boson or an off-shell photon, γ^* , in the final state. A ‘current’ for this
250 process is derived and the complexities arising from two separate sources of interference
251 are explored. This new result for the matrix element is compared to the results obtained
252 from a Leading Order (in the strong coupling, α_s) generator **MadGraph** at the level of the
253 matrix element squared in wide regions of phase space is seen to be in exact agreement.
254 This result must then be regularised to treat the divergences discussed in chapter 2 and
255 this process is presented. The procedure for matching this regularised result to Leading
256 Order results is shown and the importance of the inclusion of these non-resummation
257 terms is discussed. Lastly three comparisons of the High Energy Jets Z+Jets Monte-
258 Carlo generator to recent experimental studies **ATLAS** and **CMS** at the LHC are shown.
- 259 From here we use the results of chapter 4, and the resulting publicly available Monte
260 Carlo package, to compare our description to a recent experimental prediction of the
261 ratio of the $W^\pm + \text{jets}$ rate to the $Z/\gamma^* + \text{jets}$ rate. Our predictions are compared against
262 next-to-leading order (in α_s) results from **NJet** and leading order results from **MadGraph**.
- 263 In chapter ?? we apply the massive spinor-helicity to the production of a $t\bar{t}$ pair in
264 hadronic collisions. Using the **PySpinor** package we calculate values for the full-mass
265 matrix element and compare them to leading-order (in α_s) results from **MadGraph**. This
266 is a process in which the leading logarithmic contribution starts at one order higher
267 than in previous work and so the effects of the resummation are not as expected to be as
268 crucial as in the case of chapter 4 - however at large values for the centre-of-mass energy
269 (such as that a future high energy circular collider) these ‘next-to-leading’ logarithms
270 will once again lead to the breakdown of fixed-order perturbation theory.
- 271 In chapter 5 we discuss the results of a lengthy study of jet production from the **ATLAS**
272 collaboration. This analysis was a thorough look at BFKL-like dynamics in proton-
273 proton colliders and the HEJ predictions are seen to describe the data well in the
274 regions of phase-space where we know the effects of our resummation become relevant.
275 We compare the predictions from both standalone HEJ and HEJ interfaced with
276 **ARIADNE**, a parton shower based on a dipole-cascade model. Although the interface to

277 ARIADNE increases the computational complexity significantly; we see that the Sudakov
278 logarithms added by significantly improve the description of data.

279 In chapter 7, with a study of $Z/\gamma^* + \text{Jets}$ at a centre-of-mass energy of 100TeV relevant
280 for the discussion of the next wave of high energy particle physics experiments (such
281 as any Future Circular Collider) which are of great interest to the community at large.
282 We see that the higher-order perturbative terms are much larger at 100TeV relative to
283 7TeV data and predictions. Moreover, the regions of phase-space relevant for this thesis;
284 that of high energy wide-angle QCD radiation is especially enhanced and, therefore
285 resumming these contributions will be essential for precision physics at any ‘Future
286 Circular Collider’.

287 Finally, in chapter 8 I summarise the results of the above chapters and provide a short
288 outlook for future work.

²⁸⁹ **Chapter 2**

²⁹⁰ **Quantum Chromodynamics at
hadronic colliders**

²⁹² **2.1 The QCD Lagrangian**

²⁹³ We obtain the QCD Lagrangian by considering the spin- $\frac{1}{2}$ Dirac Lagrangian for the
²⁹⁴ case of a fermionic fields ψ each with mass m :

$$\mathcal{L}_D = \bar{\psi}_i (i\cancel{D} - m)_{ij} \psi_j, \quad (2.1)$$

²⁹⁵ where ψ_i is itself a vector of 3 fermion fields in the fundamental representation of $SU(3)$
²⁹⁶ with $i = 1, \dots, 3^1$. This is manifestly invariant under the *global* $SU(3)$ transformation

$$\psi_i \rightarrow e^{i\alpha^a T_{ij}^a} \psi_j \quad (2.2)$$

²⁹⁷ where $a = 1, \dots, 8$, α^a are constant and T^a are the generators of the $SU(3)$ group. We
²⁹⁸ choose to promote this *global* symmetry to a *local* one by relaxing the constraint that
²⁹⁹ α^a are constant and instead allow them to depend on a space-time coordinate i.e.

$$\alpha^a = \alpha^a(x^\mu). \quad (2.3)$$

¹The choice of 3 here is, again, well experimentally verified. Here we will work explicitly with the gauge group $SU(3)$ although many of the results which follow can be derived with a more general special unitary group $SU(N_c)$.

300 This breaks the $SU(3)$ symmetry but we can recover the required invariance by
301 replacing the usual partial derivative term with a ‘covariant derivative’ defined by:

$$\mathcal{D}_{ij}^\mu = \partial_{ij}^\mu - ig_s A^{\mu a} T_{ij}^a, \quad (2.4)$$

302 where g_s is the QCD coupling constant and A_μ^a is the QCD gauge field associated with
303 the gluon. With this replacement the local $SU(3)$ invariance of eq. (2.1) is recovered.
304 We must also include the effect of the kinetic term for the gluon field in our theory.
305 We do this by considering the field-strength tensor for A_μ^a , $F_{\mu\nu}^a$ which is given by:

$$F_{\mu\nu}^a = \partial_\mu A_\nu^a - \partial_\nu A_\mu^a + g_s f^{abc} A_\mu^b A_\nu^c \quad (2.5)$$

306 where f^{abc} are constants which define the algebra of the $SU(3)$ group and are given by

$$T^a T^b - T^b T^a = i f^{abc} T^c. \quad (2.6)$$

307 eq. (2.6) is what makes QCD fundamentally different from Quantum Electrodynamics
308 (QED): the simple fact that the generators of the underlying group *do not* commute
309 makes performing calculations in QCD significantly more complicated than it’s Abelian
310 cousin QED.

311 In summary then, the QCD Lagrangian is given by

$$\mathcal{L}_{\text{QCD (classical)}} = -\frac{1}{4} F_{\mu\nu}^a F^{a\mu\nu} + \sum_{f=1}^6 \bar{\psi}_i^{(f)} (i \not{D} - m_f)_{ij} \psi_j^{(f)}, \quad (2.7)$$

312 where we have now generalised to the experimentally proven case of 6 ‘flavours’ of quark
313 in our model (outlined previously in tab. (1.1)). This is referred to as the ‘classical’
314 QCD Lagrangian since we have not included quantum effects such as loop corrections.
315 The full ‘quantum’ Lagrangian is as follows [57]:

$$\mathcal{L}_{\text{QCD}} = \sum_{f=1}^6 \bar{\psi}_i^{(f)} (i \not{D}^{ij} - m_f)_{ij} \psi_j^{(f)} - \frac{1}{4} F_{\mu\nu}^a F^{a\mu\nu} - \frac{(\partial^\mu A_\mu^a)^2}{2\xi} + (\partial^\mu \bar{c}^a) \mathcal{D}_\mu^{ab} c^b, \quad (2.8)$$

316 where \mathcal{D}_μ is the covariant derivative in the adjoint representation given by

$$\mathcal{D}_\mu^{ab} = \delta^{ab}\partial_\mu - g_s f^{abc} A_\mu^c. \quad (2.9)$$

317 The final two terms arise from the treatment of a degeneracy in the QCD path integral
 318 which is caused by the gauge symmetry we enforced earlier - as a result we are only
 319 able to define a gluon propagator once we have “fixed the gauge” which is achieved by
 320 the penultimate term in eq. (2.8). ξ is a free parameter in this process and, as we will
 321 see when we come to define the gluon propagator, it’s choice *defines* a specific gauge
 322 (see Appendix A). The final term is a mathematical quirk of this process and c and
 323 \bar{c} represent the resulting QCD “ghost” and “anti-ghost” fields respectively. They are
 324 unphysical since they are spin-1 anti-commuting fields.

325 2.2 The Partonic Cross-Section

326 Now we have a complete Lagrangian for QCD we can begin to move towards physical
 327 observables. The first step towards this is the Lehman-Symanzik-Zimmerman (LSZ)
 328 reduction formula. This gives us a relation between the scattering amplitude from some
 329 initial state into some final state, $\langle f|i\rangle \equiv \langle f|S|i\rangle$ where S is the scattering matrix, and
 330 a time-ordered vacuum expectation operator of a product of fields. Here we briefly
 331 present the argument behind the LSZ formula for the case of $2 \rightarrow 2$ scattering using
 332 scalar phi-cubed theory for simplicity (but this generalises to more complex theories).
 333 The Lagrangian for this theory is given by:

$$\mathcal{L}_{\text{phi-cubed}} = \frac{1}{2}\partial^\mu\phi\partial_\mu\phi + \frac{m^2}{2}\phi^2 - \frac{g}{6}\phi^3. \quad (2.10)$$

334 We can Fourier expand the field, $\phi(x)$, in terms of its annihilation and creating operators
 335 as follows:

$$\phi(x) = \int \frac{d^4k}{2E(2\pi)^3} \left(a(\vec{k})e^{ik\cdot x} + a^\dagger(\vec{k})e^{-ik\cdot x} \right), \quad (2.11)$$

336 and inverting this we find the following form for the creation operator $a^\dagger(\vec{k})$:

$$a^\dagger(\vec{k}) = i \int d^3x e^{-ix\cdot k} (\partial_0 - E) \phi(x), \quad (2.12)$$

337 We expect that as time flows forward to $+\infty$ (or backwards to $-\infty$) the field, $\phi(x)$,

³³⁸ become asymptotically free and therefore we can neglect any interaction effects in these
³³⁹ extremes. From eq. (2.12) it is straightforward to show that:

$$a^\dagger(\vec{k}, t = \infty) - a^\dagger(\vec{k}, t = -\infty) = i \int d^4x e^{-ix \cdot k} (\partial^2 + m^2) \phi(x). \quad (2.13)$$

³⁴⁰ Clearly this would be zero if we only consider the free theory where $g = 0$ in eq. (2.10)
³⁴¹ - intuitively this is correct since once we remove any interaction terms a state we create
³⁴² at $t = -\infty$ should flow to $t = \infty$ unaltered. However, more generally for an interacting
³⁴³ theory it will be non-zero and eq. (2.13) gives us a relationship between asymptotically
³⁴⁴ free initial and final states. Using eq. (2.13) (and its hermitian conjugate) we can begin
³⁴⁵ to look at the scattering from a 2 particle initial state $|i\rangle$ to some 2 particle final state
³⁴⁶ $|f\rangle$, $k_1 + k_2 \rightarrow k'_1 + k'_2$, this is given by:

$$\langle i|j\rangle \equiv \langle 0|T \left(a(k'_1, \infty) a(k'_2, \infty) a^\dagger(k'_1, -\infty) a^\dagger(k'_2, -\infty) \right) |0\rangle, \quad (2.14)$$

³⁴⁷ where T denotes the time-ordered product of operators. After substituting for the a
³⁴⁸ and a^\dagger operators and seeing that the time-ordering means that all of the remaining
³⁴⁹ annihilation/creation operators end up acting on a vacuum state which they annihilate
³⁵⁰ we are left with:

$$\begin{aligned} \langle i|j\rangle = i^4 \int d^4x'_1 d^4x'_2 d^4x_1 d^4x_2 & e^{ik'_1 \cdot x'_1} (\partial_{x'_1}^2 + m^2) e^{ik'_2 \cdot x'_2} (\partial_{x'_2}^2 + m^2) \times \\ & e^{ik_1 \cdot x_1} (\partial_{x_1}^2 + m^2) e^{ik_2 \cdot x_2} (\partial_{x_2}^2 + m^2) \times \\ & \langle 0|T (\phi(x'_1)\phi(x'_2)\phi(x_1)\phi(x_2)) |0\rangle. \end{aligned}$$

³⁵¹ This is the LSZ reduction formula for $2 \rightarrow 2$ scattering in a phi-cubed theory. It reduces
³⁵² the problem of finding scattering amplitudes to the calculation of time-ordered problem
³⁵³ of fields under the assumption that we may treat the fields at $t = \pm\infty$ as free.
³⁵⁴ The next step is to see how we can calculate these time-ordered products. This is most
³⁵⁵ conveniently done by taking functional derivatives of the QCD path integral given by:

$$\mathcal{Z}[J, \eta, \bar{\eta}, \chi, \bar{\chi}] = \int \mathcal{D}A \mathcal{D}\psi \mathcal{D}\bar{\psi} \mathcal{D}c \mathcal{D}\bar{c} e^{i \int d^4x (\mathcal{L}_{QCD} + A^{a\mu} J_\mu^a + \bar{\psi}^a \eta^a + \bar{\eta}^a \psi^a + \bar{c}^a \chi^a + \bar{\chi}^a c^a)}, \quad (2.15)$$

³⁵⁶ where $J^{a\mu}$, η^a , $\bar{\eta}^a$, χ^a and $\bar{\chi}^a$ are ‘source’ terms which we target with functional

357 derivatives and we have left the sum over quark flavours implicit. In order to proceed
 358 we break down eq. (2.1) into a free Lagrangian, $\mathcal{L}_{\text{QCD},0}$, and an interacting Lagrangian,
 359 $\mathcal{L}_{\text{QCD},I}$ as follows:

$$\begin{aligned}
 \mathcal{L}_{\text{QCD}} &= \mathcal{L}_{\text{QCD},0} + \mathcal{L}_{\text{QCD},I}, \\
 \mathcal{L}_{\text{QCD},0} &= \bar{\psi}_i (i\cancel{\partial} - m)_{ij} \psi_j - \frac{1}{4} (\partial_\mu A_\nu^a - \partial_\nu A_\mu^a) (\partial^\mu A^\nu{}^a - \partial^\nu A^\mu{}^a) \\
 &\quad - \frac{(\partial^\mu A_\mu^a)^2}{2\xi} + (\partial^\mu \bar{c}^a) (\partial_\mu c^a), \\
 \mathcal{L}_{\text{QCD},I} &= g_s \bar{\psi}^i T_{ij}^a \gamma^\mu \psi^j - \frac{g_s}{2} f^{abc} (\partial_\mu A_\nu^a - \partial_\nu A_\mu^a) A^{b\mu} A^{c\nu} \\
 &\quad - \frac{g_s^2}{4} f^{abe} f^{cde} A_\mu^a A_\nu^b A^{c\mu} A^{d\nu} - g_s f^{abc} \partial^\mu \bar{c}^a c^b A_\mu^c.
 \end{aligned}$$

360 We can then rewrite eq. (2.15) as a combination of functional derivatives acting on the
 361 free QCD path integral, \mathcal{Z}_0 as:

$$\begin{aligned}
 \mathcal{Z}[J, \eta, \bar{\eta}, \chi, \bar{\chi}] &= \exp \left[i \int d^4x \mathcal{L}_{\text{QCD},I} \left(\frac{\delta}{i\delta J^{\mu a}}, \frac{\delta}{i\delta \eta^a}, \frac{\delta}{i\delta \bar{\eta}^a}, \frac{\delta}{i\delta \xi^a}, \frac{\delta}{i\delta \bar{\xi}^a} \right) \right] \\
 &\quad \times \mathcal{Z}_0[J, \eta, \bar{\eta}, \chi, \bar{\chi}],
 \end{aligned} \tag{2.16}$$

362 where \mathcal{Z}_0 is identical to eq. (2.15) but with the free Lagrangian, in place of the full
 363 Lagrangian. We can solve \mathcal{Z}_0 exactly which yields us the propagators for the gluons,
 364 quarks and ghosts. Respectively:

$$\langle 0 | A_a^\mu(x) A_b^\nu(y) | 0 \rangle = \int \frac{d^4k}{(2\pi)^4} e^{-ik \cdot (x-y)} \delta_{ab} \frac{i}{k^2} \left(g^{\mu\nu} - (1-\xi) \frac{k^\mu k^\nu}{k^2} \right), \tag{2.17a}$$

$$\langle 0 | \bar{\psi}_i^{(f)}(x) \psi_j^{(f')}(y) | 0 \rangle = \int \frac{d^4k}{(2\pi)^4} e^{-ik \cdot (x-y)} \delta_{ij} \delta_{ff'} \frac{i(\not{k} + m)}{k^2 - m^2}, \tag{2.17b}$$

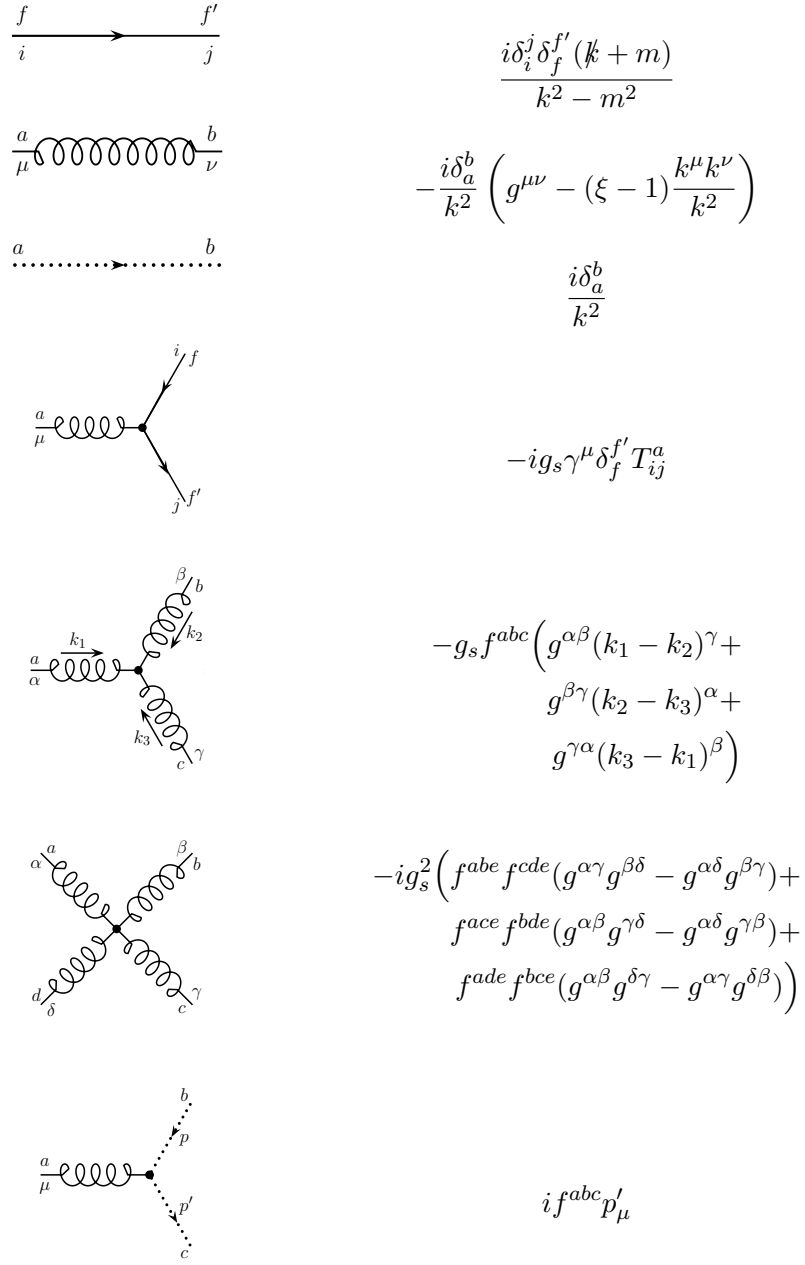
$$\langle 0 | \bar{c}_a(x) c_b(y) | 0 \rangle = \int \frac{d^4k}{(2\pi)^4} e^{-ik \cdot (x-y)} \delta_{ab} \frac{i}{k^2}. \tag{2.17c}$$

365 We can read off the remaining QCD vertex factors directly from the interaction
 366 Lagrangian (or - more rigorously derive them by Taylor expanding eq. (2.16) and
 367 disregarding any irrelevant diagrams such as those where no scattering occurs or those
 368 with bubble contributions).

369 The full set of rules for the vertices and propagators are summarised in tab. (2.1). The

³⁷⁰ remaining *Feynman rules* may be summarised as:

Table 2.1: A graphical summary of the Feynman rules. The solid lines indicate a fermion (anti-fermion) propagator with momentum flowing parallel (anti-parallel) to the direction of the arrow. Similarly for the dashed lines which represent the ghost (anti-ghost) propagating and lastly the twisted lines depict a propagating gluon. As in the preceding equations i and j represent fundamental colour indices, a and b represent adjoint colour indices and, where present, f and f' represent fermion flavour. All Greek indices are Lorentz indices.



- 371 1. Incoming external lines with spin s and momentum p are given a factor of $u_i^{(s)}(p)$
 372 or $\bar{v}_i^{(s)}(p)$ for quarks or anti-quarks. Similarly outgoing external quark or anti-
 373 quark lines get a factor $\bar{u}_i^{(s)}(p)$ or $v_i^{(s)}(p)$. If the external particles are not coloured
 374 the procedure is the same but of course the spinors will no longer be $SU(3)$
 375 fundamental vectors. External gluons with momentum p , polarisation ϵ and
 376 colour a are replaced by $\epsilon^a(p)$ or $\epsilon^{a*}(p)$ depending on whether they are incoming
 377 or outgoing.
- 378 2. For each vertex or propagator in the Feynman diagram insert the corresponding
 379 mathematical expression (see tab. (2.1)). The order of the Lorentz indices must
 380 be the same as that found by tracing the fermion lines in the diagram backwards,
- 381 3. A factor of -1 must be included for each anti-fermion line flowing from the initial
 382 state to the final state,
- 383 4. A factor of -1 must be included for each fermion, anti-fermion or ghost loop in
 384 the diagram
- 385 5. An integration over any unconstrained momenta in the diagram must be included
 386 with measure:

$$\int \frac{d^4k}{(2\pi)^4}, \quad (2.18)$$

385 where k is the momenta in question and the integral is understood to run over
 386 all four momentum components from zero up to infinity,

- 387 6. A diagram dependent symmetry factor must be included,
- 388 7. Lastly, for an unpolarised calculation we must sum over initial spin and colour
 389 and average over all possible final spins and colours.

390 The $u(p)$ and $v(p)$ are Dirac spinors which solve the free Dirac eq. for a plane-wave:

$$(i\gamma^\mu - m)u(p) = 0 \quad (i\gamma^\mu + m)v(p) = 0. \quad (2.19)$$

391 The result of following these Feynman rules is what we refer to as the matrix element,
 392 \mathcal{M} . We will now detail how we go from the matrix element of some scattering process
 393 to a useful physical observable: the *partonic cross-section*, $\hat{\sigma}$. The matrix element
 394 is related to the fully-differential cross-section by ‘Fermi’s golden rule’ which, for a
 395 scattering process $p_a + p_b \rightarrow p_1 + \dots + p_m$ is given by

$$d\hat{\sigma} = \frac{|\mathcal{M}(p_a + p_b \rightarrow p_1^{(f)}, \dots, p_m^{(f)})|^2}{F} \times (2\pi)^4 \delta^{(4)}(p_a + p_b - p_1 - \dots - p_m) \times \frac{d^3 \vec{p}_1}{2E_1(2\pi)^3} \cdots \frac{d^3 \vec{p}_m}{2E_m(2\pi)^3}, \quad (2.20)$$

396 where $F = 4\sqrt{(p_a p_b)^2 - m_a^2 m_b^2}$ is the flux of the incoming particles and the delta
 397 function acts to enforce momentum conservation for the process.

398 We now have a procedure for going from a scattering process we wish to calculate to
 399 the differential cross-section for that process.

400 2.3 Divergences and Regularisation

401 In the preceding section we saw that any unconstrained momenta in a Feynman diagram
 402 must be integrated over to account for all possible ways the momenta in the process
 403 may flow. We refer to these contributions as loop-level or higher-order corrections.
 404 When calculating these corrections we encounter divergences of various kinds which
 405 can be divided up into three classes based on how they arise.

406 2.3.1 Ultraviolet divergences

407 Ultraviolet divergences (UV) occur when all the components of a loop momenta grow
 408 large, $k^\alpha \rightarrow \infty$, such that k^2 becomes the dominant term in propagator. Since these
 409 extremely high momentum modes corresponding to physics at very short distance scales
 410 we choose to interpret these divergences as an indication that our theory is only an
 411 effective theory and we shouldn't attempt to apply it to all scales. We can quickly spot
 412 diagrams with these pathologies with a naive power counting argument. For example
 413 given a diagram which results in a term such as the following:

$$\int \frac{d^4 k}{k^2(k^2 - m^2)}, \quad (2.21)$$

414 where m is some finite mass. In the UV region where $k \rightarrow \infty$ this is asymptotically
 415 equal to:

$$\sim \int \frac{d^4k}{k^4}, \quad (2.22)$$

⁴¹⁶ which is clearly logarithmically divergent.

⁴¹⁷ 2.3.2 Infrared and collinear divergences

⁴¹⁸ Infrared and collinear divergences (IRC) occur in theories with massless gauge bosons,
⁴¹⁹ such as QED and QCD, since a particle may emit any number of arbitrarily such
⁴²⁰ bosons with infinitesimal energy and we would never be able to detect their emission.
⁴²¹ In contrast to the UV divergences the IR becomes important in the region of phase
⁴²² space where $k^2 \rightarrow 0$. A similar power counting analysis to that above can be applied
⁴²³ here. For example if we consider the one-loop correction to the vertex diagram in
⁴²⁴ massless phi-cubed from section (2.2) we would find an integral of the form [64]:

$$I = \int \frac{d^4k}{(2\pi)^4} \frac{1}{k^2(p_1 - k)^2(p_2 + k)^2}, \quad (2.23)$$

⁴²⁵ where k is the loop momentum, $q = p_1 + p_2$ is the incoming momentum and p_i the
⁴²⁶ outgoing momenta. Expanding each momentum into light-cone coordinates with p_1 in
⁴²⁷ the plus-direction, p_2 in the minus-direction:

$$p_1 \sim (p_1^+, 0, \vec{0}) \quad p_2 \sim (0, p_2^-, \vec{0}). \quad (2.24)$$

⁴²⁸ Then take the Eikonal approximation then we have:

$$I = \int \frac{dk^+ k^- k_T^2}{(2\pi)^4} \frac{1}{(2k^+ k^- - k_T^2)(-2p_1^+ k^-)(2p_2^- k^+)}, \quad (2.25)$$

$$= \frac{1}{2q^2} \int \frac{dk^+ k^- k_T^2}{(2\pi)^4} \frac{1}{(2k^+ k^- - k_T^2)(-k^-)(k^+)}, \quad (2.26)$$

⁴²⁹ where $q^2 = 2p_1 \cdot p_2$ since p_i are massless. Here we can further subdivide the divergences
⁴³⁰ contained here into a ‘soft’ sector and a collinear one.

⁴³¹ Considering first the soft regime if we let all the components of our integration variable,
⁴³² k_μ become small at the same rate, that is, $k^\mu \sim \lambda \sqrt{q^2}$ where $\lambda \rightarrow 0$ then after a change
⁴³³ of variables equation (2.26) becomes:

$$I \sim \int \frac{d^4\lambda}{\lambda^4}, \quad (2.27)$$

⁴³⁴ which diverges logarithmically for small lambda. The collinear sector follows similarly,
⁴³⁵ if we now look at the following scaling:

$$k^\pm \sim \sqrt{q^2} \quad k^\mp \sim \lambda^2 \sqrt{q^2} \quad k_T^2 \sim \lambda \sqrt{q^2}. \quad (2.28)$$

⁴³⁶ I.e. as we decrease λ we make k_μ increasingly collinear to either p_1 or p_2 . Using this
⁴³⁷ scaling exactly reproduces eq. (2.27) and therefore is also divergent.

⁴³⁸ 2.3.3 Regularising divergences

⁴³⁹ If we are to extract any useful information from diagrams contributing above leading-
⁴⁴⁰ order we must find ways to control these these divergences. These methods are
⁴⁴¹ called ‘regularisation schemes’. The general plan with all regularisation schemes is to
⁴⁴² introduce a new parameter to the calculation which is used to get a handle on exactly
⁴⁴³ how the integral diverges. Once we have performed the integration we take the limiting
⁴⁴⁴ case where the effect of the regulator vanishes and we will see that the divergence now
⁴⁴⁵ presents itself as some singular function of the regulator when $\Lambda^2 \rightarrow \infty$. There are many
⁴⁴⁶ ways to regularise divergences each with their own advantages and disadvantages. Here
⁴⁴⁷ we briefly describe three common approaches.

⁴⁴⁸ Given that the integrands seen so far only diverge in certain regions (very large or
⁴⁴⁹ very small momenta) perhaps the most obvious thing to do is to manually introduced
⁴⁵⁰ alter the limits of our integration. This is the momentum cut-off scheme. we simply
⁴⁵¹ replace the upper (lower) bound with some finite large (small) value, Λ^2 . This will
⁴⁵² regulate any UV (soft) divergences and allow us to complete the calculation provided
⁴⁵³ there are no collinear singularities which this approach cannot hope to regulate. While
⁴⁵⁴ this method has the advantage of being very conceptually simple it also has the serious
⁴⁵⁵ disadvantages of breaking translational and gauge invariance. Worse still is that simply
⁴⁵⁶ limiting the integration to avoid the extremities has not effect on the collinear sector.

⁴⁵⁷ An alternative which *does* keep both gauge and translational invariance is the Pauli-
⁴⁵⁸ Villars regularisation scheme [59]. In this picture we replace the introduce and extra
⁴⁵⁹ field (or many extra fields [40]) which has the opposite spin-statistics and therefore has
⁴⁶⁰ the effect of suppressing the very high mass region in the integrand as follows

$$\int \frac{d^4k}{(2\pi)^4} \frac{1}{p^2 - m^2} \rightarrow \int \frac{d^4k}{(2\pi)^4} \left(\frac{1}{p^2 - m^2} - \frac{1}{p^2 - M^2} \right), \quad (2.29)$$

461 where M is the mass of the Pauli-Villars field with $m \ll M$. However, once again this
462 does not treat any problems in the IRC sectors.

463 Lastly we have dimensional regularisation. Here we analytically continue the number
464 of dimensions in our integral away from $d = 4$. We still want to be able to return to
465 our physical four dimensional theory and so we choose

$$d = 4 - 2\epsilon \quad (2.30)$$

466 where ϵ is the regulator by which we control the divergence. Clearly then the limit $\epsilon \rightarrow 0$
467 would recover our original theory. It is worth noting that there are many conventions
468 for defining epsilons but up to signs and factors of 2 they are equivalent. Dimensional
469 regularisation treats both the UV and the IRC divergences and translational and gauge
470 invariance are preserved. The disadvantage is that this modification changes the Dirac
471 algebra relations which typically makes computing the integrals more involved.

472 2.4 Renormalising the QCD Lagrangian

- 473 • Is this section really necessary? We don't actually use counter-terms/dressed
474 vertices anywhere etc.
- 475 • Could be combined with the following section as 'Renormalisation and the QCD
476 Beta function'?

477 2.5 The QCD Beta function

478 QCD has two striking features which are not apparent from the Lagrangian derived
479 above. The first is asymptotic freedom. This is the fact that at *high* energies the QCD
480 coupling strength becomes increasingly weak and it is this which allows us to perform
481 a perturbative expansion of physical observables such as cross-sections. The second
482 feature is confinement. Confinement is the reason we do not observe bare quarks and
483 gluons in nature, instead we only see bound states of these fundamental QCD partons.
484 This is because at very *low* energies the coupling strength becomes increasingly strong.

485 It turns out that when renormalise QCD to remove the ultraviolet singularities we
486 introduce a scale dependence in the coupling strength:

$$\alpha_s = \alpha_s(\mu_r). \quad (2.31)$$

487 This scale, μ_r , is the renormalisation scale discussed in section (2.4). It can be
488 interpreted as a measure of our ignorance of the true high-scale theory which governs
489 nature, that is to say, we believe QCD is the right theory *only up to* some scale μ_r .
490 The evolution of α_s with μ_r is given by the renormalisation group equation:

$$\mu_r^2 \frac{\partial \alpha_s}{\partial \mu_r^2} = \beta(\alpha_s(\mu_r^2)), \quad (2.32)$$

491 where the $\beta(\alpha_s)$ is the beta function. It can be expanded perturbatively as a series in
492 α_s as follows:

$$\beta(\alpha_s) = -\beta_0 \alpha_s (1 + \beta_1 \alpha_s + \beta_2 \alpha_s^2 + \dots), \quad (2.33)$$

493 where the perturbative coefficients, β_i , can be calculated using the methods of section
494 (2.2). For example the leading order contribution, β_0 , is given by:

$$\beta_0 = 11 - \frac{2n_f}{3}. \quad (2.34)$$

495 If we truncate eq. (2.33) at leading-order in α_s then we can solve eq. (2.32) and we see
496 that the coupling, $\alpha_s(\mu_r)$, ‘runs’ with the following form:

$$\alpha_s(Q^2) = \frac{\alpha_s(\mu_r^2)}{1 + \alpha(\mu_r^2) \frac{\beta_0}{4\pi} \ln \frac{Q^2}{\mu_r^2}}. \quad (2.35)$$

497 It is clear from this (since in the standard model we have $n_f \leq 6$ and therefore $\beta_0 > 0$ ²)
498 that as Q^2 tends to zero the coupling strength becomes very large and at high values for
499 Q^2 we see that $\alpha_s(Q^2) \rightarrow 0$. This later limit is exactly the asymptotic freedom property
500 of QCD and it holds even when we include the higher order terms we neglected in the
501 leading-order approximation used to arrive at eq. (2.35) [20]. It is an essential result

²The number of fermions we consider depends on the energy scale we are at. Clearly we must be at an energy larger than the mass of any given quark for it to be produced. This was experimentally observed in the famous R -ratio where the ratio of the $e^+e^- \rightarrow$ hadrons cross-section to the $e^+e^- \rightarrow \mu^+\mu^-$ cross-section was investigated

in that it allows us to perform perturbative expansions of observables and without this none of the following work would be possible. The evolution of the strong coupling with Q^2 is shown in fig. (2.1), it shows several extracted values of α_s based on six various types of experiment. For example, the hadronic collider predictions include studies of the ratio of the 3-jet inclusive cross-section to the 2-jet inclusive cross-section as a means of finding the strong coupling [31].

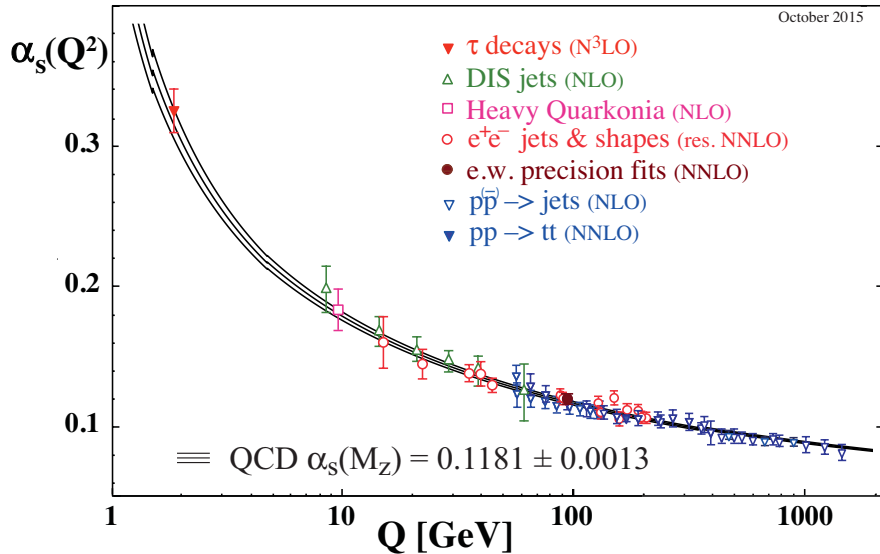


Figure 2.1: The evolution of α_s over several orders of magnitude in the scale of the process Q^2 . The data points fitted are of varying degrees of formal accuracy ranging from next-to-leading order in α_s (NLO) to next-to-next-to-next-to-leading order in α_s (N³LO). Fig. from [20].

2.6 QCD Factorisation at Hadronic Colliders

So far we have only talked about the very general idea of two particles interacting and scattering off one another into some final state which we are interested in. This is too simple a picture when we are considering hadronic colliders such as the Large Hadron Collider (proton-proton), the Tevatron (proton-antiproton), HERA (proton-lepton) and, potentially, a Future Circular Collider (FCC) with a hadronic initial state. At experiments we collide QCD bound states with one another but in practise when calculating cross-sections we perform a sum over the possible combinations of initial states we may encounter in the two incoming hadrons. In order to do this we must have a good understanding of the dynamics of the partons inside the onrushing hadrons; this understanding is encoded in the Parton Distribution Functions (PDFs). A PDF,

519 $f_{i/H}(x, Q^2)$ is a function which tells us how likely we are to find a parton of type i
520 carrying a fraction x of the total hadrons momentum in a hadron, of type H , during a
521 collision occurring at an energy scale Q . Because the PDFs contain non-perturbative
522 information we cannot compute their properties in the same way as we calculate cross-
523 sections, instead they are determined by fitting to data from a range of experiments
524 (such as those mentioned above). Once we have the PDFs we can compute the physical
525 hadronic cross-sections, σ , by convoluting two of them (one for each hadron) with the
526 partonic cross-section for the scattering of partons of type i and j , $\hat{\sigma}_{ij}$, discussed in
527 section (2.2) and summing over the possible initial partons as follows:

$$\sigma(Q^2) = \sum_{f_a, f_b} \int_0^1 dx_a dx_b f_{a/H_a}(x_a, Q^2) f_{b/H_b}(x_b, Q^2) \hat{\sigma}_{ij}(\alpha_s(\mu_r), \mu_r^2, \mu_f^2). \quad (2.36)$$

528 Eq. (2.36) can be intuitively understood as a separation of scales; the long distance
529 physics of the PDFs is manifestly distinct from the short distance hard scatter contained
530 in the partonic cross-section. The scale at which we separate the long and short range
531 physics is called the *factorisation scale*, μ_f . As with the renormalisation scale it is
532 not *a priori* clear what is the correct factorisation scale and results of perturbative
533 calculations are often quoted with a ‘scale uncertainty’ band.

534 2.7 From Partons to Jets

535 As alluded to in section (2.5) the computations of scattering amplitudes can only take us
536 so far when comparing simulations to experiments. In particular, the final state quarks
537 and gluons in our perturbative picture of QCD differ from the confined hadrons observed
538 at hadronic colliders: It is well known that final state QCD partons fragment and emit
539 showers of additional radiation before finally they becomes colourless bound states in
540 a process known as ‘hadronisation’. This process is not perturbatively well-understood
541 since it occurs at scale, often called Λ_{QCD} , at which QCD becomes non-perturbative, *i.e.*
542 the coupling constant of the theory has become too large for us to legitimately truncate
543 a perturbative expansion. There are models for both the ‘parton shower’ behaviour of
544 the energetic final state partons, such as **Pythia** [63], **Herwig** [33] and **Sherpa** [46] as
545 well as models for the hadronisation such as the ‘Lund string model’ [17] implemented
546 in various physics software packages but most relevantly (for the remainder of this
547 thesis) - in the **Ariadne** code.
548 All high energy collider experiments see a great deal of QCD radiation in the final
549 state. This radiation, produced through the mechanisms outlined above, appears in

550 columnated structures called ‘jets’ and so it is at the jet level that we may compare our
 551 simulated results to actual measurements. The question of how we best map from the
 552 parton level to the jet level is not a trivial one: A single high-energy (or ‘hard’) parton
 553 may split and form two final state jets but equally two low energy (or ‘soft’) partons
 554 may combine into a single jet.

555 There are several approaches to this problem include the **SISCone** algorithm [61] and
 556 Pythia’s own implementation **CellJet** [62]. However the most commonly user family
 557 of jet reconstruction algorithm are know as the ‘sequential recombination algorithms’.
 558 This group of approaches include the Cambridge-Aachen, k_T and anti- k_T algorithms.
 559 The general algorithm, as given in [24], is:

- 560 1. Given a list of final state partons calculate some generalised distance, d_{ij} , between
 561 all possible combinations of jets i and j as well as d_{iB} where B is the beam-line,
- 562 2. We identify the smallest value of these. If, say d_{ab} is the smallest, we combine
 563 partons a and b . If however d_{aB} is the smallest then we call a a jet and remove
 564 it from the list of partons,
- 565 3. We then recompute all the generalised distances and repeat steps 1 and 2 until
 566 no further partons remain,

567 where the generalised distances are defined as

$$d_{ij} = \min(k_{Ti}^{2p}, k_{Tj}^{2p}) \frac{\Delta R^2}{R^2}, \quad (2.37)$$

$$d_{iB} = k_{Ti}^{2p},$$

568 where k_{Ti} is the transverse momentum of the i^{th} parton, R is a free parameter in
 569 the clustering which relates to the size of the jets and ΔR^2 is the distance in the
 570 detector metric between the two partons given $\Delta R^2 = \Delta\phi^2 + \Delta y^2$ where $\Delta\phi$ and Δy
 571 are the angular distance (about the beam line) between the partons and the rapidity
 572 gap between the partons respectively. The parameter is p and it is this which specifies
 573 precisely which clustering algorithm we are using; $p = 0$ reduces to the Cambridge-
 574 Aachen scheme while $p = \pm 1$ give the k_T and anti- k_T respectively. The question of
 575 which to use is outlined in detail in [24] but we give a brief summary here.

576 The choice of jet algorithm boils down to handful of key properties the algorithm much
 577 exhibit. Given a set of hard QCD final states we require that the result of the clustering
 578 algorithm, i.e. the jets and jet shapes, are not unduly sensitive to additional soft and
 579 collinear radiation. This is intuitively clear since, for example, a final state with a

580 single high energy quark with momentum, k_{Ti} , may radiate infinitely a multitude of
581 infinitely soft gluons, k_{Ts_i} , which may (or may not) be collinear to the original parton
582 - but since $k_{Ts_i} \ll k_{Ti}$ the result must be a single jet, j_{Ti} , which has $j_{Ti} \sim k_{Ti}$.
583 Any algorithm which satisfies this is said to be infra-red and collinear (IRC) safe. We
584 also want an algorithm which is insensitive to the hadronisation model used, or any
585 possible extra multiple-parton or experimental pile-up emissions since these things are,
586 at present, poorly understood. It is also worth mentioning that since jet clustering
587 algorithms are used in experimental triggers to quickly catagorise events they should
588 be as computational cheap as possible.
589 Although the Cambridge-Aachen algorithm has advantages in some experimental
590 searches such as studies where the substructure of jets is of particular interest [7,22], the
591 most widely used sequential recombination algorithm is the anti- k_t algorithm ($p = -1$)
592 and so all of the work which follows and all of the experimental comparisons made will
593 use this as the method for mapping simulated parton level results to a more useful set
594 of jet level results. The jet size parameter R varies between experiments but is typically
595 either 0.4 for ATLAS analyses or 0.5 for CMS analyses.

596 2.8 Perturbative QCD and Resummation

597 In section 2.2 we saw that we could separate out the QCD Lagrangian into free and
598 interacting components and that vacuum expectations of time ordered fields could
599 be found by taking functional derivatives of the free partition function (eq. (2.16)).
600 Since terms which give rise to interactions in the Lagrangian come with a factor of
601 the coupling strength, g , Taylor expanding the exponential in eq. (2.16) will yield an
602 infinite series of terms and, in principle, in order to compute any physical observable we
603 must calculate we must evaluate all of these. Of course in practise this is not possible.
604 We must choose a subset of terms from this infinite array which we reason will give the
605 *best possible approximation to the full series*.

606 2.8.1 Fixed-order Perturbation

607 The fixed-order perturbative operates on the assumption that since, as we saw in section
608 2.5, the coupling strength α_s , and hence also the coupling constant, g , in the expansion,
609 becomes small at large energy scales we may truncate the series at some power of g .
610 For example given a cross-section of a scattering, $X \rightarrow Y$, we wish to calculate the
611 fixed order picture of the expansion would be:

$$\sigma_{X \rightarrow Y} = \sum_{i=1}^N \alpha_s^i(Q^2) \mathcal{C}_{X \rightarrow Y}^{(i)} \quad (2.38)$$

612 where $\mathcal{C}_{X \rightarrow Y}^{(i)}$ are the coefficient terms which encode the kinematics of the diagrams
 613 contributing at each ‘order’ in the series. Since we expect that the more terms we
 614 can calculate the better our truncated series will approximate the full result we should
 615 choose N as large as possible though in principle it is determined by the complexity and
 616 the computational cost of the relevant calculation of the coefficient functions. Recent
 617 progress has allowed the automation of next-to-leading order QCD calculations ($N = 2$)
 618 in packages such in **MadGraph** (v5) [13], **BlackHat** [21], **MC@NLO** [38] and **Powheg** [37]. In
 619 general it is not known how to compute multi-loop (i.e. $N \geq 3$) calculations and while
 620 process specific calculations have been completed [23, 41, 43], it is still very much a hot
 621 topic in theoretical physics.

622 It is important to note the limitations of this fixed-order scheme. For example if we
 623 were to consider NLO corrections to dijet production we would only be able to produce
 624 final states with two or three jets (since we can only have one extra real emission).
 625 Clearly this is a limitation since the external fermion lines can radiate arbitrarily many
 626 extra gluons. It is precisely this phenomenon which is shown in fig. 2.2, the NLO
 627 calculations (shown in green and black) are limited to $\langle \text{jets} \rangle \leq 3$ which the predictions
 628 from **POWHEJ+PYTHIA** and **HEJ** which include higher-order corrections and predict a
 629 higher average number of jets. Note that the higher-order corrections here are *not*
 630 the same in the case of **POWHEJ+PYTHIA** and **HEJ**. Also note that although the scale
 631 uncertainty band of the NLO calculation *does* exceed $\langle \text{jets} \rangle = 3$ this is not a result
 632 of the formalism but instead comes about as the result of an attempt to quantify the
 633 residual dependence of the calculation on the factorisation and renormalisation scales.
 634 This scale dependence of observables will be discussed in more detail in chapter 4.
 635 There are frameworks to allow the ‘merging’ of NLO calculations of different multiplicity
 636 but the details of these are beyond the scope of this thesis. A comprehensive review of
 637 such methods may be found in [11].

638 We now present an instructive fixed-order calculation of the next-to-leading corrections
 639 to quark-antiquark pair production via an off-shell photon [35].

640 2.8.2 An Example Fixed-Order Calculation

641 The Feynman diagrams which need to be included for the and $\mathcal{O}(1)$ and $\mathcal{O}(\alpha_s)$
 642 corrections to the $\gamma^* \rightarrow q\bar{q}$ process are shown in fig. (2.3). We refer to fig. (2.3a)

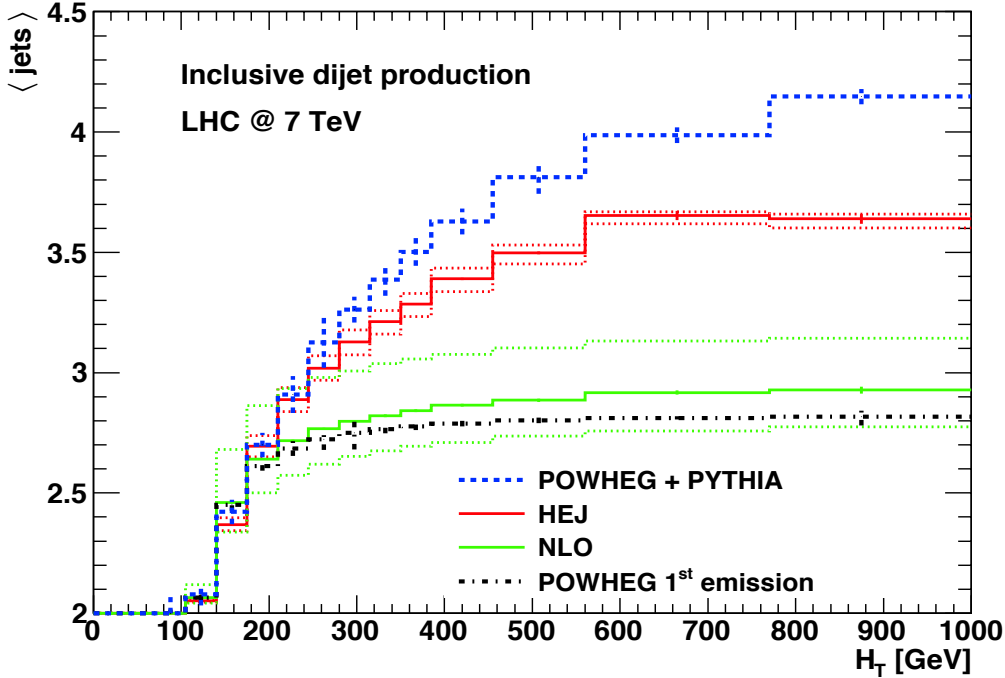


Figure 2.2: Simulations of the average number of jets as a function of the sum of the transverse momenta in the event, H_T , for inclusive dijets at a 7TeV LHC.

as the tree level diagram, fig. (2.3b) as the vertex correction and figs. (2.3c) and (2.3d) as the self-energy corrections. Figs. (2.3e) and (2.3f) are the ‘real correction’. Since the virtual corrections all have the same final state they must be summed and squared together. To make the order of each term in the perturbative expansion clear we extract the α_s factors from the \mathcal{A}_i here. Therefore:

$$\begin{aligned} |\mathcal{M}|^2 &= |\mathcal{A}_0 + \alpha_s \mathcal{A}_v + \alpha_s \mathcal{A}_{se1} + \alpha_s \mathcal{A}_{se2}|^2 + \mathcal{O}(\alpha_s^2) \\ &= |\mathcal{A}_0|^2 + 2\alpha_s \Re\{\mathcal{A}_0^* \mathcal{A}_v\} + 2\alpha_s \Re\{\mathcal{A}_0^* \mathcal{A}_{se1}\} \\ &\quad + 2\alpha_s \Re\{\mathcal{A}_0^* \mathcal{A}_{se2}\} + \mathcal{O}(\alpha_s^2), \end{aligned} \quad (2.39)$$

where the bar on the LHS means there is an implicit sum over spins and polarisations on the RHS. We can see then that to $\mathcal{O}(\alpha_s)$ we have four contributions to consider, but the two self-energy contributions will have the same functional form so it would seem that in practice we only need to perform three calculations - it turns out this is not the case; we will find that the divergence associated with exchanging a soft gluon

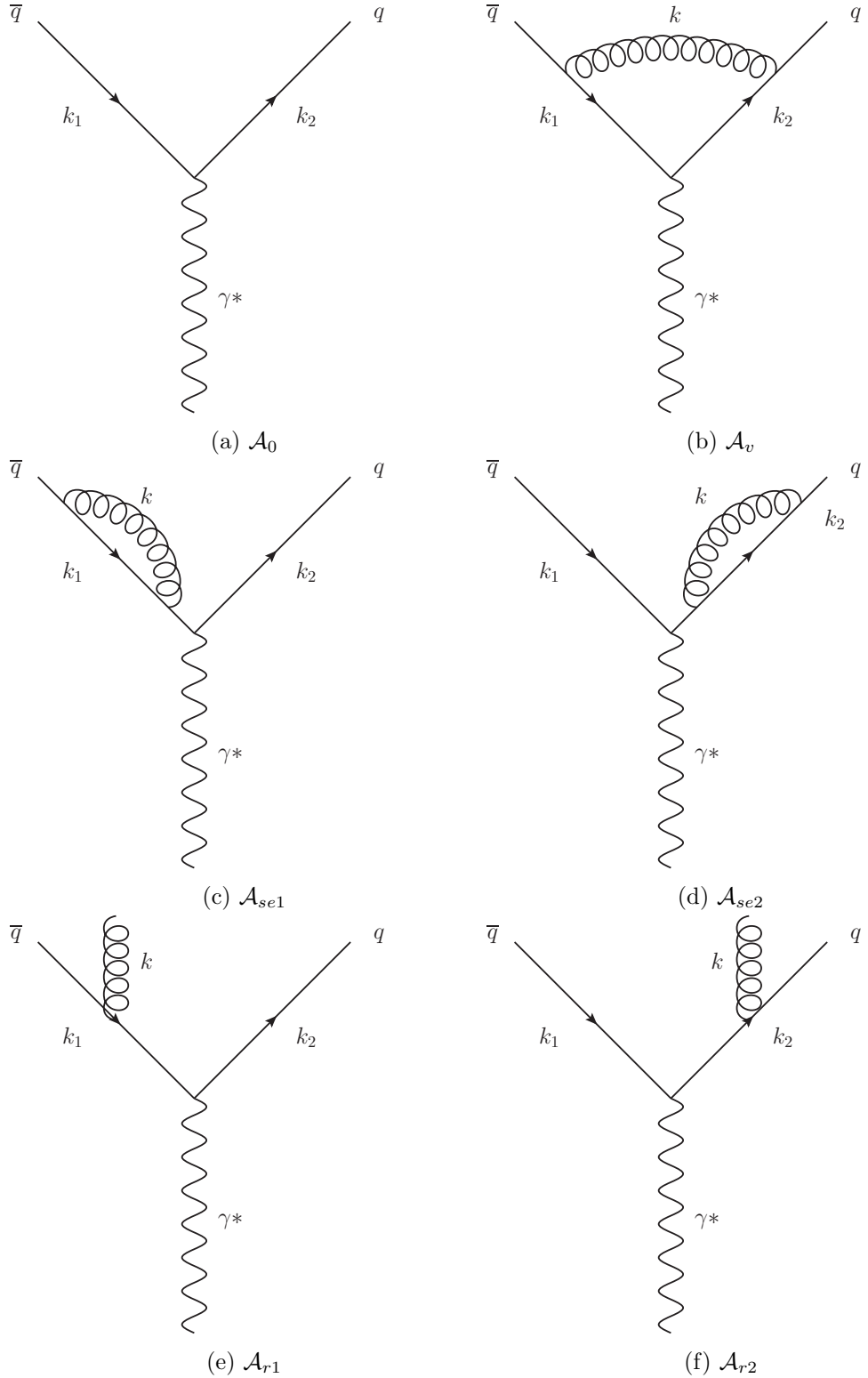


Figure 2.3: Feynman diagrams for calculating the $O(\alpha_s)$ correction to $\gamma^* \rightarrow q\bar{q}$. Fig. (2.3a) is the leading order contribution. Figs. (2.3b - 2.3d) are the virtual corrections and lastly figs. (2.3e - 2.3f) are the real emission contributions.

in fig. (2.3b) can only be cancelled if we also include the soft divergences that arise from figs. (2.3e) to (2.3f). At first glance this seems very peculiar since these diagrams have different final states and therefore should have no business contributing to this calculation. However, since the gluon can be emitted with vanishingly small momentum it would be experimentally impossible to detect and therefore the final states would look the same to an imperfect observer.

It is the cancellation of these divergences that will be shown in detail in the next two sections. Figs. (2.3a), (2.3b) and (2.3e) will be calculated in detail while the result for the self energy expressions will only be omitted since it can be cancelled by choosing the work in the Landau gauge [35]. Since we expect both UV and IR divergences we choose to work in the dimensional regularisation scheme.

664 The Leading Order Process

If we let the pair-produced quarks have charge $\pm Qe$ then the Feynman rules outlined in section 2.2 give:

$$\mathcal{A}_0 = -ieQ\bar{u}^{\lambda_2}(k_2)\gamma^\mu v^{\lambda_1}(k_1)\epsilon_\mu^r(p), \quad (2.40)$$

where we have used the QED Feynman rule for a quark-antiquark-photon vertex: $iQe\gamma^\mu$, the λ_i 's are the spins of the quarks, r is the polarisation of the incoming photon and $p = k_1 + k_2$ is the momentum carried by the incoming photon. To calculate we can square and since we are typically interested in unpolarised calculations we perform a sum over all polarisations and spins (we also choose this point to include the sum over the possible colour states of the outgoing quarks):

$$|\overline{\mathcal{A}_0}|^2 = 3 \sum_{\forall \lambda, r} e^2 Q^2 [\bar{u}^{\lambda_2}(k_2)\gamma^\mu v^{\lambda_1}(k_1)][\bar{v}^{\lambda_1}(k_1)\gamma^\nu v^{\lambda_2}(k_1)]\epsilon_\mu^r(p)\epsilon_{*\mu}^r(p). \quad (2.41)$$

We can now use Casimir's trick [44] to convert this spinor string into a trace, using the replacements $\sum_r \epsilon_\mu^r \epsilon_{*\nu}^r = -g_{\mu\nu}$ and the completeness conditions for spinors:

$$|\overline{\mathcal{A}_0}|^2 = -e^2 Q^2 \text{Tr}[\not{k}_2 \gamma^\mu \not{k}_1 \gamma_\mu], \quad (2.42)$$

where we have used the high energy limit to discard the quark mass terms. This trace can be evaluated in arbitrary dimensions to give, in the high energy limit:

$$|\overline{\mathcal{A}_0}|^2 = 6e_d^2 Q^2 s(d-2), \quad (2.43)$$

677 where we have defined the usual Mandelstam variable $s = (k_1 + k_2)^2 = 2k_1 \cdot k_2$ and define
 678 $e_d^2 = e^2 \mu^{4-d}$ where μ has units of mass in order to make the coupling e dimensionless.
 679 To find the leading order cross-section we divide by the particle flux and multiply by
 680 the two particle phase space which is given by:

$$\int d^{2d-2} R_2 = 2^{1-d} \pi^{\frac{d}{2}-1} \frac{\Gamma(\frac{d}{2}-1)}{\Gamma(d-2)} s^{\frac{d-4}{2}}, \quad (2.44)$$

681 where R_2 is the two particle phase space in d dimensions. Combining these factors and
 682 defining $\alpha_e = \frac{e^2}{4\pi}$:

$$\begin{aligned} \sigma_0 &= 3 \cdot 2^{2-d} \pi^{1-\frac{d}{2}} \frac{\Gamma(\frac{d}{2}-1)}{\Gamma(d-2)} s^{\frac{d-4}{2}} 4\pi \alpha \mu^{d-4} Q^2 s(d-2) \frac{1}{2s} \\ &= 3\alpha Q^2 \left(\frac{s}{4\pi\mu^2} \right)^{\frac{d}{2}-2} \left(\frac{d}{2}-1 \right) \frac{\Gamma(\frac{d}{2}-1)}{\Gamma(d-2)}. \end{aligned} \quad (2.45)$$

683 and finally using $x\Gamma(x) = \Gamma(x+1)$ we get:

$$\sigma_0 = 3\alpha Q^2 \frac{\Gamma(\frac{d}{2})}{\Gamma(d-2)} \left(\frac{s}{4\pi\mu^2} \right)^{\frac{d}{2}-2}. \quad (2.46)$$

684 It is important to note that in the limit $\epsilon \rightarrow 0$ the Born cross-section remains finite.

685 The Virtual $\mathcal{O}(\alpha_s)$ Corrections

686 The virtual correction graphs are shown in figs. (2.3b), (2.3c) and (2.3d). We will begin
 687 by calculating the second term in eq. (2.39). Using the Feynman rules we have:

$$\begin{aligned} \mathcal{A}_v &= \int \frac{d^d k}{(2\pi)^d} \bar{u}^{\lambda_2}(k_2) (-ig_s \mu^\epsilon \gamma^\alpha T_{ij}^a) \frac{i(\not{k}_1 + \not{k})}{(k_1 + k)^2} (-ieQ \gamma^\mu) \frac{i(\not{k}_2 - \not{k})}{(k_2 - k)^2} \\ &\quad (-g_s \mu^\epsilon \gamma^\beta T_{ij}^a) \epsilon_\mu^r(p) \frac{-i}{k^2} \left(g_{\alpha\beta} + (1-\xi) \frac{k^\alpha k^\beta}{k^2} \right) v^{\lambda_1}(k_1). \end{aligned}$$

$$\mathcal{A}_v = -ig_s^2 e Q \mu^{2\epsilon} \text{Tr}(T^a T^a) \bar{u}^{\lambda_2}(k_2) \int \frac{d^d k}{(2\pi)^d} \frac{\mathcal{N}_1(k_1, k_2, k)}{k^2(k_1 + k)^2(k_2 - k)^2} v^{\lambda_2}(k_2),$$

688 where the numerator of the fraction is given by:

$$\mathcal{N}_1(k_1, k_2, k) = \gamma^\alpha(\not{k}_1 + \not{k}) \gamma^\mu(\not{k}_2 - \not{k}) \gamma_\beta \left(g^{\alpha\beta} + (1 - \xi) \frac{k^\alpha k^\beta}{k^2} \right). \quad (2.48)$$

689 From eq. (2.39) we see we need $\mathcal{A}_0^* \mathcal{A}_v$:

$$\mathcal{A}_0^* \mathcal{A}_v = g_s^2 e^2 Q^2 \text{Tr}(T^a T^a) [\bar{v}^{\lambda_1}(k_1) \gamma^\nu u(k_2)] \quad (2.49)$$

$$[\bar{u}^{\lambda_2}(k_2) \int \frac{d^d k}{(2\pi)^d} \frac{\mathcal{N}_1(k_1, k_2, k)}{k^2(k_1 + k)^2(k_2 - k)^2} v^{\lambda_1}(k_1)] \epsilon_\mu^r(p) \epsilon_{*\nu}^r(p). \quad (2.50)$$

690 Now performing the spin/polarisation/colour sum and average gives:

$$\overline{\mathcal{A}_0^* \mathcal{A}_v} = -\frac{g_s^2 e^2 Q^2}{2} \int \frac{d^d k}{(2\pi)^d} \frac{\mathcal{N}_2(k_1, k_2, k)}{k^2(k_1 + k)^2(k_2 - k)^2}, \quad (2.51)$$

691 where:

$$\mathcal{N}_2(k_1, k_2, k) = \text{Tr}[\not{k}_1 \gamma_\alpha(\not{k}_1 + \not{k}) \gamma_\mu(\not{k}_2 - \not{k}) \gamma_\beta \not{k}_2 \gamma^\mu] \left(g^{\alpha\beta} + (1 - \xi) \frac{k^\alpha k^\beta}{k^2} \right). \quad (2.52)$$

692 Before we can proceed any further we must evaluate the trace term in the integral.
693 As mentioned briefly in section 2.3.3 this is not as easy as it seems because, although
694 the Dirac matrices still satisfy the Clifford algebra, the various identities for their
695 contractions and traces change when we are in d dimensions. Two useful examples are
696 shown below:

$$g_{\mu\nu} g^{\mu\nu} = d \quad (2.53a)$$

$$\gamma^\mu \gamma_\nu \gamma_\mu = (d - 2) \gamma_n u \quad (2.53b)$$

697 Using the FORM package [52] to perform the two trace terms present gives:

$$\begin{aligned} \text{Tr}[\not{k}_1 \gamma_\alpha (\not{k}_1 + \not{k}) \gamma_\mu (\not{k}_2 - \not{k}) \gamma^\alpha \not{k}_2 \gamma^\mu] &= s[s(8 - 4d) + \frac{(k_1 \cdot k)(k_2 \cdot k)}{s}(32 - 16d) \\ &\quad - (16 - 8d)(k_1 \cdot k - k_2 \cdot k) + k^2(16 - 12d + 2d^2)], \end{aligned} \quad (2.54)$$

698 and,

$$\begin{aligned} \text{Tr}[\not{k}_1 \gamma_\alpha (\not{k}_1 + \not{k}) \gamma_\mu (\not{k}_2 - \not{k}) \gamma_\beta \not{k}_2 \gamma^\mu] k^\alpha k^\beta &= s[(k_1 \cdot k)(k_2 \cdot k)(16 - 8d) \\ &\quad + k^2(8 - 4d)(k_2 \cdot k - k_1 \cdot k) - k^4(4 - 2d)], \end{aligned} \quad (2.55)$$

699 where $s = 2k_1 \cdot k_2$ and we have used the on-shell relations. After factorising the terms
700 quadratic in d and combining the two trace terms we arrive at:

$$\overline{\mathcal{A}_0^* \mathcal{A}_v} = -4s \left(\frac{d}{2} - 1 \right) \frac{g_s^2 e^2 Q^2}{2} \int \frac{d^d k}{(2\pi)^d} \frac{\mathcal{N}_3(k_1, k_2, k)}{k^2(k_1 + k)^2(k_2 - k)^2}, \quad (2.56)$$

701 where:

$$\mathcal{N}_3(k_1, k_2, k) = -2s + \frac{8k \cdot k_1 k \cdot k_2}{s} + (6 + 2\xi)(k \cdot k_1 - k \cdot k_2) + k^2(d - 4) \quad (2.57)$$

$$-4(1 - \xi) \frac{k \cdot k_1 k \cdot k_2}{k^2} - (1 - \xi)k^2. \quad (2.58)$$

702 Combining this with the particle flux and the two particle phase space we can write
703 an expression for the vertex corrected cross-section. Once again we scale the couplings
704 such that they remain dimensionless by defining $g_d^2 = g_s^2 \mu^{2-\frac{d}{2}}$:

$$\begin{aligned} \sigma_v &= -4s \left(\frac{d}{2} - 1 \right) \frac{g_d^2 \mu^{2-\frac{d}{2}} e^2 Q^2}{4s} 2^{1-d} \pi^{\frac{d}{2}-1} \frac{\Gamma(\frac{d}{2}-1)}{\Gamma(d-2)} s^{\frac{d-4}{2}} \int \frac{d^d k}{(2\pi)^d} \frac{\mathcal{N}_3(k_1, k_2, k)}{k^2(k_1 + k)^2(k_2 - k)^2}, \\ \Rightarrow \sigma_v &= -g_d^2 \mu^{2-\frac{d}{2}} Q^2 4\pi \alpha \mu^{4-d} 2^{1-d} \pi^{\frac{d}{2}-1} \frac{\Gamma(\frac{d}{2})}{\Gamma(d-2)} s^{\frac{d-4}{2}} \int \frac{d^d k}{(2\pi)^d} \frac{\mathcal{N}_3(k_1, k_2, k)}{k^2(k_1 + k)^2(k_2 - k)^2}, \\ \Rightarrow \sigma_v &= -\frac{4\sigma_0}{3} g_d^2 \mu^{2-\frac{d}{2}} \int \frac{d^d k}{(2\pi)^d} \frac{\mathcal{N}_3(k_1, k_2, k)}{k^2(k_1 + k)^2(k_2 - k)^2}, \end{aligned}$$

705 where we have expressed the virtual rate as a multiplicative correction to the Born

706 level rate by comparing directly with eq. (35). We must now use the Feynman
 707 parametrisation to re-express the product of propagators as a sum by introducing new
 708 integration variables. Using:

$$\frac{1}{ab} = \int_0^1 dy \frac{1}{(ay + b(1-y))^2}, \quad (2.60)$$

709 we have:

$$\sigma_v = -\frac{4\sigma_0}{3} g_d^2 \mu^{2-\frac{d}{2}} \int \frac{d^d k}{(2\pi)^d} \int_0^1 dy \frac{\mathcal{N}_3(k_1, k_2, k)}{(k^2 - 2k \cdot k_y)^2 k^2}, \quad (2.61)$$

710 where $k_y = yk_1 - (1-y)k_2$. Examining now the integrand we see there are two different
 711 k dependences and so we partition the terms as follows:

$$\sigma_v = -\frac{4\sigma_0}{3} g_d^2 \mu^{2-\frac{d}{2}} \int \frac{d^d k}{(2\pi)^d} \int_0^1 dy \left(\frac{\mathcal{N}'_3(k_1, k_2, k)}{(k^2 - 2k \cdot k_y)^2 k^2} + \frac{\mathcal{N}''_3(k_1, k_2, k)}{(k^2 - 2k \cdot k_y)^2 k^4} \right), \quad (2.62)$$

712 where,

$$\mathcal{N}'_3(k_1, k_2, k) = -2s + \frac{8k \cdot k_1 k \cdot k_2}{s} + (6+2\xi)(k \cdot k_1 - k \cdot k_2) + k^2(d-4) - (1-\xi)k^2. \quad (2.63a)$$

$$\mathcal{N}''_3(k_1, k_2, k) = -4(1-\xi)k \cdot k_1 k \cdot k_2. \quad (2.63b)$$

713 Differentiating eq. (2.60) with respect to a and b we get the following useful
 714 parametrisations:

$$\frac{1}{a^2 b} = \int_0^1 dx \frac{2x}{(ax + b(1-x))^3}, \quad (2.64a)$$

$$\frac{1}{a^2 b^2} = \int_0^1 dx \frac{6x(1-x)}{(ax + b(1-x))^4}. \quad (2.64b)$$

715 and taking $a = k^2 - 2k \cdot k_y$ and $b = k^2$, simplifying the denominators and performing
 716 a change of variables $K = k - xp_y$ yields:

$$\sigma_v = -\frac{4\sigma_0}{3} g_d^2 \mu^{2-\frac{d}{2}} \int \frac{d^d K}{(2\pi)^d} \int_0^1 dy \int_0^1 dx \left(\frac{2x\mathcal{N}'_3(k_1, k_2, K + xk_y)}{(K^2 - C)^3} + \right. \quad (2.65)$$

$$\left. \frac{6x(1-x)\mathcal{N}''_3(k_1, k_2, K + xk_y)}{(K^2 - C)^4} \right), \quad (2.66)$$

⁷¹⁷ where $C = x^2 p_y^2$. The change of variables modifies the numerator terms to:

$$\begin{aligned} \mathcal{N}'_3(k_1, k_2, K + xk_y) &= -2s + K^2 \left(\frac{4}{d} + d - 5 + \xi \right) \\ &\quad - (3 + \xi)xs + x^2ys(1 - y)(3 - d - \xi), \end{aligned} \quad (2.67a)$$

$$\mathcal{N}''_3(k_1, k_2, K + xk_y) = (1 - \xi) \left(x^2ys^2(1 - y) - \frac{2s}{d}K^2 \right). \quad (2.67b)$$

⁷¹⁸

⁷¹⁹ We can now perform the integrations over K with the aid of the following result:

$$\int \frac{d^d K}{(2\pi)^d} \frac{(K^2)^m}{(K^2 - C)^n} = \frac{i(-1)^{m-n}}{(4\pi)^{\frac{d}{2}}} C^{m-n+\frac{d}{2}} \frac{\Gamma(m + \frac{d}{2})\Gamma(n - m - \frac{d}{2})}{\Gamma(\frac{d}{2})\Gamma(n)}. \quad (2.68)$$

⁷²⁰ Looking at the K structure of eqs. (2.67) we can see that there are going to be 4
⁷²¹ forms of eq. (2.68) needed in this calculation. I will not show the calculation for every
⁷²² integral but will show one as an example of how the calculations can proceed. Consider
⁷²³ the contribution of the first term of eq. (2.67a):

$$I = -4s \int_0^1 dy \int_0^1 dx \int \frac{d^d K}{(2\pi)^d} \frac{1}{(K^2 - C)^3} = 4si \int_0^1 dy \int_0^1 dx (4\pi)^{-\frac{d}{2}} C^{-3+\frac{d}{2}} \frac{\Gamma(\frac{d}{2})\Gamma(3 - \frac{d}{2})}{\Gamma(\frac{d}{2})\Gamma(3)}.$$

⁷²⁴ From above we see that $C = x^2 k_y = -x^2 y(1 - y)s$ and so:

$$I = 4si(4\pi)^{-\frac{d}{2}} \Gamma(3 - \frac{d}{2})(-s)^{-3+\frac{d}{2}} \int_0^1 dy \int_0^1 dx x^{-5+d} y^{(-2+\frac{d}{2})-1} (1 - y)^{(-2+\frac{d}{2})-1}, \quad (2.69)$$

⁷²⁵ Therefore:

$$I = 4s i(4\pi)^{-\frac{d}{2}} \Gamma\left(3 - \frac{d}{2}\right) (-s)^{-3+\frac{d}{2}} \frac{1}{d-4} \frac{\Gamma^2(\frac{d}{2}-2)}{\Gamma(d-4)}. \quad (2.70)$$

726 Choosing $d = 4 + \epsilon$ (with the intention of taking the limit $\epsilon \rightarrow 0$ once it is safe to do
727 so), and manipulating the gamma functions to expose the pole structure gives:

$$-4 \int_0^1 dy \int_0^1 dxx \int \frac{d^d K}{(2\pi)^d} \frac{1}{(K^2 - C)^3} = 4(-s)^{\frac{\epsilon}{2}} i(4\pi)^{-2-\frac{\epsilon}{2}} \frac{4}{\epsilon^2} \frac{\Gamma\left(1 - \frac{\epsilon}{2}\right) \Gamma^2\left(1 + \frac{\epsilon}{2}\right)}{\Gamma(1+\epsilon)}, \quad (2.71)$$

728 which is clearly divergent in the limit $d \rightarrow 4$. The other integrals follow similarly and
729 the combined result can be expressed as:

$$\sigma_v = \frac{2\alpha_s}{3\pi} \sigma_0 \left(\frac{s}{4\pi\mu^2} \right)^{\frac{\epsilon}{2}} \frac{\Gamma\left(1 - \frac{\epsilon}{2}\right) \Gamma^2\left(1 + \frac{\epsilon}{2}\right)}{\Gamma(1+\epsilon)} \left(-\frac{8}{\epsilon^2} + \frac{6}{\epsilon} - \frac{8+4\epsilon}{1+\epsilon} \right), \quad (2.72)$$

730 where we have defined $\alpha_s = \frac{g_d^2}{4\pi}$. Expanding the product of gamma matrices for $\epsilon \rightarrow 0$
731 gives:

$$\frac{\Gamma\left(1 - \frac{\epsilon}{2}\right) \Gamma^2\left(1 + \frac{\epsilon}{2}\right)}{\Gamma(1+\epsilon)} = \frac{\gamma_E}{2} \epsilon + \left(\frac{\gamma_E^2}{8} - \frac{\pi^2}{48} \right) \epsilon^2 + \mathcal{O}(\epsilon^3), \quad (2.73a)$$

$$\left(\frac{s}{4\pi\mu^2} \right)^{\frac{\epsilon}{2}} = e^{\ln\left(\frac{s}{4\pi\mu^2}\right)^{\frac{\epsilon}{2}}} = e^{\frac{\epsilon}{2} \ln\left(\frac{s}{4\pi\mu^2}\right)} = 1 + \frac{\epsilon}{2} \ln\left(\frac{s}{4\pi\mu^2}\right) + \mathcal{O}(\epsilon^2), \quad (2.73b)$$

732 where γ_E is Euler's constant. Finally then we have:

$$\sigma_v = \frac{2\alpha_s}{3\pi} \sigma_0 \left[-\frac{8}{\epsilon^2} + \frac{1}{\epsilon} (6 - 4\gamma_E - 4L) + \gamma_E (3 - \gamma_E) \right] \quad (2.74)$$

$$- 8 + \frac{\pi^2}{6} + \pi^2 - L^2 - (2\gamma_E - 3)L \Big], \quad (2.75)$$

733 where $L = \ln\left(\frac{s}{4\pi\mu^2}\right)$. We can now see that regardless of our choice of gauge parameter,
734 ξ , the result for the vertex correction is gauge independent. We also see that the
735 parameter introduced to fix the coupling to be dimensionless appears in the final result;
736 this is often the case when using dimensional regularisation and the modified minimal
737 subtraction renormalisation scheme.

⁷³⁸ **The Real $\mathcal{O}(\alpha_s)$ Corrections**

⁷³⁹ The real gluon emission diagrams which contribute to the $\mathcal{O}(\alpha_s)$ corrections are figs.
⁷⁴⁰ (2.3e) and (2.3f). These diagrams have an indistinguishable final state and so the real
⁷⁴¹ contribution will be of the form:

$$|\mathcal{A}_r|^2 = |\mathcal{A}_{left} + \mathcal{A}_{right}|^2 = |\mathcal{A}_{left}|^2 + |\mathcal{A}_{right}|^2 + 2\mathcal{A}_{left}\mathcal{A}_{right}^*, \quad (2.76)$$

⁷⁴² where \mathcal{A}_{left} and \mathcal{A}_{right} refer to figs. (2.3e) and (2.3f) respectively and are given by:

$$\mathcal{A}_{left} = -Q e g_s T_{ij}^a \bar{u}(k_2) \gamma^\mu \frac{\not{k}_1 + \not{k}}{(k_1 + k)^2} \gamma^\nu v(k_1) \epsilon_\nu \eta_\mu, \quad (2.77a)$$

$$\mathcal{A}_{right} = -Q e g_s T_{ij}^a \bar{u}(k_2) \gamma^\nu \frac{\not{k}_2 + \not{k}}{(k_2 + k)^2} \gamma^\mu v(k_1) \epsilon_\nu \eta_\mu. \quad (2.77b)$$

⁷⁴³ In the calculation of the terms of eq. (64) it will be useful to write the energy fractions
⁷⁴⁴ for each particle as $x_i = \frac{2E_i}{\sqrt{s}}$ (where $i = 1$ is the external antiquark, $i = 2$ is the
⁷⁴⁵ antiquark and $i = 3$ is the external gluon). In terms of these invariants the contraction
⁷⁴⁶ of any two external particles simplifies to $p_i \cdot p_j = \frac{1}{2}s(1 - x_k)$ which (since we are still
⁷⁴⁷ assuming our quarks can be taken to be massless) gives a simple expression for the
⁷⁴⁸ Mandelstam variables. Evaluating the $|...|^2$ terms gives:

$$|\mathcal{A}_{left}|^2 = \frac{Q^2 e^2 g_s^2}{(k_1 + k)^4} \text{Tr}(T^a T^a) \text{Tr}(\not{k}_2 \gamma^\mu (\not{k}_1 + \not{k}) \gamma^\nu \not{k}_1 \gamma_\nu (\not{k}_1 + \not{k}) \gamma_\mu), \quad (2.78a)$$

$$|\mathcal{A}_{right}|^2 = \frac{Q^2 e^2 g_s^2}{(k_2 + k)^4} \text{Tr}(T^a T^a) \text{Tr}(\not{k}_2 \gamma^\nu (\not{k}_2 + \not{k}) \gamma^\mu \not{k}_2 \gamma_\mu (\not{k}_2 + \not{k}) \gamma_\nu), \quad (2.78b)$$

$$\mathcal{A}_{left} \mathcal{A}_{right}^* = \frac{Q^2 e^2 g_s^2}{(k_2 + k)^2 (k_1 + k)^2} \text{Tr}(T^a T^a) \text{Tr}(\not{k}_2 \gamma^\mu (\not{k}_1 + \not{k}) \gamma^\nu \not{k}_1 \gamma_\mu (\not{k}_2 + \not{k}) \gamma_\nu). \quad (2.78c)$$

⁷⁴⁹ Evaluating the trace terms in d -dimensions and rearranging in terms of the energy
⁷⁵⁰ fractions gives:

$$|\mathcal{A}_{left}|^2 = 32Q^2 e^2 g_s^2 \left(1 + \frac{\epsilon}{2}\right)^2 \frac{1 - x_1}{1 - x_2}, \quad (2.79a)$$

$$|\mathcal{A}_{right}|^2 = 32Q^2 e^2 g_s^2 \left(1 + \frac{\epsilon}{2}\right)^2 \frac{1 - x_2}{1 - x_1}, \quad (2.79b)$$

$$2\mathcal{A}_{left} \mathcal{A}_{right}^* = 64Q^2 e^2 g_s^2 \left(1 + \frac{\epsilon}{2}\right) \left(-\frac{\epsilon}{2} - 2 \frac{1 - x_3}{(1 - x_1)(1 - x_2)}\right). \quad (2.79c)$$

⁷⁵¹ Summing these expressions gives:

$$|\mathcal{A}_r|^2 = 32Q^2e^2g_s^2 \left[\left(1 + \frac{\epsilon}{2}\right)^2 \frac{x_1^2 + x_2^2}{(1-x_2)(1-x_1)} + \epsilon \left(1 + \frac{\epsilon}{2}\right) \frac{2 - 2x_1 - 2x_2 + x_1x_2}{(1-x_2)(1-x_1)} \right]. \quad (2.80)$$

⁷⁵² As with the virtual contributions we are interested in the observable cross-section and
⁷⁵³ so we must include the phase space factor for a three particle final state. Unlike the
⁷⁵⁴ two particle phase space calculation here $\int d^{3d-3}R_3$ cannot be integrated completely
⁷⁵⁵ and we are left with a differential in terms of the energy fractions defined above:

$$\frac{d^2R_3}{dx_1dx_2} = \frac{s}{16(2\pi)^3} \left(\frac{s}{4\pi}\right)^\epsilon \frac{1}{\Gamma(2+\epsilon)} \left(\frac{1-z^2}{4}\right)^{\frac{\epsilon}{2}} x_1^\epsilon x_2^\epsilon, \quad (2.81)$$

⁷⁵⁶ where $z = 1 - 2\frac{1-x_1-x_2}{x_1x_2}$. Combining eqs. (2.80) and (2.81) with a flux factor gives:

$$\frac{d^2\sigma_r}{dx_1dx_2} = \frac{2Q^2e^2g_s^2F(x_1, x_2; \epsilon)}{\pi} \left(\frac{s}{4\pi}\right)^\epsilon \frac{1}{\Gamma(2+\epsilon)} \left(\frac{1-z^2}{4}\right)^{\frac{\epsilon}{2}} x_1^\epsilon x_2^\epsilon, \quad (2.82)$$

⁷⁵⁷ where we define $F(x_1, x_2; \epsilon)$ as the algebraic factor in square brackets from eq. (2.80).
⁷⁵⁸ Switching to a dimensionless coupling and introducing α_s as above:

$$\frac{d^2\sigma_r}{dx_1dx_2} = \frac{2Q^2e^2\alpha_s}{\pi} F(x_1, x_2; \epsilon) \left(\frac{s}{4\pi\mu^2}\right)^\epsilon \frac{1}{\Gamma(2+\epsilon)} \left(\frac{1-z^2}{4}\right)^{\frac{\epsilon}{2}} x_1^\epsilon x_2^\epsilon. \quad (2.83)$$

⁷⁵⁹ Comparing with the Born cross-section in eq. (2.46) this can be written as:

$$\frac{d^2\sigma_r}{dx_1dx_2} = \frac{2\alpha_s\sigma_0}{3\pi} F(x_1, x_2; \epsilon) \left(\frac{s}{4\pi\mu^2}\right)^{\frac{\epsilon}{2}} \frac{1}{\Gamma(2+\frac{\epsilon}{2})} \left(\frac{1-z^2}{4}\right)^{\frac{\epsilon}{2}} x_1^\epsilon x_2^\epsilon. \quad (2.84)$$

⁷⁶⁰ Integrating over the allowed region of x_1 and x_2 :

$$\sigma_r = \frac{2\alpha_s\sigma_0}{3\pi} \left(\frac{s}{4\pi\mu^2}\right)^{\frac{\epsilon}{2}} \frac{1}{\Gamma(2+\frac{\epsilon}{2})} \int_0^1 dx_1 x_1^\epsilon \int_{1-x_1}^1 x_2^\epsilon \left(\frac{1-z^2}{4}\right)^{\frac{\epsilon}{2}} F(x_1, x_2; \epsilon). \quad (2.85)$$

⁷⁶¹ We can define a change of variables $x_2 = 1 - vx_1$ to decouple these integrals since:

$$\left(\frac{1-z^2}{4}\right)^{\frac{\epsilon}{2}} = \frac{x_1^2(1+v^2) - 2vx_1 + 1}{(1-x_1)x_1v} + \epsilon \frac{x_1^2(1-v+v^2-x_1+1)}{(1-x_1)x_1v} \quad (2.86)$$

$$+ \frac{\epsilon^2}{4} \frac{x_1^2(v^2-2v+1) + 4(v-1)+1}{(1-x_1)xv}. \quad (2.87)$$

⁷⁶² Substituting this into eq. (2.85) and performing the x_1 and v integrations gives:

$$\sigma_r = \frac{2\alpha_s\sigma_0}{3\pi} \left(\frac{s}{4\pi\mu^2} \right)^{\frac{\epsilon}{2}} \frac{\Gamma^2(1+\frac{\epsilon}{2})}{\Gamma(1+\frac{3\epsilon}{2})} \left[\frac{8}{\epsilon^2} - \frac{6}{\epsilon} + \frac{19}{2} \right]. \quad (2.88)$$

⁷⁶³ Further expanding the Gamma functions gives:

$$\sigma_r = \frac{2\alpha_s}{3\pi} \sigma_0 \left[\frac{8}{\epsilon^2} + \frac{1}{\epsilon} (-6 + 4\gamma_E + 4L) - \gamma_E(3 - \gamma_E) - \frac{57}{6} + \frac{7\pi^2}{6} + L^2 + (2\gamma_E - 3)L \right].$$

⁷⁶⁴ As in the case of the virtual corrections this is divergent in the limit $\epsilon \rightarrow 0$ and exhibits
⁷⁶⁵ a residual dependence on μ .

⁷⁶⁶ Cancellation of divergences

⁷⁶⁷ Having now found the vertex corrections and the real corrections up to $\mathcal{O}(\epsilon^2)$ we can
⁷⁶⁸ write the next-to-leading order cross-section by simply summing the two:

$$\sigma_{NLO} = \sigma_r + \sigma_v = \frac{\alpha_s}{\pi} \sigma_0. \quad (2.89)$$

⁷⁶⁹ So the total cross-section to next-to-leading order accuracy is:

$$\sigma = \sigma_0 \left(1 + \frac{\alpha_s}{\pi} \right) + \mathcal{O}(\alpha_s^2). \quad (2.90)$$

⁷⁷⁰ The fact that the infra-red divergences in both the real and virtual emission NLO
⁷⁷¹ diagrams cancel is an example of the KLN theorem which states that the Standard
⁷⁷² Model is completely free of infra-red divergences on the whole and holds true at all
⁷⁷³ orders.

⁷⁷⁴ **2.8.3 Resumming Higher-Order Corrections**

⁷⁷⁵ So as we have seen we can evaluate the truncated perturbative series and, provided we
⁷⁷⁶ remember to include higher multiplicity diagrams which contribute in the soft limit,
⁷⁷⁷ we will be left with a finite result which is invariant under gauge transformations.

⁷⁷⁸ It would seem then that this is the best way to proceed: we calculate as many corrections
⁷⁷⁹ as we can and reason that all of the higher-order terms we have neglected are suppressed
⁷⁸⁰ by powers of a small expansion parameter - the strong coupling, α_s . If this is indeed
⁷⁸¹ the case we should see that each time we go to a higher-order in perturbation theory
⁷⁸² our series begins to converge. E.g. the effect of the NNLO terms should be small
⁷⁸³ with respect to the NLO terms etc. It turns out that this true for all observables. To
⁷⁸⁴ motivate this we can give a schematic expansion of some variable we wish to calculate,
⁷⁸⁵ \mathcal{O} :

$$\begin{aligned} \mathcal{O} = & \alpha_s (a_1 L^2 + b_1 L + c_1 1) + \\ & \alpha_s^2 (a_2 L^4 + b_2 L^3 + c_2 L^2 + d_2 L + e_2 1) + \\ & \alpha_s^3 (a_3 L^6 + b_3 L^5 + c_3 L^4 + d_3 L^3 + e_3 L^2 + f_3 L + g_3 1) + \dots, \end{aligned} \quad (2.91)$$

⁷⁸⁶ where L is some logarithm which may be large. A fixed-order scheme aims to exactly
⁷⁸⁷ calculate some of the rows of equation 2.91 under the assumption that all subsequent
⁷⁸⁸ lines are sufficiently suppressed. The problem with this picture is that the logarithms
⁷⁸⁹ may be large enough that $\alpha_s^n L^{2n} \sim \mathcal{O}(1)$. In this case it would appear that it
⁷⁹⁰ would be better for us to calculate the first column of the terms (called the ‘leading
⁷⁹¹ logarithmic’ or simple LL approximation) that to find the the first *row* of terms (the
⁷⁹² LO approximation). Fig. 2.4 shows how the ratio of the inclusive Higgs plus three
⁷⁹³ jet cross-section to inclusive Higgs plus two jet cross-section varies as a function of the
⁷⁹⁴ rapidity gap between the two leading jets in p_T . It is shown in chapter 3 that this
⁷⁹⁵ rapidity gap is approximately equal to the logarithm, L , which we claim violates the
⁷⁹⁶ key assumptions underlying fixed-order perturbation theory. Hence, as we move to
⁷⁹⁷ large $\Delta y(j_1, j_2)$ we increase the size of L in eq. 2.91 and the terms neglected by the
⁷⁹⁸ fixed-order scheme (but captured by a LL calculation) grow in size. The ratio of the
⁷⁹⁹ inclusive $(n+1)$ -jets to n -jet cross-sections is an interesting probe of the convergence
⁸⁰⁰ of the QCD perturbative expansion since we are directly comparing the size of the
⁸⁰¹ NLO contributions to the LO terms. Fig. 2.4a shows that at a centre-of-mass energy
⁸⁰² of 14TeV (the energy scales soon to be achieved at the LHC) even at modest rapidity
⁸⁰³ intervals of around 4.0 we see that half of all events contain extra radiation and when

804 we pull the leading jets apart further in rapidity this increases to three quarters of all
805 events.

806 Furthermore, figs. 2.4b and 2.4c show that as we increase the centre-of-mass energy to
807 that of a potential hadronic future circular collider, 33TeV and 100TeV respectively,
808 these enhanced higher-order terms become even more important - in the extreme case
809 of dijets with $\Delta y(j_1, j_2) \approx 8.0$ at a 100TeV collider almost 90% of the cross-section is
810 coming from the next-to-leading term in the perturbative series: this is clear evidence
811 that is not generally sufficient to think of the expansion as being controlled by only the
812 strong coupling constant, α_s .

813 The remaining chapters of this thesis will focus on deriving a formalism for these
814 terms in the approximation for physics at the LHC and showing that they are, indeed,
815 important.

816 2.9 Parton showers for Monte-Carlo generators

817 2.10 Spinor-Helicity Notation

818 It is convenient to work in Helicity-Spinor notation to evaluate Feynman diagrams in
819 the MRK limit [?]. As usual we have:

$$| p\pm \rangle = \psi_{\pm}(p) \quad \overline{\psi_{\pm}(p)} = \langle p\pm | . \quad (2.92)$$

820 Often the helicity information will be suppressed, and we define the following shorthand:

$$\langle pk \rangle = \langle p- | k+ \rangle \quad [pk] = \langle p+ | k- \rangle . \quad (2.93)$$

821 In this scheme we have the following identities:

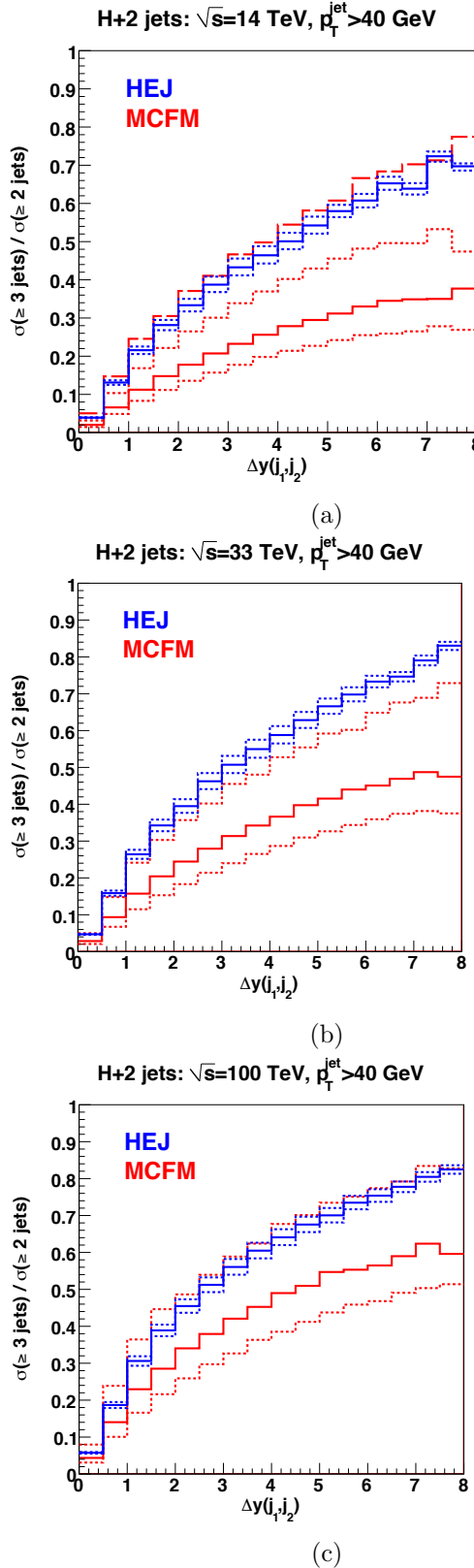


Figure 2.4: The ratio of the inclusive Higgs plus three jet cross-section to inclusive Higgs plus two jet cross-section shown for centre-of-mass energies of 14TeV (similar to the current LHC), 33TeV and 100TeV (possible energy scales for a hadronic future circular collider).

$$\langle ij \rangle [ij] = s_{ij} \quad \langle i\pm | \gamma^\mu | i\pm \rangle = 2k_i^\mu \quad (2.94)$$

$$\langle ij \rangle = -\langle ji \rangle \quad [ij] = -[ji] \quad (2.95)$$

$$\langle ii \rangle = 0 \quad [ii] = 0 \quad (2.96)$$

$$\langle i\pm | \gamma^\mu | j\pm \rangle \langle k\pm | \gamma_\mu | l\pm \rangle = 2[ik]\langle lj \rangle \quad \langle k\pm | \gamma^\mu | l\pm \rangle = \langle l\mp | \gamma^\mu | k\mp \rangle \quad (2.97)$$

$$\langle ij \rangle \langle kl \rangle = \langle ik \rangle \langle lj \rangle + \langle il \rangle \langle kj \rangle \quad [ij][kl] = [ik][jl] + [il][kj] \quad (2.98)$$

$$\langle i+ | \not{k} | j+ \rangle = [ik]\langle kj \rangle \quad \langle i- | \not{k} | j- \rangle = \langle ik \rangle [kj] \quad (2.99)$$

822 Using the momentum for the partons outlined above and the on-shell condition for the
823 external partons, $|p_i^\perp| = p_i^+ p_i^-$, we have the following:

$$\langle ij \rangle = p_i^\perp \sqrt{\frac{p_j^+}{p_i^+} - p_j^\perp} \sqrt{\frac{p_i^+}{p_j^+}}, \quad \langle ai \rangle = -i \sqrt{-\frac{p_a^+}{p_i^+} p_i^\perp}, \quad \langle ib \rangle = i \sqrt{-p_b^- p_i^+}, \quad \langle ab \rangle = -\sqrt{\hat{s}}, \quad (2.100)$$

824 where \hat{s} is the partonic centre of mass energy. In the MRK limit eq. 19 simplifies to:

$$\langle ij \rangle \approx -p_j^\perp \sqrt{\frac{p_i^+}{p_j^+}}, \quad \langle ai \rangle \approx -i \sqrt{\frac{p_a^+}{p_i^+} p_i^\perp}, \quad \langle ib \rangle \approx i \sqrt{p_i^+ p_n^-}, \quad \langle ab \rangle \approx -\sqrt{p_1^+ p_n^-}. \quad (2.101)$$

825 2.10.1 Spinor-Helicity Calculations with Massive Partons

826 To do calculations with massive partons using the spinor-helicity formalism we must be
827 very careful since all of our favourite identities and tricks rely on the spinor brackets,
828 $|i\rangle$, representing massless partons with $p_i^2 = 0$. We begin by defining ‘fundamental
829 spinors’ [?] which we can use to build more general spinors and go from there. For
830 some k_0, k_1 satisfying $k_0^2 = 0, k_1^2 = -1$ and $k_0 \cdot k_1 = 0$ we can define positive and
831 negative helicity spinors as follows:

$$u_-(k_0)\bar{u}_-(k_0) \equiv \omega_- \not{k}_0 \quad (2.102a)$$

$$u_+(k_0) \equiv \not{k}_1 u_-(k_0), \quad (2.102b)$$

where $\omega_\lambda = \frac{1}{2}(1 + \lambda\gamma^5)$ is the helicity projection operator. In order for these to be valid spinors they must satisfy the following completeness relations:

$$\sum_{\lambda} u_{\lambda}(p)\bar{u}_{\lambda}(p) = \not{p} + m \quad (2.103a)$$

$$u_{\lambda}(p)\bar{u}_{\lambda}(p) = \omega_{\lambda}\not{p} \quad (2.103b)$$

The spinors in eq. can easily be shown to satisfy these as follows:

$$\begin{aligned} u_-(k_0)\bar{u}_-(k_0) + u_+(k_0)\bar{u}_+(k_0) &= \omega_- \not{k}_0 + \not{k}_1 u_-(k_0)\bar{u}_-(k_0) \not{k}_1, \\ &= \omega_- \not{k}_0 + \not{k}_1 \omega_- \not{k}_0 \not{k}_1, \\ &= \omega_- \not{k}_0 + \frac{1}{2}\gamma^{\mu}k_{1\mu}(1 - \gamma^5)\gamma^{\nu}k_{0\nu}\gamma^{\sigma}k_{1\sigma}, \\ &= \omega_- \not{k}_0 + \frac{1}{2}k_{1\mu}k_{0\nu}k_{1\sigma}(\gamma^{\mu}\gamma^{\nu}\gamma^{\sigma} - \gamma^{\mu}\gamma^5\gamma^{\nu}\gamma^{\sigma}), \\ &= \omega_- \not{k}_0 + \frac{1}{2}k_{1\mu}k_{0\nu}k_{1\sigma}(2\gamma^{\mu}g^{\nu\sigma} - \gamma^{\mu}\gamma^{\sigma}\gamma^{\nu} + 2\gamma^5\gamma^{\mu}g^{\nu\sigma} - \gamma^5\gamma^{\mu}\gamma^{\sigma}\gamma^{\nu}), \\ &= \omega_- \not{k}_0 + k_{1\mu}k_{0\nu}k_{1\sigma}\omega_+\gamma^{\mu}(2g^{\nu\sigma} - \gamma^{\sigma}\gamma^{\nu}), \\ &= \omega_- \not{k}_0 + 2\not{k}_1 k_0 \cdot k_1 - \omega_+ \not{k}_1 \not{k}_1 \not{k}_0, \\ &= \omega_- \not{k}_0 + \omega_+ \not{k}_0, \end{aligned}$$

where we have used $\gamma^{\mu}\gamma^{\mu} = 2g^{\mu\nu}$, $\gamma^{\mu}\gamma^5 = 0$ and $\not{k}_1 \not{k}_1 = k_1^2 = 0$. This proves the property of eq. 2.103b and inserting the definition of ω_{λ} gives:

$$\begin{aligned} u_-(k_0)\bar{u}_-(k_0) + u_+(k_0)\bar{u}_+(k_0) &= \frac{1}{2}(1 - \gamma^5)\not{k}_0 + (1 + \gamma^5)\not{k}_0, \\ &= \not{k}_0, \end{aligned}$$

Which is eq. 2.103a for a massless particle.

We can use these fundamental spinors to form spinors for any given momenta, p (which

⁸³⁹ has $p^2 = 0$), as follows:

$$u_\lambda(p) = \not{p} u_{-\lambda}(k_0) \frac{1}{\sqrt{2p \cdot k_0}}, \quad (2.106)$$

⁸⁴⁰ provided we don't have $p \cdot k_0 = 0$. Once again it is easy to show that this spinor satisfies
⁸⁴¹ the necessary conditions, for example:

$$\begin{aligned} u_\lambda(p) \bar{u}_\lambda(p) &= \frac{1}{2p \cdot k_0} \not{p} u_{-\lambda}(k_0) \bar{u}_{-\lambda}(p) \not{p}, \\ &= \frac{1}{2p \cdot k_0} \not{p} \omega_{-\lambda} \not{k}_0 \not{p}, \\ &= \frac{1}{4p \cdot k_0} \not{p} (1 - \lambda \gamma^5) \not{k}_0 \not{p}, \\ &= \frac{1}{2p \cdot k_0} p_\mu k_{0\nu} p_\sigma \omega_\lambda \gamma^\mu (2g^{\nu\sigma} - \gamma^\sigma \gamma^\nu), \\ &= \frac{1}{2p \cdot k_0} \omega_\lambda (2\not{p} p \cdot k_0 - \not{p} \not{p} \not{k}), \\ &= \omega_\lambda \not{p}. \end{aligned}$$

⁸⁴² So far so good. This can also be generalised so that we can build massive spinors from
⁸⁴³ our fundamental ones. We can use

$$u(q, s) = \frac{1}{\sqrt{2q \cdot k}} (\not{q} + m) u_-(k) \quad (2.108)$$

⁸⁴⁴ to describe a quark with spin 4-vector s , mass m and momentum q . To confirm this
⁸⁴⁵ we go through the same procedure as above:

$$\begin{aligned}
 u_\lambda(p, s) \bar{u}_\lambda(p, s) &= \frac{1}{2q \cdot k_0} (\not{q} + m) u_-(k_0) \bar{u}_-(q) (\not{q} + m), \\
 &= \frac{1}{2q \cdot k_0} (\not{q} + m) \omega_- \not{k}_0 (\not{q} + m), \\
 &= \frac{1}{4q \cdot k_0} (\not{q} + m) (1 - \gamma^5) \not{k}_0 (\not{q} + m), \\
 &= \frac{1}{4q \cdot k_0} [(\not{q} \not{k}_0 \not{q} + m \not{k} \not{q} + m \not{q} \not{k}_0 + m^2 \not{k}) - \gamma^5 (\not{q} \not{k} \not{q} - m \not{k} \not{q} + m \not{q} \not{k}_0 - m^2 \not{k})], \\
 &= \frac{1}{2} \left(\not{q} + m - \gamma^5 \not{q} - m \gamma^5 + \frac{m \gamma^5 \not{k} \not{q}}{k \cdot q} + \frac{\gamma^5 m^2 \not{k}}{k \cdot q} \right), \\
 &= \frac{1}{2} \left(1 + \left(\frac{1}{m} \not{q} - \frac{m}{q \cdot k} \not{k} \right) \gamma^5 \right) (\not{q} + m), \\
 &= \frac{1}{2} (1 + \not{s} \gamma^5) (\not{q} + m),
 \end{aligned}$$

⁸⁴⁶ where the last line defines the spin vector $s = \frac{1}{m}q - \frac{m}{q \cdot k}k$. Conjecturing a similar form
⁸⁴⁷ for an antiquark spinor with spin 4-vector s , mass m and momentum q :

$$v(q, s) = \frac{1}{\sqrt{2q \cdot k}} (\not{q} - m) u_-(k), \quad (2.110)$$

⁸⁴⁸ which leads to:

$$\begin{aligned}
 v_\lambda(p, s) \bar{v}_\lambda(p, s) &= \frac{1}{2q \cdot k_0} (\not{q} - m) u_-(k_0) \bar{u}_-(q) (\not{q} - m), \\
 &= \frac{1}{2} \left((\not{q} - m) + \left(-\not{q} + m + \frac{m^2}{q \cdot k_0} \not{k}_0 - \frac{m}{q \cdot k_0} \not{q} \not{k}_0 \right) \gamma^5 \right), \\
 &= \frac{1}{2} (1 + \not{s} \gamma^5) (\not{q} - m).
 \end{aligned}$$

⁸⁴⁹ One last check that is worth performing is that these spinors actually satisfy the Dirac
⁸⁵⁰ eq. for both the quark and antiquark case. For the quark:

$$\not{q}u(q, s) = \frac{1}{2q \cdot k_0} \not{q}(\not{q} + m)u_-(k_0),$$

$$= \frac{1}{2q \cdot k_0} (m^2 + m\not{q})u_-(k_0),$$

851 we now define some momentum \tilde{q} by the relation $q = \tilde{q} + k_0$ such that $\tilde{q}^2 = 0$ and
852 $q \cdot k = \tilde{q} \cdot k$. Since $q^2 = 2\tilde{q} \cdot k = m^2$ we may write

$$\not{q}u(q, s) = \frac{1}{m} (m^2 + m\not{q})u_-(k_0),$$

$$= (m + \not{q})u_-(k_0),$$

853 we can now back substitute from the definition of $u(q, s)$ in eq. 2.108 to get:

$$\not{q}u(q, s) = \sqrt{2q \cdot k}u(q, s),$$

$$= mu(q, s),$$

854 which is the Dirac eq. for a quark. The result for antiquarks follows similarly. Now we
855 have forms for massive quarks and antiquarks in terms of massless spinors we can use
856 all of the spinor-helicity machinery to make our computations more efficient. Slightly
857 more useful forms of equations 2.108 and 2.110 can be found by decomposing q into
858 massless components once again: $q = \tilde{q} + k$ (once again this acts as a definition for \tilde{q}).
859 Then from eq. 2.108:

$$u(q, s) = \frac{1}{m} (\not{\tilde{q}} + \not{k} + m)u_-(k),$$

$$= \frac{1}{m} (|\tilde{q}^+\rangle\langle\tilde{q}^+|k^-\rangle + |\tilde{q}^-\rangle\langle\tilde{q}^-|k^-\rangle + |k^-\rangle\langle k^-|k^-\rangle + |k^-\rangle\langle k^-|k^-\rangle + m|k^-\rangle),$$

$$= \frac{[\tilde{q}k]}{m} |\tilde{q}^+\rangle + |k^-\rangle,$$

860 and similarly for the other helicities and the antiquarks:

$$u(q, -s) = \frac{\langle \tilde{q}k \rangle}{m} |\tilde{q}^- \rangle + |k^+ \rangle, \quad (2.116a)$$

$$v(q, s) = \frac{[\tilde{q}k]}{m} |\tilde{q}^+ \rangle - |k^- \rangle, \quad (2.116b)$$

$$v(q, -s) = \frac{\langle \tilde{q}k \rangle}{m} |\tilde{q}^- \rangle - |k^+ \rangle \quad (2.116c)$$

861 2.11 Monte Carlo Techniques

862 2.11.1 One Dimensional Integration

863 Integrals are ubiquitous in every field of physics and particle physics is no different.
864 We have already seen many examples where meaningful physical results can only be
865 obtained after computing an integral two good examples of this are the convolution of
866 the parton distribution functions with the partonic cross-section seen in section ?? and
867 the more complex multi-dimensional integrals seen in section ?? the calculation of the
868 one-loop correction to quark-antiquark production.

869 For some of the integrals derived here it is not always feasible (and sometimes not even
870 possible) to calculate them analytically. In these situations we must use a numerical
871 approach to approximate the full result. Such approaches generally fall into one of
872 two categories; quadrature or Monte-Carlo random sampling approaches. The most
873 appropriate solution depends the integrand itself (and in particular our prior knowledge
874 of the integrand) and the number of dimensions we are integrating over.

875 Here we briefly consider the one-dimensional case. Given an integral:

$$I = \int_a^b f(x) dx, \quad (2.117)$$

876 we can use well known results such as the Compound Simpson's Rule to approximate
877 the integral by

$$I \approx \frac{h}{3} \sum_{i=0}^{N/2} (f(x_{2i-2}) + 4f(x_{2i-1}) + f(x_{2i})) + \mathcal{O}(N^{-4}), \quad (2.118)$$

878 where N is the number of times we have subdivided the integral range (a, b) and

879 $x_i = a + \frac{i(b-a)}{N}$ are the points at which we sample the integrand. The error quoted
 880 on eq. 2.118 only shows the dependence on the sampling rate and it should be noted
 881 that there are other factors arising from the size of the domain of integration and on
 882 derivatives of the integrand, $f(x)$. The N^{-4} scaling of the error in this method makes
 883 it a good choice for numerics in one-dimension.

884 The Monte-Carlo approach to approximating eq. (2.117) would be to (pseudo-
 885)randomly select a series of N points, x_i , from within the domain of integration and
 886 then compute the integral as follows:

$$I \approx I_{MC} = \frac{b-a}{N} \sum_{i=0}^N f(x_i) + \mathcal{O}(N^{-\frac{1}{2}}). \quad (2.119)$$

887 Convergence of this result is assured by the weak law of large numbers (also known
 888 as Bernoulli's Theorem) which states that for a series of independent and identically
 889 distributed random variables, X_1, \dots, X_N , each with $\mathbb{E}(X_i) = \mu$ the sample mean
 890 approaches the population mean as $N \rightarrow \infty$. That is,

$$\lim_{N \rightarrow \infty} \frac{X_1 + \dots + X_N}{N} = \mu. \quad (2.120)$$

891 We can see this explicitly since the expectation of I_{MC} under the continuous probability
 892 density function p is:

$$\begin{aligned} \mathbb{E}_p[I_{MC}] &= \mathbb{E}_p \left[\frac{b-a}{N} \sum_{i=0}^N f(x_i) \right] \\ &= \frac{b-a}{N} \sum_{i=0}^N \mathbb{E}_p [f(x_i)] \\ &= \frac{b-a}{N} \sum_{i=0}^N \int_{-\infty}^{+\infty} f(x)p(x)dx \end{aligned}$$

where $p(x) = \frac{1}{b-a}$ is the uniform probability distribution for $x \in (a, b)$. Hence,

$$\begin{aligned} \mathbb{E}_p[I_{MC}] &= \frac{b-a}{N} \frac{1}{b-a} \sum_{i=0}^N \int_a^b f(x)dx \\ &= \int_a^b f(x)dx = I. \end{aligned}$$

893 Since the convergence of the Monte-Carlo approximation clearly scales significantly
 894 worse than the case for quadrature it would seem that it is not worth considering and,
 895 indeed, for a single dimension it is not. However, the picture changes when we consider
 896 integrals in dimension $d \geq 2$.

897 **2.11.2 Higher Dimensional Integration**

898 In the case of higher dimensional integrals e.g.

$$I = \int_{[a,b]} f(\vec{x}) d\vec{x} = \int_{x_1=a_1}^{x_1=b_1} \cdots \int_{x_n=a_n}^{x_n=b_n} f(x_1, \dots, x_n) dx_1 \dots dx_n, \quad (2.121)$$

899 we can still look to generalisations of the quadrature methods touched on in section
 900 2.11.1 however the convergence of these methods is less favourable. Quadrature
 901 methods have errors which scale with the number of dimensions we are integrating
 902 over, e.g. $\mathcal{O}(N^{-\frac{4}{d}})$ for the compound Simpson's rule. We can argue this intuitively
 903 since if we have N points in one dimension to get an error which scales as $\mathcal{O}(N^{-4})$ then
 904 in two dimensions we would require N^2 to achieve the same density of samplings and
 905 hence $N^2 \sim \mathcal{O}(N^{-4}) \implies N^2 \sim \mathcal{O}(N^{-\frac{4}{2}})$ and more generally $\mathcal{O}(N^{-\frac{4}{d}})$.

906 By comparison the error of a Monte Carlo approximation stays fixed at $\mathcal{O}(N^{-\frac{1}{2}})$
 907 regardless of the number of dimensions in the integrals. We are spared from this so-
 908 called ‘curse of dimensionality’ by the Central Limit Theorem which states that for a
 909 sequence of independent and identically distributed random variables X_1, \dots, X_N each
 910 with variance σ^2 we have:

$$\frac{X_1 + \dots + X_N - N\mathbb{E}(X_1)}{\sqrt{N}\sigma} \xrightarrow{\lim N \rightarrow \infty} \mathcal{N}(0, 1), \quad (2.122)$$

911 where $\mathcal{N}(0, 1)$ is the normal distribution with mean zero and variance 1. Then using
 912 the additive and multiplicative scaling of the normal distribution we see that:

$$\sum_{i=1}^N X_i \xrightarrow{\lim N \rightarrow \infty} \mathcal{N}\left(\mu, \frac{\sigma^2}{N}\right), \quad (2.123)$$

913 where μ is the mean of the variables X_i . The variance of a normal distribution is well
 914 known and we can use this to see that for a d -dimensional integral we can approximate
 915 our uncertainty as:

$$\int_{[a,b]} f(\vec{x}) d\vec{x} = V \langle f \rangle \pm V \sqrt{\frac{\langle f^2 \rangle - \langle f \rangle^2}{N}} \quad (2.124)$$

$$\equiv V \langle f \rangle \pm V \frac{\sigma_{MC}}{\sqrt{N}}, \quad (2.125)$$

where V is the volume of the domain of integration, $\langle f \rangle = \sum_i f(x_i)$ and $\langle f^2 \rangle = \sum_i f(x_i)^2$.

2.11.3 Variation Reduction Techniques

In equation 2.125 we saw that the error estimate of a Monte Carlo approximation depends not only on the number of points sampled, N , but also on σ_{MC} . We can try to reduce σ_{MC} by reducing how ‘variable’ the integrand is over the domain of integration, for instance in the extreme example where our integrand is $f(x) = f_0$, a constant, it is clear that one Monte Carlo sample is sufficient to compute the integral exactly. Previously when computing $\mathbb{E}_p[I_{MC}]$ we used a uniform probability density function but we are free to use any distribution we like to perform the integration. This can be seen since:

$$\begin{aligned} \mathbb{E}_p[I_{MC}] &= \int f(x)p(x)dx, \\ &= \int \frac{f(x)p(x)q(x)}{q(x)}, \\ &= \mathbb{E}_q \left[\frac{I_{MC}p(x)}{q(x)} \right], \end{aligned}$$

where $q(x)$ is our ‘importance sampling’ distribution. For example let us consider the integral

$$I = 150 \int_0^{\frac{1}{2}} x^2 \arcsin x^2 dx. \quad (2.126)$$

The integrand of eq. 2.126 is shown in fig. 2.5 along with two potential choices of density functions. The uniform distribution (shown in red) will sample the integrand equally across the domain however it is clear from looking at the functional form of

eq. 2.126 that that isn't the most efficient approach since it is strongly peaked towards the right hand side of the domain. Hence that is where the largest contribution to the Monte Carlo sum will come from. However if we sample the modified integrand using pseudo-random numbers generated from a distribution proportional to x^4 (shown in green in fig. 2.5) we can reduce the variance of our approximation significantly. Tab. 2.2 shows how the approximation improves as we vary the number of samples, N , for the two cases of $q \sim \mathcal{U}(0, 0.5)$ and $q \sim x^4$.

N	$q \sim \mathcal{U}(0.0, 0.5)$		$q \sim x^4$	
	Approximation	Error	Approximation	Error
10^1	0.5111428 ± 1.5932607	0.4318912	0.9424279 ± 1.6817093	0.0006061
10^2	0.9098668 ± 2.0212007	0.0331672	0.9429298 ± 2.6653523	0.0001042
10^3	0.9456974 ± 2.0415918	0.0026633	0.9431454 ± 0.8430513	8.936×10^{-5}
10^4	0.9438040 ± 2.0222993	0.0007699	0.9430386 ± 0.2665659	4.504×10^{-6}
10^5	0.9337252 ± 2.0040391	0.0093088	0.9430241 ± 0.0842942	2.848×10^{-6}

Table 2.2: The Monte-Carlo approximation to equation 2.126 as we vary the number of sampled points, N , shown in the naive sampling case and in the importance sampled case.

Tab. 2.2 clearly shows the value of an importance sampling approach convergences to the correct result much faster than when we sample uniformly. Of course this tactic relies on us having some prior knowledge of the behaviour of our integrand in order to select the correct probability density function to use which, in more complicated examples is not always possible³. A more realistic, and relevant, example of importance sampling comes from the cross-section for the production of a Z^0 boson in association with dijets. The matrix element squared for such a process will have following form upon factoring out the Z^0 propagator squared:

$$|\mathcal{M}_{Z^0+jj}|^2 \sim \left| \frac{1}{p_Z^2 - M_Z^2 + i\Gamma_Z M_Z} \right|^2 \times f(\text{QCD, EW}) \times g(\text{Kinematic}), \quad (2.127)$$

where p_Z is the momentum carried by the Z^0 boson, M_Z is its mass, Γ_Z is its width and $f(\text{QCD, EW})$ will contain all of the coupling information and $g(\text{Kinematic})$ encodes the remainder of the matrix element. When using a Monte-Carlo approach to generate events of this kind we can use the schematic of 2.127 to *a priori* select an appropriate probability density function to sample from. Fig. 2.6 shows the squared Z^0 propagator. Obvious comparisons with fig. 2.5 can be drawn in the sense that were we to generate

³More novel approaches whereby the sampling distribution is modified to improve convergence as the Monte-Carlo iterations are calculated, such as the VEGAS algorithm, exist but they will not be discussed here.

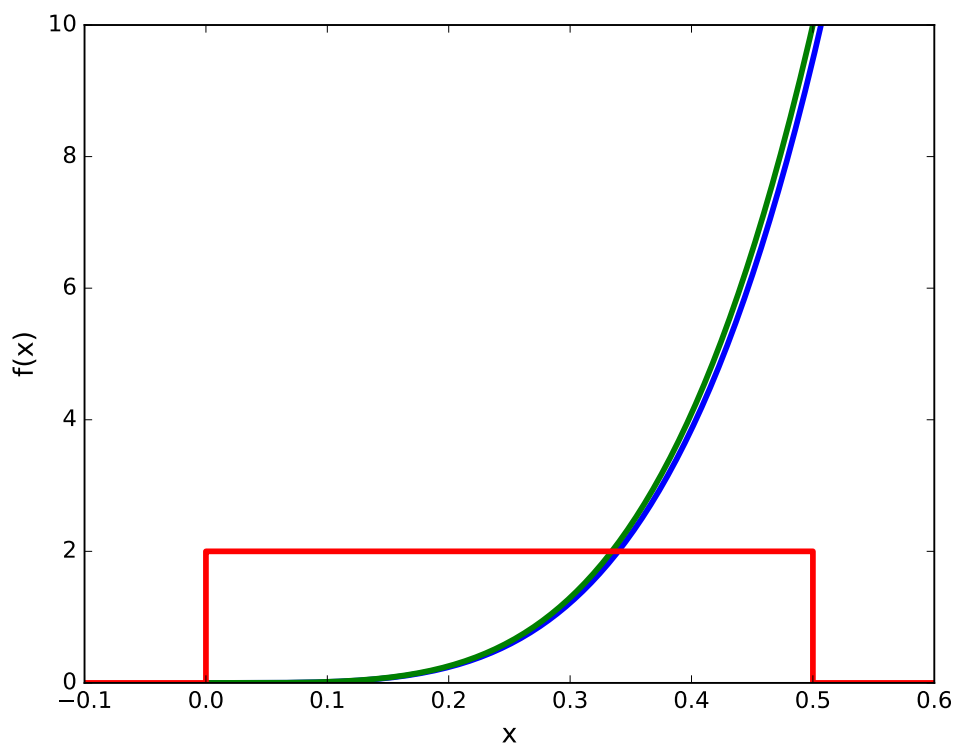


Figure 2.5: A simple importance sampling example (see equation 2.126). The integrand, $f(x)$, is shown in blue, the importance sampling distribution is shown in green and, for comparison, the uniform probability density function used in the naive case of no importance sampling is also shown (in red).

953 events with a uniform spread of values for p_Z^2 we would end with a very slow rate
 954 of convergence by oversampling areas where the integrand is very small and slowly
 955 varying.

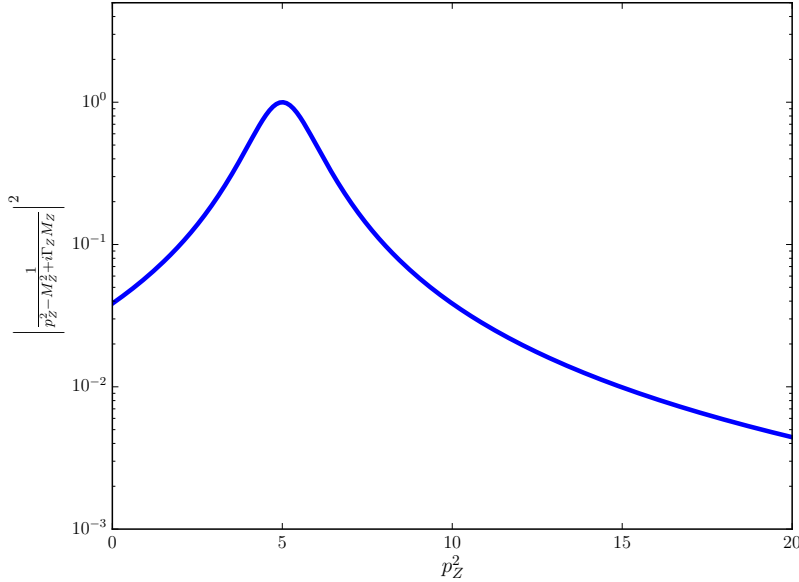


Figure 2.6: The absolute value squared of the Z^0 propagator for a range of values of the invariant mass squared of the Z^0 , p_Z^2 . We can see it is strongly peaked at the Z^0 mass and, as such, is an ideal candidate for using importance sampling.

956 Another good example of importance sampling is found in how we sample the incoming
 957 partons in our simulations. Simple momentum conservation considerations lead us to
 958 values for the Bjorken scaling variables of our incoming partons, x_a and x_b , and we can
 959 use these to intelligently sample the available partons. The naive way to perform the
 960 sum over all possible incoming states would be to uniformly choose a random number
 961 corresponding to one of the light quarks, one the light anti-quarks or to a gluon⁴. We
 962 can, however, do better than this by using what we know about how the parton density
 963 functions vary with $x_{a/b}$ - fig. ?? shows this behaviour as measured by the HERA
 964 experiment. By choosing to randomly sample then incoming parton types according
 965 to the relative values for the parton density functions we can, once again, reduce the
 966 variance of our numerical integrations as much as possible.

⁴By ‘light (anti-)quarks’ we mean all except the top and anti-top. The parton density functions for these are not available and, even if they were, they would be small enough that we could safely ignore their contribution to cross-sections.

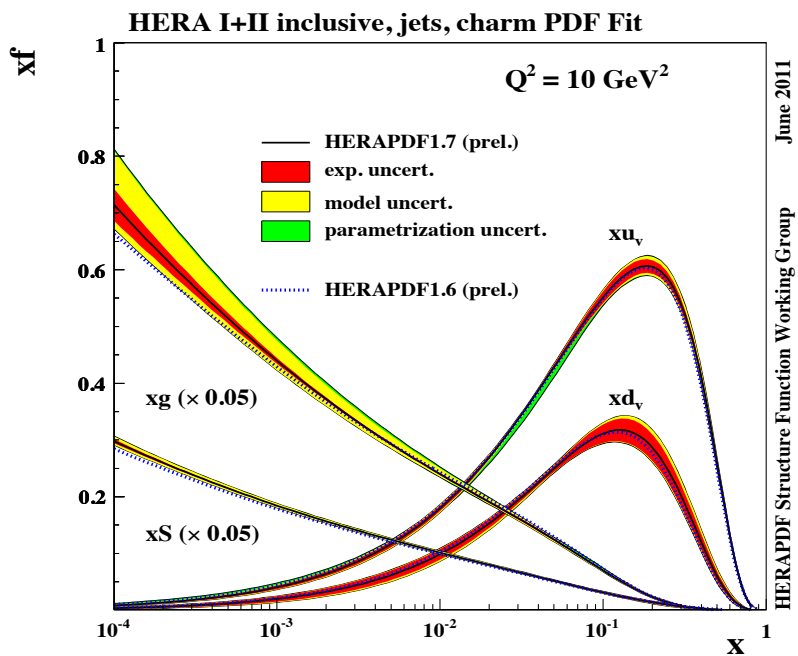


Figure 2.7: Recent parton distribution function fits from the HERA experiment. The observed variation in $f(x_{a/b}, Q^2)$, especially at high $x_{a/b}$, can be exploited when computing the equation ?? by using an importance sampling approach

967 **Chapter 3**

968 **High Energy QCD**

969 **3.1 The High Energy Limit of $2 \rightarrow 2$ QCD scattering**

970 **3.1.1 Mandelstam Variables in the High Energy Limit**

971 The $2 \rightarrow 2$ QCD scattering amplitudes can be expressed in terms of the well-known
972 Mandelstam variables s, t and u . Which, in terms of the momenta in the process, are
973 given by:

$$s = (p_1 + p_2)^2 \quad (3.1a)$$

$$t = (p_1 - p_2)^2 \quad (3.1b)$$

$$u = (p_2 - p_3)^2 \quad (3.1c)$$

974 When working in the high energy limit it is convenient to re-express these in terms of
975 the perpendicular momentum of the outgoing partons, p_\perp , and the difference in rapidity
976 between the two final state partons, Δy :

$$s = 4p_\perp^2 \cosh^2 \frac{\Delta y}{2} \quad (3.2a)$$

$$t = -2p_\perp^2 \cosh \frac{\Delta y}{2} e^{-\frac{\Delta y}{2}} \quad (3.2b)$$

$$u = -2p_\perp^2 \cosh \frac{\Delta y}{2} e^{\frac{\Delta y}{2}} \quad (3.2c)$$

977 In the limit of hard jets well separated in rapidity these can be approximated to give

$$s \approx p_{\perp}^2 e^{\Delta y} \quad (3.3a)$$

$$t \approx -p_{\perp}^2 \quad (3.3b)$$

$$u \approx -p_{\perp}^2 e^{\Delta y} \quad (3.3c)$$

From eq. (above) it is clear that the ‘hard, wide-angle jet’ limit is equivalent to the High Energy limit since:

$$\Delta y \approx \ln \left(\frac{s}{-t} \right) \quad (3.4)$$

3.1.2 HE limit of the three-gluon vertex

The three gluon vertex shown in fig. (X) has the following Feynman rule:

$$g_s f^{abc} ((p_1 + p_3)^{\nu} g^{\mu_1 \mu_3} + (q - p_3)^{\mu_1} g^{\mu_3 \nu} - (q + p_1)^{\mu_3} g^{\mu_1 \nu}) \quad (3.5)$$

In the high energy limit the emitted gluon with momenta q is much softer than the emitting gluon with momenta p_1 i.e. $p_1^{\mu} \gg q^{\mu} \forall \mu$ and therefore $p_1 \sim p_3$ - using this we can approximate the vertex by

$$\approx g_s f^{abc} (2p_1^{\nu} g^{\mu_1 \mu_3} + p_3^{\mu_1} g^{\mu_3 \nu} - p_3^{\mu_3} g^{\mu_1 \nu}) \quad (3.6)$$

Furthermore, since the hard gluons in a high energy process are external they must satisfy the Ward identities; $\epsilon_1 \cdot p_1 = \epsilon_3 \cdot p_3 = 0$. Hence, the vertex can be expressed simply as:

$$\approx 2g_s f^{abc} p_1^{\nu} g^{\mu_1 \mu_3} \quad (3.7)$$

3.1.3 At Leading Order in α_s

Talk through the limit of $2 \rightarrow 2$ scattering of gluons. Introduce mandelstam variables, show the equivalence of large delta y and large s.

⁹⁹¹ **3.1.4 At Next-to-Leading Order in α_s**

⁹⁹² Calculate the NLO calculations to the 2j ME and show that there explicitly is a delta
⁹⁹³ y (large log) enhancement.

⁹⁹⁴ **3.1.5 High Energy Jets ‘Currents’**

⁹⁹⁵ **3.1.6 Effective Vertices For Real Emissions**

⁹⁹⁶ **3.2 High Energy Jets**

⁹⁹⁷ **3.2.1 The Multi-Regge Kinematic limit of QCD amplitudes**

⁹⁹⁸ **3.2.2 Logarithms in HEJ observables**

⁹⁹⁹ Here you should take a $2 \rightarrow n$ ME, apply the HE limit to it, do a PS integration and
¹⁰⁰⁰ show the logs you get. Need the HE limit of PS integral from JA thesis and/or from
¹⁰⁰¹ VDD talk

¹⁰⁰² **3.2.3 HEJ currents**

¹⁰⁰³ **3.2.4 High Energy Phase-space Integration**

1004 **Chapter 4**

1005 **$Z/\gamma^* + \text{Jets}$ at the LHC**

1006 • Rewrite the bits Jenni/Jeppe wrote.

1007 The Large Hadron Collider (LHC) sheds ever more light on Standard Model processes
1008 at higher energies as it continues into Run II. One “standard candle” process for the
1009 validation of the Standard Model description in this new energy regime is the production
1010 of a dilepton pair through an intermediate Z boson or photon, in association with (at
1011 least) two jets [2–4, 27, 30, 50, 51]. This final state can be entirely reconstructed from
1012 visible particles (in contrast to $pp \rightarrow \text{dijets} + (W \rightarrow e\nu)$) making it a particularly
1013 clean channel for studying QCD radiation in the presence of a boson. Experimentally
1014 this process is indistinguishable from the production of a virtual photon which has
1015 decayed into the same products and we will consider both throughout.

1016 W and Z/γ^* -production are excellent benchmark processes for investigating QCD
1017 corrections, since the mass of the boson provides a perturbative scale, while the event
1018 rates allow for jet selection criteria similar to those applied in Higgs boson studies.
1019 $W, Z/\gamma^*$ -production in association with dijets is of particular interest, since in many
1020 respects it behaves like a dijet production emitting a weak boson (i.e. electroweak
1021 corrections to a QCD process rather than QCD corrections to a weak process). This
1022 observation means that a study of $W, Z/\gamma^*$ -production in association with dijets is
1023 relevant for understanding Higgs-boson production in association with dijets (which in
1024 the gluon-fusion channel can be viewed as a Higgs-boson correction to dijet production).
1025 This process is interesting (e.g. for CP -studies) in the region of phase space with
1026 large dijet invariant mass, where the coefficients in the perturbative series have
1027 logarithmically large contributions to all orders. As an example of the increasing
1028 importance of the higher orders, it is noted that the experimental measurement of
1029 the $N + 1/N$ -jet rate in $Z/\gamma^* + \text{jets}$ increases from 0.2 to 0.3 after application of very

1030 modest VBF-style selection cuts even at 7 TeV [2, 3, 27].

1031 The current state-of-the-art for fixed-order calculations for this process is the next-to-
 1032 leading order calculation of Z/γ^* plus 4 jets by the BlackHat collaboration [47]. While
 1033 it has become standard to merge next-to-leading order QCD calculations with parton
 1034 showers [9, 12, 37–39, 58], results for jet production in association with vector bosons
 1035 have so far only appeared with up to two jets [25, 60]. Indeed, $W/Z + 0-, 1-$ and
 1036 2-jet NLO samples have been merged with higher-order tree-level matrix elements
 1037 and parton shower formulations [36, 45]. However, a parton shower cannot be expected
 1038 to accurately provide a description of multiple hard jets from its resummation of the
 1039 (soft and collinear) logarithms which are enhanced in the region of small invariant
 1040 mass. An alternative method to describe the higher-order corrections is instead to sum
 1041 the logarithmic corrections which are enhanced at large invariant mass between the
 1042 particles. This is the approach pioneered by the High Energy Jets (HEJ) framework [15,
 1043 16]. Here, the hard-scattering matrix elements for a given process are supplemented
 1044 with the leading-logarithmic corrections (in s/t) at all orders in α_s . This approach
 1045 has been seen to give a good description of dijet and W plus dijet data at both the
 1046 TeVatron [8] and the LHC [1, 5, 6, 28, 29]. In particular, these logarithmic corrections
 1047 ensure a good description of W plus dijet-production in the region of large invariant
 1048 mass between the two leading jets [6]. It is not surprising that standard methods
 1049 struggle in the region of large invariant mass, since the perturbative coefficients receive
 1050 large logarithmic corrections to all orders, and perturbative stability is guaranteed only
 1051 once these are systematically summed.

1052 The purpose of this paper is to develop the treatment of such large QCD perturbative
 1053 corrections within High Energy Jets to include the process of Z/γ^* plus dijets. While
 1054 this process has many features in common with the W plus dijets process, one major
 1055 difference is the importance of interference terms, both between different diagrams
 1056 within the same subprocess (e.g. $qQ \rightarrow qQ(Z \rightarrow) e^+ e^-$ with emissions off either the
 1057 q or Q line) and between Z and γ^* processes of the same partonic configuration. For
 1058 processes with two quark lines, the possibility to emit the Z/γ^* from both of these leads
 1059 to profound differences to the formalism, since the t -channel momentum exchanged
 1060 between the two quark lines obviously differs whether the boson emission is off line q
 1061 or Q . Furthermore, the interference between the two resulting amplitudes necessitates
 1062 a treatment at the amplitude-level. High Energy Jets is formulated at the amplitude-
 1063 level, which, together with the matching to high-multiplicity matrix-elements, sets it
 1064 apart in the field of high energy logarithms [18, 26, 32, 34, 48, 49, 53–55]. The added
 1065 complication over earlier High Energy Jets-formalism (and indeed in any BFKL-related
 1066 study) by the interfering t -channels introduces a new structure of divergences in both

1067 real and virtual corrections, and therefore a new set of subtraction terms are needed,
1068 in order to organise the cancellation of these divergences. The matching to full high-
1069 multiplicity matrix elements puts the final result much closer to those of fixed order
1070 samples merged according to the shower formalism [25, 36, 45, 60] — although of course
1071 the logarithms systematically controlled with High Energy Jets are different to those
1072 controlled in the parton shower formalism. In particular, High Energy Jets remains a
1073 partonic generator, i.e. although it is an all-order calculation (like a parton shower), it
1074 is not interfaced to a hadronisation model. Initial steps in combining the formalism of
1075 High Energy Jets and that of a parton shower (and hadronisation) were performed in
1076 Ref. [14].

We begin the main body of this article by outlining the construction of a High Energy Jets amplitude and its implementation in a fully flexible parton level Monte Carlo in the next section. In section ?? we derive the new subtraction terms which allows us to fully account for interference between the amplitudes. The subtraction terms allow for the construction of the all-order contribution to the process as an explicit phase-space integral over any number of emissions. Specifically, the main result for the all-order summation is formulated in Eq. (??):

$$\sigma = \sum_{f_a, f_b} \sum_{n=2}^{\infty} \int \frac{d^3 p_a}{(2\pi)^3 2E_a} \int \frac{d^3 p_b}{(2\pi)^3 2E_b} \left(\prod_{i=2}^n \int_{p_{i\perp} > \lambda_{cut}} \frac{d^3 p_i}{(2\pi)^3 2E_i} \right) (2\pi)^4 \delta^{(4)} \left(p_a + p_b - \sum_i p_i \right) \\ \times | \mathcal{M}_{f_a f_b \rightarrow Z/\gamma^* f_a(n-2) g f_b}^{HEJ-reg}(p_a, p_b, \{p_i\}) |^2 \frac{x_a f_{fa}(x_a, Q_a) x_b f_{fb}(x_b, Q_b)}{\hat{s}^2} \Theta_{cut},$$

1077 where σ is the sough-after cross section, and the rest of the equation is discussed in
1078 the relevant section. Section ?? also discusses the necessary modifications in order
1079 to include fixed-order matching. In section ?? we show and discuss the comparisons
1080 between the new predictions obtained with High Energy Jets and LHC data. We
1081 conclude and present the outlook in section ??.

1082 4.1 $Z+jets$

1083 Similarly to the the case of W^\pm plus jets there are *four* possible emission sites for the
1084 boson; Two on the forward incoming quark, and two on the backward incoming quarks
1085 (see fig. 4.1).

1086 In the language of currents (see for *e.g.* [?]) we call the left hand side of fig. 4.1 j_μ^Z / γ^* :

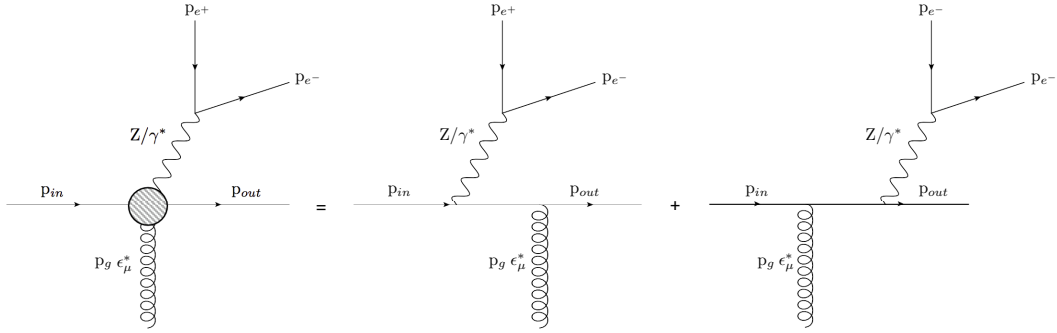


Figure 4.1: The possible emission sites for a neutral weak boson.

$$j_\mu^Z = \bar{u}^{h_{out}}(p_{out}) \left(\gamma^\sigma \frac{\not{p}_{out} + \not{p}_Z}{(p_{out} + p_Z)^2} \gamma_\mu + \gamma_\mu \frac{\not{p}_{in} - \not{p}_Z}{(p_{in} - p_Z)^2} \gamma_\sigma \right) u^{h_{in}}(p_{in}) \times \bar{u}^{h_{e^-}}(p_{e^-}) \gamma_\sigma u^{h_{e^+}}(p_{e^+}). \quad (4.1)$$

1087 We can then express amplitudes in terms of contractions of ‘emitting’ and ‘non-emitting’
 1088 currents.

1089 As the fig. above indicates, when emitting a Z boson there is also the possibility of
 1090 an off-shell photon being exchanged instead of a Z . Since the difference in these two
 1091 channels is indistinguishable in the final state we must treat the interference as the
 1092 amplitude level. For example, the amplitude for $2 \rightarrow 2$ scattering is:

$$\mathcal{A}_{Z/\gamma}^{2 \rightarrow 2} = \underbrace{\left(\frac{k_1}{p_{Z/\gamma}^2 - m_Z^2 + i\Gamma_Z m_Z} + \frac{Q_1 e}{p_{Z/\gamma}^2} \right)}_{\mathcal{K}_a} \frac{j_1^{Z/\gamma} \cdot j_2}{q_{t1}^2} + \underbrace{\left(\frac{k_2}{p_{Z/\gamma}^2 - m_Z^2 + i\Gamma_Z m_Z} + \frac{Q_2 e}{p_{Z/\gamma}^2} \right)}_{\mathcal{K}_b} \frac{j_1 \cdot j_2^{Z/\gamma}}{q_{b1}^2}, \quad (4.2)$$

1093 where k_i are the Z couplings to the quarks, Q_i are the the γ couplings to the quarks,
 1094 m_Z is the mass of the Z , Γ_Z is the width of the Z peak, q_{t1} is the momentum of
 1095 the t -channel gluon exchanged when Z emission occurs of the forward incoming quark
 1096 line and q_{b1} is the momentum of the exchanged gluon when Z emission occurs of the
 1097 backward incoming quark line.

1098 Eq. (4.2) is a good example of the advantages of using currents since the form of the
 1099 diagrams for either Z or γ can be expressed as only two contraction (with the distinct
 1100 propagators dealt with in the \mathcal{K}_i terms).

1101 Extra *real* gluon emissions from the t -channel gluon are then included using an effective
 1102 vertex of the form [?] [?]:

$$V^\rho(q_j, q_{j+1}) = -(q_j + q_{j+1})^\rho - 2 \left(\frac{s_{aj}}{s_{ab}} - \frac{q_{j+1}^2}{s_{bj}} \right) p_b^\rho + 2 \left(\frac{s_{bj}}{s_{ab}} + \frac{q_j^2}{s_{aj}} \right) p_a^\rho, \quad (4.3)$$

¹¹⁰³ where $s_{aj} = 2p_a \cdot p_j$ etc. The general $2 \rightarrow n$ amplitude therefore looks like:

$$\begin{aligned} \mathcal{A}_{Z/\gamma}^{2 \rightarrow n} = & \left(\mathcal{K}_a \frac{V^{\mu_1}(q_{t1}, q_{t2}) \cdots V^{\mu_{n-2}}(q_{t(n-1)}, q_{t(n-2)})}{q_{t1} \cdots q_{t(n-1)}} j_1^Z \cdot j_2 + \dots \right. \\ & \left. \mathcal{K}_b \frac{V^{\mu_1}(q_{b1}, q_{b2}) \cdots V^{\mu_{n-2}}(q_{b(n-1)}, q_{b(n-2)})}{q_{b1} \cdots q_{b(n-1)}} j_1 \cdot j_2^Z \right) \epsilon_{\mu_1}^* \cdots \epsilon_{\mu_{(n-2)}}^* \end{aligned} \quad (4.4)$$

¹¹⁰⁴ and after taking the modulus squared of this we have the following:

$$\begin{aligned} |\mathcal{A}_{Z/\gamma}^{2 \rightarrow n}|^2 = & \left| \mathcal{K}_a j_1^{Z/\gamma} \cdot j_2 \right|^2 \frac{V^2(q_{t1}, q_{t2}) V^2(q_{t2}, q_{t3}) \cdots V^2(q_{b(n-2)}, q_{b(n-1)})}{q_{t1}^2 \cdots q_{t(n-1)}^2} + \dots \\ & \left| \mathcal{K}_b j_2^{Z/\gamma} \cdot j_1 \right|^2 \frac{V^2(q_{b1}, q_{b2}) V^2(q_{b2}, q_{b3}) \cdots V^2(q_{b(n-2)}, q_{b(n-1)})}{q_{b1}^2 \cdots q_{b(n-1)}^2} + \dots \\ & 2\Re \{ \mathcal{K}_a \overline{\mathcal{K}_b} \times (j_1^{Z/\gamma} \cdot j_2) (\overline{j_2^{Z/\gamma} \cdot j_1}) \} \frac{V(q_{t1}, q_{t2}) \cdot V(q_{b1}, q_{b2}) \cdots V(q_{t(n-2)}, q_{t(n-1)}) \cdot V(q_{b(n-2)}, q_{b(n-1)})}{q_{t1} q_{b1} \cdots q_{t(n-1)} q_{b(n-1)}} \end{aligned} \quad (4.5)$$

¹¹⁰⁵ In previous work it was seen that the interference between forward quark- and backward
¹¹⁰⁶ weak boson emission (the third term in eq. (4.5)) was negligible [?]. This turns out
¹¹⁰⁷ not to be the case in Z plus jets - possibly due to the effects of photon interference.

1108 4.1.1 Formulation in terms of currents

1109 4.1.2 To High Multiplicity Final States

1110 4.1.3 Z^0 Emission Interference

1111 4.1.4 Photonic Interference

1112 4.1.5 The $2 \rightarrow n$ Matrix Element

1113 4.1.6 The Differential Z/γ Cross-Section

1114 4.2 Regularising the $Z/\gamma^* + \text{Jets}$ Matrix Element

1115 Explain that in the MRK limit the external legs can't (by definition) be soft, then look
1116 at the limit of one gluon going soft (basically an NLO correction to the (n-1) parton
1117 ME) in the effective vertex. Show that this leads to a divergence.

1118 Next talk about NLO virtual corrections to the (n-1)-parton ME. Show that in the HE
1119 limit, only two diagrams contribute (extra t - crosses and uncrossed - g exchange) show
1120 the log enhancement given. Give explicitly calculation showing divergences cancelling
1121 (as must happen by KLN theorem).

1122 4.2.1 Soft Emissions

1123 To calculate useful quantities such as cross sections *etc.* we must integrate equation (4.5)
1124 over all of phase space. However, problems arise when we attempt to integrate over
1125 the so called 'soft' (low energy) regions of phase space - things which should be finite
1126 diverge and need to be cancelled carefully. It is well understood that the divergences
1127 coming from soft *real* emissions cancel with those coming from soft *virtual* emissions
1128 and so we must explicitly show this cancellation and calculate the remaining finite
1129 contribution multiplying the $(n - 1)$ -final state parton matrix element.

1130 In the previous work on W^\pm emission the finite contribution was found to be [?][?]:

$$\frac{\alpha_s C_a \Delta_{j-1,j+1}}{\pi} \ln \frac{\lambda^2}{|\vec{q}_{j\perp}|^2}, \quad (4.6)$$

1131 where α_s is the strong coupling strength, C_a is a numerical factor, $\Delta_{i-1,i+1}$ is the
1132 rapidity span of the final state partons either side of our soft emission, λ is a factor

1133 chosen to define the soft region: $p^2 < \lambda^2$ and $|\vec{q}_{j\perp}|^2$ is the sum of squares of the
 1134 transverse components of the j^{th} t -channel gluon momenta.

1135 Here we investigate the cancellation of these divergences for Z emission and most
 1136 importantly whether the finite term is of the same form for the interference term which
 1137 was previously disregarded.

1138 We start by looking at a $2 \rightarrow n$ process and take the limit of one final state parton
 1139 momentum, p_i , becoming small. Because of the form of eq. (4.5) this amounts to
 1140 looking at the effect of soft-ness on eq. (4.3), we can immediately see that for p_i going
 1141 soft the gluon chain momenta coming into- and coming out of the j^{th} emission site will
 1142 coincide: $q_{j+1} \sim q_j$:

$$V^\rho(q_j, q_{j+1}) \rightarrow -2q_j^\rho - 2 \left(\frac{s_{aj}}{s_{ab}} - \frac{q_j^2}{s_{bj}} \right) p_b^\rho + 2 \left(\frac{s_{bj}}{s_{ab}} + \frac{q_j^2}{s_{aj}} \right) p_a^\rho \quad (4.7)$$

1143 In eq. (4.5) we have two types of terms involving the effective vertex; terms like
 1144 $V^2(q_{t/bj}, q_{t/b(j+1)})$ and terms like $V(q_{tj}, q_{t(j+1)}) \cdot V(q_{bj}, q_{b(j+1)})$. The procedure for the
 1145 V^2 terms doesn't change between top-line emission and bottom-line emission and
 1146 so only the calculation for top-line emission will be shown here.

1147 4.2.2 $V^2(q_{tj}, q_{t(j+1)})$ Terms

1148 Once we square eq. (4.7) and impose on-shell conditions to p_a and p_b we get:

$$V^2(q_{tj}, q_{tj}) = 4q_j^2 + 8q_j \cdot p_b \left(\frac{s_{aj}}{s_{ab}} - \frac{q_j^2}{s_{bj}} \right) - 8q_j \cdot p_a \left(\frac{s_{bj}}{s_{ab}} + \frac{q_j^2}{s_{aj}} \right) - 4s_{ab} \left(\frac{s_{aj}}{s_{ab}} - \frac{q_j^2}{s_{bj}} \right) \left(\frac{s_{bj}}{s_{ab}} + \frac{q_j^2}{s_{aj}} \right) \quad (4.8)$$

1149 Now since $p_j \rightarrow 0$ the terms s_{aj} and s_{bj} will also become vanishing:

$$V^2(q_{tj}, q_{tj}) = 4q_j^2 + 8q_j \cdot p_b \frac{q_j^2}{s_{bj}} - 8q_j \cdot p_a \frac{q_j^2}{s_{aj}} - 4s_{ab} \frac{q_j^4}{s_{bj}s_{aj}} \quad (4.9)$$

1150 Clearly the final term now dominates due to its $\sim \frac{1}{p_i^2}$ behaviour:

$$V^2(q_{ti}, q_{ti}) = -\frac{4s_{ab}}{s_{bi}s_{ai}} q_i^4 + \mathcal{O}\left(\frac{1}{|p_i|}\right) \quad (4.10)$$

1151 We must now explicitly calculate the invariant mass terms. Since we are in the high

¹¹⁵² energy limit we may take $p_a \sim p_1 \sim p_+ = (\frac{1}{2}p_z, 0, 0, \frac{1}{2}p_z)$ and $p_b \sim p_n \sim p_- =$
¹¹⁵³ $(\frac{1}{2}p_z, 0, 0, -\frac{1}{2}p_z)$ and we describe our soft gluon by $p_i = (E, \vec{p})$. Therefore:

$$s_{ai} = 2p_a \cdot p_i \sim 2p_+ \cdot p_i = \frac{1}{2}p_z E - \frac{1}{2}p_z^2, \quad (4.11a)$$

$$s_{bi} = 2p_b \cdot p_i \sim 2p_- \cdot p_i = \frac{1}{2}p_z E + \frac{1}{2}p_z^2, \quad (4.11b)$$

¹¹⁵⁴ and $s_{ab} = \frac{1}{2}p_z^2$. Then eq. (4.10) reads:

$$V^2(q_{ti}, q_{ti}) = -\frac{4p_z^2}{(p_z E - p_z^2)(p_z E + p_z^2)} q_i^4 + \mathcal{O}\left(\frac{1}{|p_i|}\right), \quad (4.12a)$$

$$V^2(q_{ti}, q_{ti}) = -\frac{4p_z^2}{p_z^2(E^2 - p_z^2)} q_i^4 + \mathcal{O}\left(\frac{1}{|p_i|}\right), \quad (4.12b)$$

¹¹⁵⁵ but since $E^2 - p_1^2 = 0$:

$$V^2(q_{ti}, q_{ti}) = -\frac{4}{|\vec{p}_{1\perp}|^2} q_i^4 + \mathcal{O}\left(\frac{1}{|p_i|}\right), \quad (4.13)$$

¹¹⁵⁶ Now looking back to eq. (4.5) we see that each vertex is associated with factors of
¹¹⁵⁷ $(q_{ti}^{-2} q_{t(i+1)}^{-2})$ but once again since the emission is soft this becomes (q_{ti}^{-4}) . This factor
¹¹⁵⁸ conspires to cancel with that in eq. (4.13), moreover each vertex comes with a factor
¹¹⁵⁹ of $-C_A g_s^2$ (which are contained in the \mathcal{K}_i terms in eq. (4.5)). Including these and
¹¹⁶⁰ dropping subdominant terms the final factor is:

$$\frac{4C_A g_s^2}{|\vec{p}_{\perp}|^2} \quad (4.14)$$

¹¹⁶¹ 4.2.3 $V(q_{ti}, q_{t(i+1)}) \cdot V(q_{bi}, q_{b(i+1)})$ Terms

¹¹⁶² The calculation of the interference term with a soft emission follows similarly to the
¹¹⁶³ above section. After taking $p_i \rightarrow 0$ and dotting the two vertex terms together we have:

$$\begin{aligned} V(q_{ti}, q_{ti}) \cdot V(q_{bi}, q_{bi}) &= 4q_i^t \cdot q_i^b - 4q_i^t \cdot p_a \left(\frac{s_{bi}}{s_{ab}} + \frac{t_i^b}{s_{ai}} \right) + 4q_i^t \cdot p_b \left(\frac{s_{ai}}{s_{ab}} + \frac{t_i^b}{s_{bi}} \right) \dots \\ &\quad - 4q_i^b \cdot p_a \left(\frac{s_{bi}}{s_{ab}} + \frac{t_i^t}{s_{ai}} \right) + 4q_i^b \cdot p_b \left(\frac{s_{ai}}{s_{ab}} + \frac{t_i^t}{s_{bi}} \right) \dots \end{aligned} \quad (4.15)$$

1164 having use $p_a^2 = 0$ and $p_b^2 = 0$ once again. We can drop all the terms with s_{ai} or s_{bi} in
 1165 the denominator and this time we are left with *two* dominant terms which combine to
 1166 give:

$$V(q_{ti}, q_{ti}) \cdot V(q_{bi}, q_{bi}) = -\frac{s_{ab}}{s_{ai}s_{bi}} t_i^t t_i^b + \mathcal{O}\left(\frac{1}{|p_i|}\right). \quad (4.16)$$

1167 The invariant mass terms here are identical to those we saw in the V^2 terms and the
 1168 products of $t_i^t t_i^b$ also appear in the denominator of the interference term in eq. (4.5).
 1169 After this cancelling we are left with exactly what we had before (see eq. (4.14)). Since
 1170 exactly the same factor comes from all three terms at the amplitude squared level we
 1171 may factor them out and express the amplitude squared for an n -parton final state with
 1172 one soft emission in terms of an $(n-1)$ -parton final state amplitude squared multiplied
 1173 by our factor:

$$\lim_{p_i \rightarrow 0} |\mathcal{A}_{Z/\gamma}^{2 \rightarrow n}|^2 = \left(\frac{4C_A g_s^2}{|\vec{p}_{i\perp}|^2} \right) |\mathcal{A}_{Z/\gamma}^{2 \rightarrow (n-1)}|^2 \quad (4.17)$$

1174 4.2.4 Integration of soft diverences

1175 As mentioned above the divergences only become apparent after we have attempted to
 1176 integrate over phase space. The Lorentz invariant phase space integral associated with
 1177 p_i is:

$$\int \frac{d^3 \vec{p}_i}{(2\pi)^3 2E_i} \frac{4C_A g_s^2}{|\vec{p}_{i\perp}|^2}. \quad (4.18)$$

1178 It is convenient to replace the integral over the z -component of momentum with one
 1179 over rapidity, y_2 . Rapidity and momentum are related through:

$$y = \frac{1}{2} \ln \left(\frac{E + p_z}{E - p_z} \right) \quad (4.19)$$

1180 The Jacobian of this transformation is:

$$\frac{dy}{dp_z} = \frac{1}{2(E+p_z)} \frac{\partial}{\partial p_z}(E+p_z) - \frac{1}{2(E-p_z)} \frac{\partial}{\partial p_z}(E-p_z), \quad (4.20)$$

$$= \frac{E}{E^2 - p_z^2} - \frac{p_z}{E^2 - p_z^2} \frac{\partial E}{\partial p_z}, \quad (4.21)$$

$$= \frac{E}{E^2 - p_z^2} - \frac{p_z}{E^2 - p_z^2} \frac{p_z}{E}, \quad (4.22)$$

$$= \frac{1}{E}. \quad (4.23)$$

1181 The phase space integral then reads:

$$\int \frac{d^{2+2\epsilon} \vec{p}_\perp}{(2\pi)^{2+2\epsilon}} \frac{dy}{4\pi} \frac{4C_A g_s^2}{|\vec{p}_\perp|^2} \mu^{-2\epsilon} = \frac{4C_A g_s^2 \mu^{-2\epsilon}}{(2\pi)^{2+2\epsilon} 4\pi} \Delta_{i-1,i+1} \int \frac{d^{2+2\epsilon} \vec{p}_\perp}{|\vec{p}_\perp|^2}, \quad (4.24)$$

1182 where we have analytically continued the integral to $2 + 2\epsilon$ dimensions to regulate the
1183 divergence and introduced the parameter μ to keep the coupling dimensionless in the
1184 process. Converting to polar coordinates and using the result for the volume of a unit
1185 hypersphere gives to integrated soft contribution:

$$\frac{4C_A g_s^2}{(2\pi)^{2+2\epsilon} 4\pi} \Delta_{i-1,i+1} \frac{1}{\epsilon} \frac{\pi^{1+\epsilon}}{\Gamma(\epsilon+1)} \left(\frac{\lambda^2}{\mu^2} \right)^\epsilon \quad (4.25)$$

1186 4.2.5 Virtual Emissions

1187 The virtual emission diagrams are included using the Lipatov ansatz for the gluon
1188 propagator:

$$\frac{1}{q_i^2} \longrightarrow \frac{1}{q_i^2} e^{\hat{\alpha}(q_i)(\Delta_{i,i-1})}, \quad (4.26)$$

1189 where:

$$\hat{\alpha}(q_i) = \alpha_s C_A q_i^2 \int \frac{d^{2+2\epsilon} k_\perp}{(2\pi)^{2+2\epsilon}} \frac{1}{k_\perp^2 (k_\perp - q_{i\perp})^2} \mu^{-2\epsilon}. \quad (4.27)$$

1190 Once again we choose to perform the integral using dimensional regularisation. Using
1191 the well known Feynman parameterisation formulae gives:

$$\hat{\alpha}(q_i) = \alpha_s C_A q_i^2 \int \frac{d^{2+2\epsilon} k_\perp}{(2\pi)^{2+2\epsilon}} \int_0^1 \frac{dx}{[x(k - q_i)_\perp^2 + (1-x)k_\perp^2]^2} \mu^{-2\epsilon}, \quad (4.28)$$

$$= \alpha_s C_A q_i^2 \int \frac{d^{2+2\epsilon} \hat{k}_\perp}{(2\pi)^{2+2\epsilon}} \int_0^1 \frac{dx}{[\hat{k}_\perp^2 + q_{i\perp}^2(1-x)]^2} \mu^{-2\epsilon}, \quad (4.29)$$

1192 where we have performed a change of variables to $\hat{k}_\perp = k_\perp - x q_{i\perp}$ with unit Jacobian.
 1193 Changing the order of integration we can perform the \hat{k}_\perp integral using the following
 1194 result:

$$\int \frac{d^d k}{(2\pi)^d} \frac{1}{(k^2 - C)^\alpha} = \frac{1}{(4\pi)^{\frac{d}{2}}} \frac{\Gamma(\alpha - \frac{d}{2})}{\Gamma(\alpha)} \frac{(-1)^\alpha}{C^{\alpha - \frac{d}{2}}}, \quad (4.30)$$

1195 to give:

$$\hat{\alpha}(q_i) = \alpha_s C_A q_i^2 \frac{\Gamma(1-\epsilon)}{(4\pi)^{1+\epsilon}} (-q_{i\perp}^2)^{\epsilon-1} \int_0^1 dx (1-x)^{\epsilon-1}, \quad (4.31)$$

$$= -\frac{2g_s^2 C_A}{(4\pi)^{2+\epsilon}} \frac{\Gamma(1-\epsilon)}{\epsilon} \left(\frac{q_{i\perp}^2}{\mu^2} \right)^\epsilon, \quad (4.32)$$

1196 having completed the x integral and used $\alpha_s = \frac{g_s^2}{4\pi}$.

1197 4.2.6 Cancellation of Infrared Contributions

1198 We now show how the infrared contributions from soft real emissions and virtual
 1199 emissions cancel leaving our integrated matrix element finite. The subtlety here is
 1200 that we must sum two diagrams with different final states to see the cancellation.
 1201 This is because they are experimentally indistinguishable; the $2 \rightarrow (n-1)$ virtual
 1202 diagram has $(n-1)$ resolvable partons in the final state (but is a higher order diagram
 1203 perturbatively speaking). Because one of the emission in the real $2 \rightarrow n$ diagram is
 1204 soft it is experimentally undetectable so we detect the same final state as the virtual
 1205 diagram. The matrix element squared for the real soft diagram will look like:

$$|\mathcal{A}_{Z/\gamma}^{2 \rightarrow n}|^2 = \left(\frac{4g_s^2 C_a}{|p_{i\perp}|^2} \right) \left[\left| \mathcal{K}_a j_1^{Z/\gamma} \cdot j_2 \right|^2 \frac{\prod_{i \neq j}^{n-2} V^2(q_{ti}, q_{t(i+1)})}{\prod_{i \neq j}^{n-1} q_{ti}^2} + \dots \right] \quad (4.33)$$

$$\left| \mathcal{K}_b j_2^{Z/\gamma} \cdot j_1 \right|^2 \frac{\prod_{i \neq j}^{n-2} V^2(q_{bi}, q_{b(i+1)})}{\prod_{i \neq j}^{n-1} q_{bi}^2} + \dots \quad (4.34)$$

$$2\Re\{\mathcal{K}_a \overline{\mathcal{K}_b} \times (j_1^{Z/\gamma} \cdot j_2)(\overline{j_2^{Z/\gamma} \cdot j_1})\} \frac{\prod_{i \neq j}^{n-2} V(q_{ti}, q_{t(i+1)}) \cdot V(q_{bi}, q_{b(i+1)}))}{\prod_{i \neq j}^{n-1} q_{ti} q_{bi}} \Big], \quad (4.35)$$

where we have taken the i^{th} gluon to be soft and the result of the Lorentz invariant phase space integration over the p_i momentum is shown in eq. (4.25).

After inserting the Lipatov ansatz into the $2 \rightarrow (n-1)$ matrix element squared we have:

$$|\mathcal{A}_{Z/\gamma}^{2 \rightarrow (n-1)}|^2 = \left| \mathcal{K}_a j_1^{Z/\gamma} \cdot j_2 \right|^2 \frac{\prod_i^{n-3} V^2(q_{ti}, q_{t(i+1)})}{\prod_i^{n-2} q_{ti}^2} e^{2\hat{\alpha}(q_{ti})\Delta_{i-1,i+1}} + \dots \quad (4.36)$$

$$\left| \mathcal{K}_b j_2^{Z/\gamma} \cdot j_1 \right|^2 \frac{\prod_i^{n-3} V^2(q_{bi}, q_{b(i+1)})}{\prod_i^{n-2} q_{bi}^2} e^{2\hat{\alpha}(q_{bi})\Delta_{i-1,i+1}} + \dots \quad (4.37)$$

$$2\Re\{\mathcal{K}_a \overline{\mathcal{K}_b} \times (j_1^{Z/\gamma} \cdot j_2)(\overline{j_2^{Z/\gamma} \cdot j_1})\} \frac{\prod_i^{n-3} V(q_{ti}, q_{t(i+1)}) \cdot V(q_{bi}, q_{b(i+1)}))}{\prod_i^{n-2} q_{ti} q_{bi}} e^{(\hat{\alpha}(q_{bi}) + \hat{\alpha}(q_{ti}))\Delta_{i-1,i+1}}, \quad (4.38)$$

We can now go through term-by-term to show the divergences cancel and find the finite contribution to the matrix element squared. Similarly to when we calculated the soft terms the pure top and bottom emissions follow identically so here we will only state the procedure for the top emission. The interference term is slightly different.

For the top line emission we have the following terms:

$$\frac{4C_A g_s^2}{(2\pi)^{2+2\epsilon} 4\pi} \Delta_{i-1,i+1} \frac{1}{\epsilon} \frac{\pi^{1+\epsilon}}{\Gamma(\epsilon+1)} \left(\frac{\lambda^2}{\mu^2} \right)^\epsilon + e^{2\hat{\alpha}_s(q_{ti})\Delta_{i-1,i+1}}. \quad (4.39)$$

We now extract the relevant term (in terms of the strong coupling order) from the exponential and substitute the expression for $\hat{\alpha}_s$:

$$= \frac{4C_A g_s^2}{(2\pi)^{2+2\epsilon} 4\pi} \Delta_{i-1,i+1} \frac{1}{\epsilon} \frac{\pi^{1+\epsilon}}{\Gamma(\epsilon+1)} \left(\frac{\lambda^2}{\mu^2} \right)^\epsilon - - \frac{2g_s^2 C_A}{(4\pi)^{2+\epsilon}} \frac{\Gamma(1-\epsilon)}{\epsilon} \left(\frac{q_{ti\perp}^2}{\mu^2} \right)^\epsilon, \quad (4.40)$$

$$= \frac{g_s^2 C_A}{4^{1+\epsilon} \pi^{2+\epsilon}} \Delta_{i-1,i+1} \left(\frac{1}{\epsilon \Gamma(1+\epsilon)} \left(\frac{\lambda^2}{\mu^2} \right)^\epsilon - \frac{\Gamma(1-\epsilon)}{\epsilon} \left(\frac{q_{ti\perp}^2}{\mu^2} \right)^\epsilon \right). \quad (4.41)$$

¹²¹⁷ Expanding the terms involving ϵ yeilds:

$$\frac{1}{\Gamma(1+\epsilon)} = 1 + \gamma_E \epsilon + \mathcal{O}(\epsilon^2), \quad (4.42a)$$

$$\Gamma(1-\epsilon) = 1 + \gamma_E \epsilon + \mathcal{O}(\epsilon^2), \quad (4.42b)$$

$$\left(\frac{x}{y} \right)^\epsilon = 1 + \epsilon \ln \left(\frac{x}{y} \right) + \mathcal{O}(\epsilon^2). \quad (4.42c)$$

¹²¹⁸ And so the finite terms are:

$$= \frac{g_s^2 C_A \Delta_{i-1,i+1}}{4^{1+\epsilon} \pi^{2+\epsilon}} \left((1 + \gamma_E \epsilon + \mathcal{O}(\epsilon^2)) \left(\frac{1}{\epsilon} + \ln \left(\frac{\lambda^2}{\mu^2} \right) + \mathcal{O}(\epsilon) \right) - (1 + \gamma_E \epsilon + \mathcal{O}(\epsilon^2)) \left(\frac{1}{\epsilon} + \ln \left(\frac{q_{ti\perp}^2}{\mu^2} \right) + \mathcal{O}(\epsilon) \right) \right) \quad (4.43a)$$

$$= \frac{g_s^2 C_A \Delta_{i-1,i+1}}{4\pi^2} \ln \left(\frac{\lambda^2}{q_{ti\perp}^2} \right) \quad (4.43b)$$

$$= \frac{\alpha_s C_A \Delta_{i-1,i+1}}{\pi} \ln \left(\frac{\lambda^2}{q_{ti\perp}^2} \right) \quad (4.43c)$$

¹²¹⁹ Likewise for the emission purely from the backward quark line we have:

$$= \frac{\alpha_s C_A \Delta_{i-1,i+1}}{\pi} \ln \left(\frac{\lambda^2}{q_{bi\perp}^2} \right) \quad (4.44)$$

¹²²⁰ For the interference we expand the exponential with both forward emission q momenta

¹²²¹ and backward emission q momenta to get:

$$= \frac{g_s^2 C_A \Delta_{i-1,i+1}}{4^{1+\epsilon} \pi^{2+\epsilon}} \left(\left(\frac{1}{\epsilon} + \gamma_E + \ln \left(\frac{\lambda^2}{\mu^2} \right) + \mathcal{O}(\epsilon) \right) - \frac{1}{2} \left[\frac{2}{\epsilon} + 2\gamma_E + \ln \left(\frac{q_{ti\perp}^2}{\mu^2} \right) - \ln \left(\frac{q_{bi\perp}^2}{\mu^2} \right) + \mathcal{O}(\epsilon) \right] \right) \quad (4.45a)$$

$$= \frac{\alpha_s C_A \Delta_{i-1,i+1}}{\pi} \ln \left(\frac{\lambda^2}{\sqrt{q_{ti\perp}^2 q_{bi\perp}^2}} \right) \quad (4.45b)$$

1222 This is a very similar form to that found in [?] and [?].

1223 **4.2.7 Example: $2 \rightarrow 4$ Scattering**

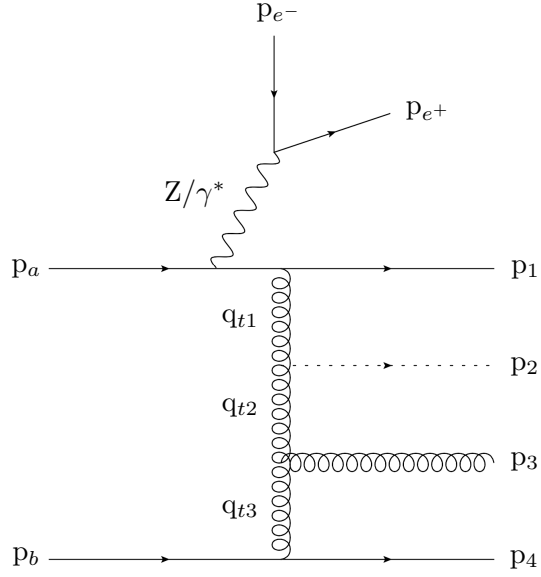
1224 As an example we show the cancellation explicitly for the case of $2 \rightarrow 4$ when the p_2
1225 momentum has gone soft. A contributing soft diagram is shown in fig. 4.2a and one
1226 example of a contributing virtual diagram of the same order is shown in fig. 4.2b. When
1227 p_2 goes soft we have the following form for the $2 \rightarrow 4$ integrated amplitude squared
1228 (N.B.: The integration is only schematic and doesn't represent the full Lorentz invariant
1229 phase space):

$$\int |\mathcal{A}_{soft}^{2 \rightarrow 4}|^2 = \frac{4C_A g_s^2 \Delta_{1,3}}{(2\pi)^{2+2\epsilon} 4\pi \epsilon \Gamma(\epsilon+1)} \left(\frac{\lambda^2}{\mu^2} \right)^\epsilon \left[|\mathcal{K}_a j_1^Z \cdot j_2|^2 \frac{V^2(q_{t1}, q_{t3})}{q_{t1}^2 q_{t3}^2} + |\mathcal{K}_b j_1 \cdot j_2^Z|^2 \frac{V^2(q_{b1}, q_{b3})}{q_{b1}^2 q_{b3}^2} + \dots \right. \\ \left. 2\Re \left\{ \mathcal{K}_a \overline{\mathcal{K}_b} (j_1^Z \cdot j_2) \overline{(j_1 \cdot j_2^Z)} \right\} \frac{V(q_{t1}, q_{t3}) \cdot V(q_{b1}, q_{b3})}{q_{t1} q_{t3} q_{b1} q_{b3}} \right], \quad (4.46)$$

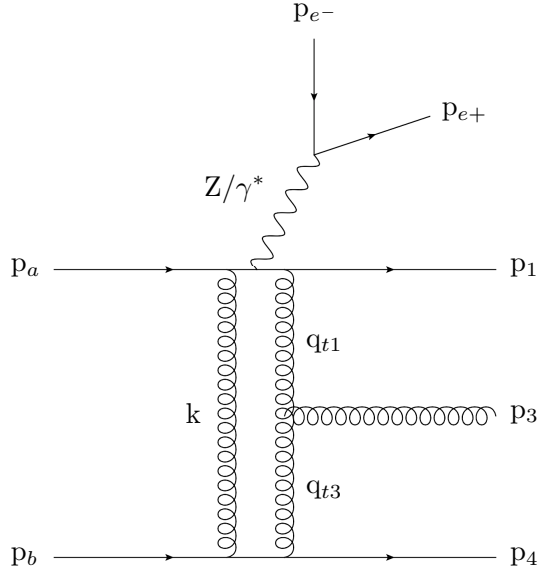
1230 and the virtual contributions for the $2 \rightarrow 3$ amplitude is:

$$\int |\mathcal{A}_{virtual}^{2 \rightarrow 3}|^2 = |\mathcal{K}_b j_1 \cdot j_2^Z|^2 \frac{V^2(q_{t1}, q_{t3})}{q_{t1}^2} e^{2\hat{\alpha}(q_{t1})\Delta_{1,3}} + |\mathcal{K}_t j_1^Z \cdot j_2|^2 \frac{V^2(q_{b1}, q_{b3})}{q_{b1}^2} e^{2\hat{\alpha}(q_{b1})\Delta_{1,3}} + \dots \\ 2\Re \left\{ \mathcal{K}_a \overline{\mathcal{K}_b} (j_1^Z \cdot j_2) \overline{(j_1 \cdot j_2^Z)} \right\} \frac{V(q_{t1}, q_{t3}) \cdot V(q_{b1}, q_{b3})}{q_{t1} q_{t3} q_{b1} q_{b3}} e^{(\hat{\alpha}(q_{t1}) + \hat{\alpha}(q_{b1}))\Delta_{1,3}}. \quad (4.47)$$

1231 Once we expand the exponential to the correct order in g_s^2 , the sum of these matrix
1232 elements squared over the region of phase space when p_2 is soft is:



(a) Soft Emission



(b) Virtual Emission

Figure 4.2: Examples of diagrams contributing to $2 \rightarrow 4$ scattering. In fig. 4.2a the p_2 has been drawn with a dashed line to denote it is not resolvable. In fig. 4.2b the final state momenta have been labelled in a seemingly strange way - this was done to make clear the cancellation when working through the algebra.

$$\begin{aligned}
 \int (|\mathcal{A}_{soft}^{2 \rightarrow 4}|^2 + |\mathcal{A}_{virtual}^{2 \rightarrow 3}|^2) = & |\mathcal{K}_a j_1^Z \cdot j_2|^2 \frac{V^2(q_{t1}, q_{t3})}{q_{t1}^2} \left(\frac{4C_A g_s^2 \Delta_{1,3}}{(2\pi)^{2+2\epsilon} 4\pi} \frac{\pi^{\epsilon+1}}{\epsilon \Gamma(\epsilon+1)} - 2\hat{\alpha}(q_{t1}) \Delta_{1,3} \right) + \dots \\
 & |\mathcal{K}_b j_1 \cdot j_2^Z|^2 \frac{V^2(q_{b1}, q_{b3})}{q_{b1}^2} \left(\frac{4C_A g_s^2 \Delta_{1,3}}{(2\pi)^{2+2\epsilon} 4\pi} \frac{\pi^{\epsilon+1}}{\epsilon \Gamma(\epsilon+1)} - 2\hat{\alpha}(q_{b1}) \Delta_{1,3}^{69} \right) + \dots \\
 & 2\Re \left\{ \mathcal{K}_a \overline{\mathcal{K}_b} (j_1^Z \cdot j_2) \overline{(j_1 \cdot j_2^Z)} \right\} \frac{V(q_{t1}, q_{t3}) \cdot V(q_{b1}, q_{b3})}{q_{t1} q_{t3} q_{b1} q_{b3}} \left(\frac{4C_A g_s^2 \Delta_{1,3}}{(2\pi)^{2+2\epsilon} 4\pi} \frac{\pi^{\epsilon+1}}{\epsilon \Gamma(\epsilon+1)} - (\hat{\alpha}(q_{t1}) + \hat{\alpha}(q_{b1})) \Delta_{1,3} \right) + \dots
 \end{aligned} \tag{4.48}$$

1233 These bracketed terms are exactly the cancellations calculated in section 4 above.

1234 Therefore:

$$\begin{aligned} \int (|\mathcal{A}_{soft}^{2 \rightarrow 4}|^2 + |\mathcal{A}_{virtual}^{2 \rightarrow 3}|^2) = & \frac{\alpha_s C_A \Delta_{1,3}}{\pi} \left(|\mathcal{K}_a j_1^Z \cdot j_2|^2 \frac{V^2(q_{t1}, q_{t3})}{q_{t1}^2} \ln \left(\frac{\lambda^2}{|q_{1t\perp}|^2} \right) + \dots \right. \\ & |\mathcal{K}_b j_1 \cdot j_2^Z|^2 \frac{V^2(q_{b1}, q_{b3})}{q_{b1}^2} \ln \left(\frac{\lambda^2}{|q_{1b\perp}|^2} \right) + \dots \\ & \left. 2\Re \left\{ \mathcal{K}_a \overline{\mathcal{K}_b} (j_1^Z \cdot j_2) \overline{(j_1 \cdot j_2^Z)} \right\} \frac{V(q_{t1}, q_{t3}) \cdot V(q_{b1}, q_{b3})}{q_{t1} q_{t3} q_{b1} q_{b3}} \ln \left(\frac{\lambda^2}{\sqrt{|q_{1t\perp}|^2 |q_{1b\perp}|^2}} \right) \right) + \mathcal{O}(\alpha_s^2), \end{aligned} \quad (4.49)$$

1235 Which is manifestly finite.

1236 4.3 Subtractions and the λ_{cut} scale

1237 The table below shows the value of the total cross section for varying values of the
1238 parameter λ_{cut} defined in section ???. It is clear that the cross section does not display
1239 a large dependence on the value of λ_{cut} . Figure 4.3 shows the effect of the same variation
1240 in λ_{cut} on the differential distribution in the rapidity gap between the two leading jets
1241 in p_\perp . Our default chosen value is 0.2.

λ_{cut} (GeV)	$\sigma(2j)$ (pb)	$\sigma(3j)$ (pb)	$\sigma(4j)$ (pb)
0.2	5.16 ± 0.03	0.90 ± 0.02	0.20 ± 0.02
0.5	5.17 ± 0.02	0.92 ± 0.01	0.22 ± 0.03
1.0	5.20 ± 0.02	0.91 ± 0.02	0.20 ± 0.01
1.0	5.26 ± 0.02	0.91 ± 0.02	0.21 ± 0.02

Table 4.1: The total cross-sections for the 2, 3 and 4 jet exclusive rates with associated statistical errors shown for different values of the regularisation parameter λ_{cut} . The scale choice was the half the sum over all traverse scales in the event, $H_T/2$.

1242 4.4 $Z/\gamma^* + \text{Jets}$ at the ATLAS Experiment

1243 • Re-word descriptions of plots

1244 We now compare the results of the formalism described in the previous sections to data.

1245 We begin with a recent ATLAS analysis of Z -plus-jets events from 7 TeV collisions [3].

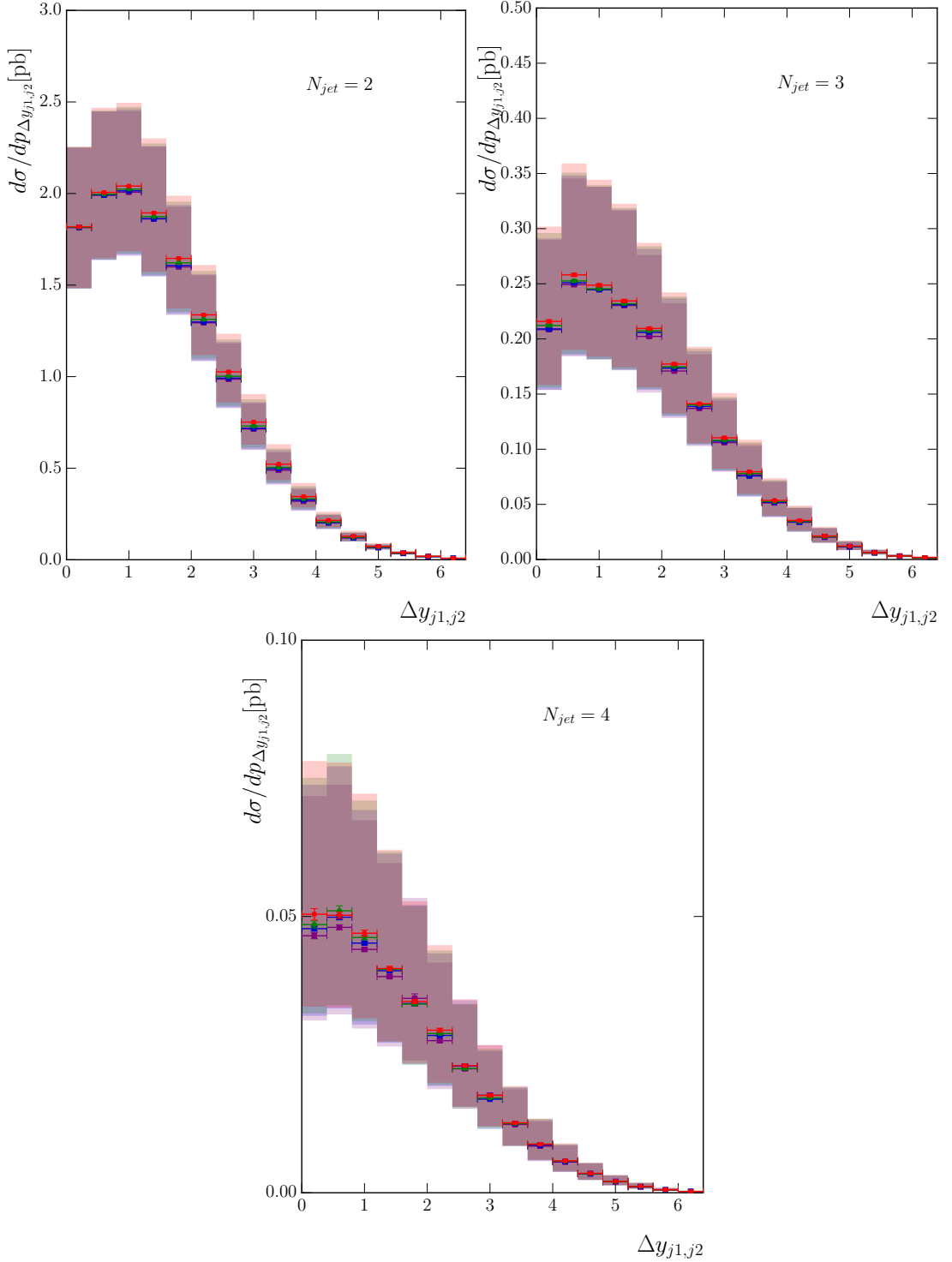


Figure 4.3: The effect of varying λ_{cut} on the differential distribution in the rapidity gap between the two leading jets in p_\perp with the $N_{jet} = 2, 3, 4$ exclusive selections shown from left to right. $\lambda_{cut} = 0.2$ (red), 0.5 (blue), 1.0 (green), 2.0 (purple).

1246 We summarise the cuts in the following table:

Lepton Cuts	$p_{T\ell} > 20 \text{ GeV}, \eta_\ell < 2.5$ $\Delta R^{\ell^+\ell^-} > 0.2, 66 \text{ GeV} \leq m^{\ell^+\ell^-} \leq 116 \text{ GeV}$
Jet Cuts ($\text{anti-}k_T$, 0.4)	$p_{Tj} > 30 \text{ GeV}, y_j < 4.4$ $\Delta R^{j\ell} > 0.5$

Table 4.2: Cuts applied to theory simulations in the ATLAS Z -plus-jets analysis results shown in Figs. 4.4–4.7.

1247 Any jet which failed the final isolation cut was removed from the event, but the event
1248 itself is kept provided there are a sufficient number of other jets present. Throughout
1249 the central value of the HEJ predictions has been calculated with factorisation and
1250 renormalisation scales set to $\mu_F = \mu_R = H_T/2$, and the theoretical uncertainty band
1251 has been determined by varying these independently by up to a factor of 2 in each
1252 direction (removing the corners where the relative ratio is greater than two). Also
1253 shown in the plots taken from the ATLAS paper are theory predictions from Alpgen [56],
1254 Sherpa [42, 45], MC@NLO [39] and BlackHat+Sherpa [19, 47]. We will also comment
1255 on the recent theory description of Ref. [36].

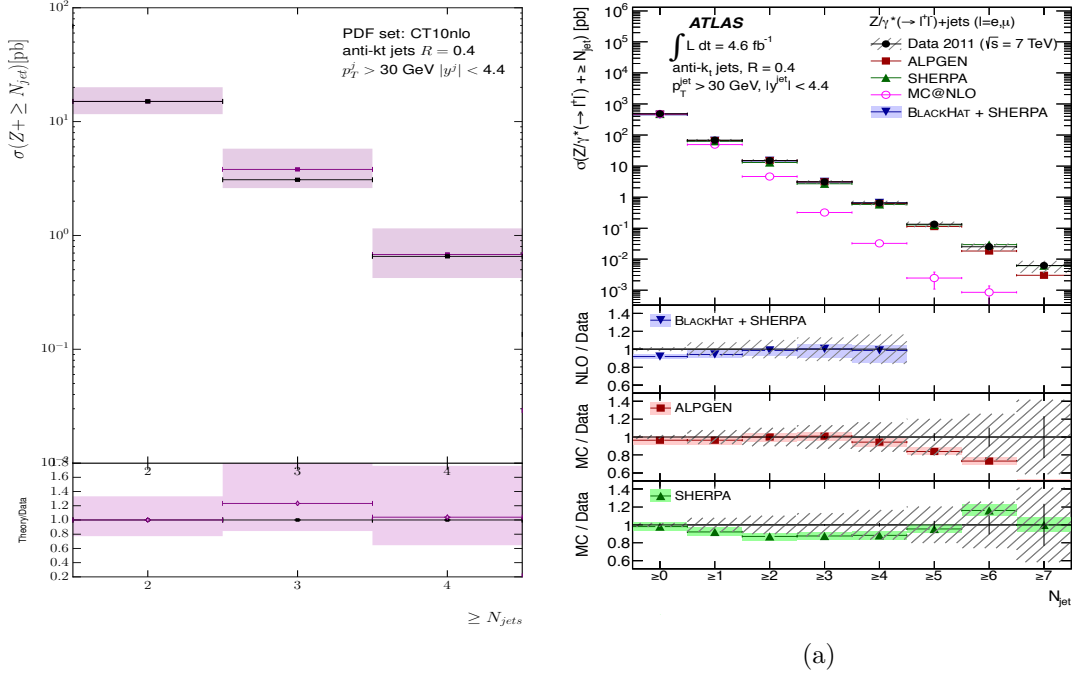
1256 In Fig. 4.4, we begin this set of comparisons with predictions and measurements of the
1257 inclusive jet rates. HEJ and most of the other theory descriptions give a reasonable
1258 description of these rates. The MC@NLO prediction drops below the data because
1259 it only contains the hard-scattering matrix element for Z/γ^* production and relies
1260 on a parton shower for additional emissions. The HEJ predictions have a larger
1261 uncertainty band which largely arises from the use of leading-order results in the
1262 matching procedures.

1263 The first differential distribution we consider here is the distribution of the invariant
1264 mass between the two hardest jets, Fig. 4.5. The region of large invariant mass is
1265 particularly important because this is a critical region for studies of vector boson fusion
1266 (VBF) processes in Higgs-plus-dijets. Radiation patterns are largely universal between
1267 these processes, so one can test the quality of theoretical descriptions in Z/γ^* -plus-
1268 dijets and use these to inform the VBF analyses. It is also a distribution which will be
1269 studied to try to detect subtle signs of new physics. In this study, HEJ and the other
1270 theory descriptions all give a good description of this variable out to 1 TeV, with HEJ
1271 being closest throughout the range. The merged sample of Ref. [36] (Fig. 9 in that
1272 paper) combined with the Pythia8 parton shower performs reasonably well throughout
1273 the range with a few deviations of more than 20%, while that combined with Herwig++
1274 deviates badly. In a recent ATLAS analysis of W -plus-dijet events [6], the equivalent
1275 distribution was extended out to 2 TeV and almost all of the theoretical predictions

1276 deviated significantly while the HEJ prediction remained flat. This is one region where
1277 the high-energy logarithms which are only included in HEJ are expected to become
1278 large.

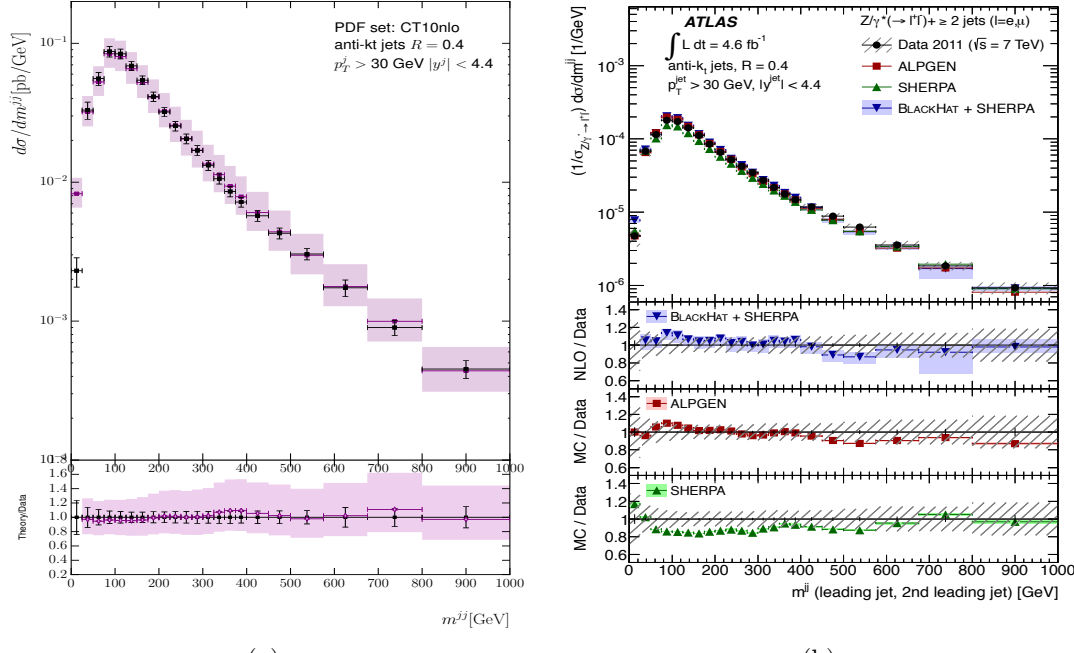
1279 In Fig. 4.6, we show the comparison of various theoretical predictions to the distribution
1280 of the absolute rapidity difference between the two leading jets. It is clear in the left
1281 plot that HEJ gives an excellent description of this distribution. This is to some extent
1282 expected as high-energy logarithms are associated with rapidity separations. However,
1283 this variable is only the rapidity separation between the two hardest jets which is often
1284 not representative of the event as harder jets tend to be more central. Nonetheless, the
1285 HEJ description performs well in this restricted scenario. The next-to-leading order
1286 (NLO) calculation of Blackhat+Sherpa also describes the distribution quite well while
1287 the other merged, fixed-order samples deviate from the data at larger values. The
1288 merged samples of Ref. [36] (Fig. 8 in that paper) describe this distribution well for
1289 small values of this variable up to about 3 units when combined with Herwig++ and
1290 for most of the range when combined with the Pythia8 parton shower, only deviating
1291 above 5 units.

1292 The final distribution in this section is that of the ratio of the transverse momentum of
1293 the second hardest jet to the hardest jet. The perturbative description of HEJ does not
1294 contain any systematic evolution of transverse momentum and this can be seen where
1295 its prediction undershoots the data at low values of p_{T2}/p_{T1} . However, for values of
1296 $p_{T2} \gtrsim 0.5p_{T1}$, the ratio of the HEJ prediction to data is extremely close to 1. The
1297 fixed-order based predictions shown in Fig. 4.4 are all fairly flat above about 0.2, but
1298 the ratio of the data differs by about 10%.

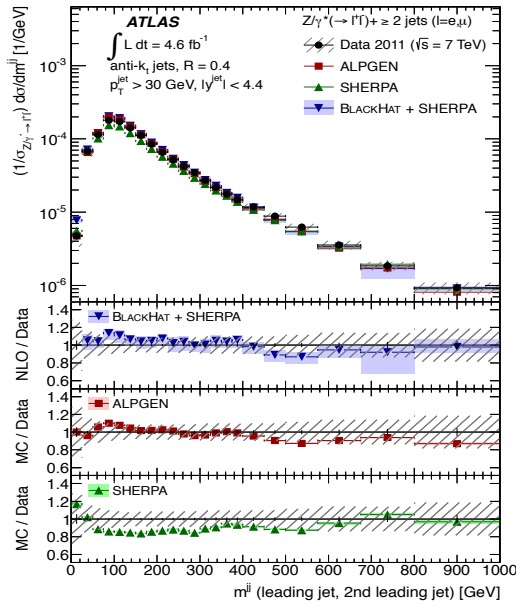


(a)

Figure 4.4: These plots show the inclusive jet rates from (a) HEJ and (b) other theory descriptions and data [3]. HEJ events all contain at least two jets and do not contain matching for 5 jets and above, so these bins are not shown.



(a)



(b)

Figure 4.5: These plots show the invariant mass between the leading and second-leading jet in p_T . As in Fig. 4.4, predictions are shown from (a) HEJ and (b) other theory descriptions and data [3]. These studies will inform Higgs plus dijets analyses, where cuts are usually applied to select events with large m_{12} .

1299 4.4.1 CMS - $Z + \text{Jets}$ Measurements

1300 We now compare to data from a CMS analysis of events with a Z/γ^* boson
 1301 produced in association with jets [51]. We show, for comparison, the plots from that
 1302 analysis which contain theoretical predictions from Sherpa [42, 45], Powheg [10] and
 1303 MadGraph [12]. The cuts used for this analysis are summarised in tab. 4.3.

Lepton Cuts	$p_{T\ell} > 20 \text{ GeV}, \eta_\ell < 2.4$ $71 \text{ GeV} \leq m^{\ell^+\ell^-} \leq 111 \text{ GeV}$
Jet Cuts (anti- k_T , 0.5)	$p_{Tj} > 30 \text{ GeV}, \eta_j < 2.4$ $\Delta R^{j\ell} > 0.5$

Table 4.3: Cuts applied to theory simulations in the CMS Z -plus-jets analysis results shown in Figs. 4.8–4.10

1304 As in the previous section, any jet which failed the final isolation cut was removed from
 1305 the event, but the event itself is kept provided there are a sufficient number of other jets
 1306 present. The main difference to these cuts and those of ATLAS in the previous section
 1307 is that the jets are required to be more central; $|\eta| < 2.4$ as opposed to $|y| < 4.4$. This
 1308 allows less room for evolution in rapidity; however, HEJ predictions are still relevant
 1309 in this scenario. Once again, the central values are given by $\mu_F = \mu_R = H_T/2$ with
 1310 theoretical uncertainty bands determined by varying these independently by factors of
 1311 two around this value. HEJ events always contain a minimum of two jets and therefore
 1312 here we only compare to the distributions for an event sample with at least two jets or
 1313 above.

1314 We begin in Fig. 4.8 by showing the inclusive jet rates for these cuts. The HEJ
 1315 predictions give a good description, especially for the 2- and 3-jet inclusive rates in this
 1316 narrower phase space. The uncertainty bands are larger for HEJ than for the Sherpa
 1317 and Powheg predictions due to our LO matching prescription (those for Madgraph are
 1318 not shown).

1319 In Figs. 4.9–4.10, we show the transverse momentum distributions for the second
 1320 and third jet respectively (the leading jet distribution was not given for inclusive dijet
 1321 events). Beginning with the second jet in Fig. 4.9, we see that the HEJ predictions
 1322 overshoot the data at large transverse momentum. In this region, the non-FKL matched
 1323 components of the HEJ description become more important and these are not controlled
 1324 by the high-energy resummation. The HEJ predictions are broadly similar to Powheg’s
 1325 Z -plus-one-jet NLO calculation matched with the Pythia parton shower. In contrast,
 1326 Sherpa’s prediction significantly undershoots the data at large transverse momentum.
 1327 Here the Madgraph prediction gives the best description of the data.

Fig. 4.10 shows the transverse momentum distribution of the third jet in this data sample. Here, the ratio of the HEJ prediction to data shows a linear increase with transverse momentum (until the last bin where all the theory predictions show the same dip). Both the Sherpa and Powheg predictions show similar deviations for this variable while the Madgraph prediction again performs very well.

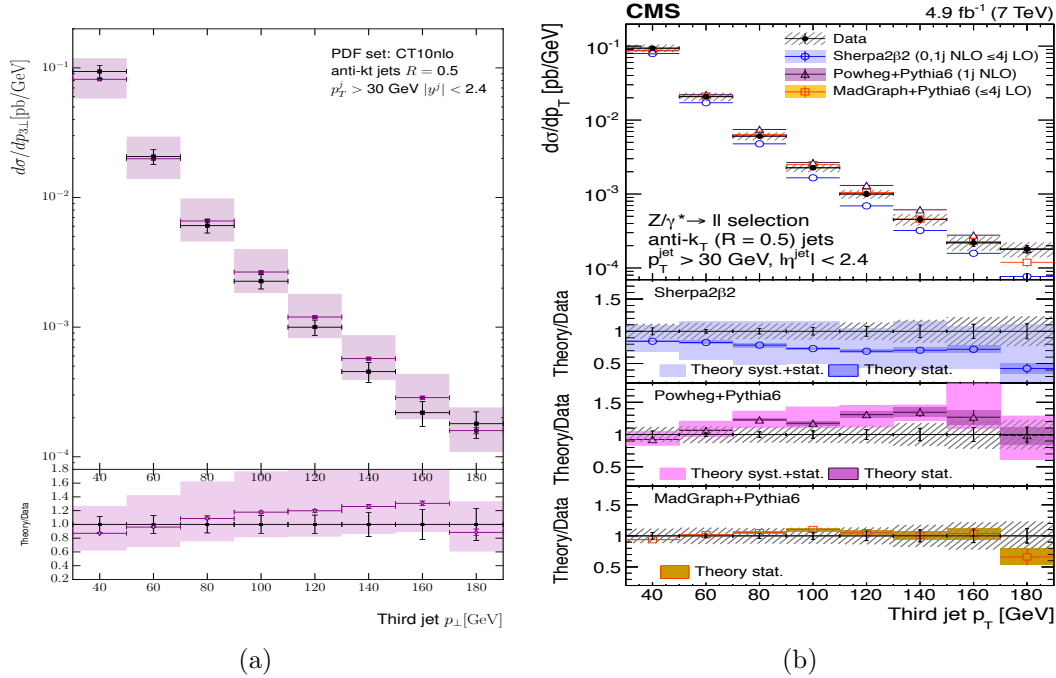


Figure 4.10: The transverse momentum distribution of the third hardest jet in inclusive dijet events in [51], compared to (a) the predictions from HEJ and (b) the predictions from other theory descriptions.

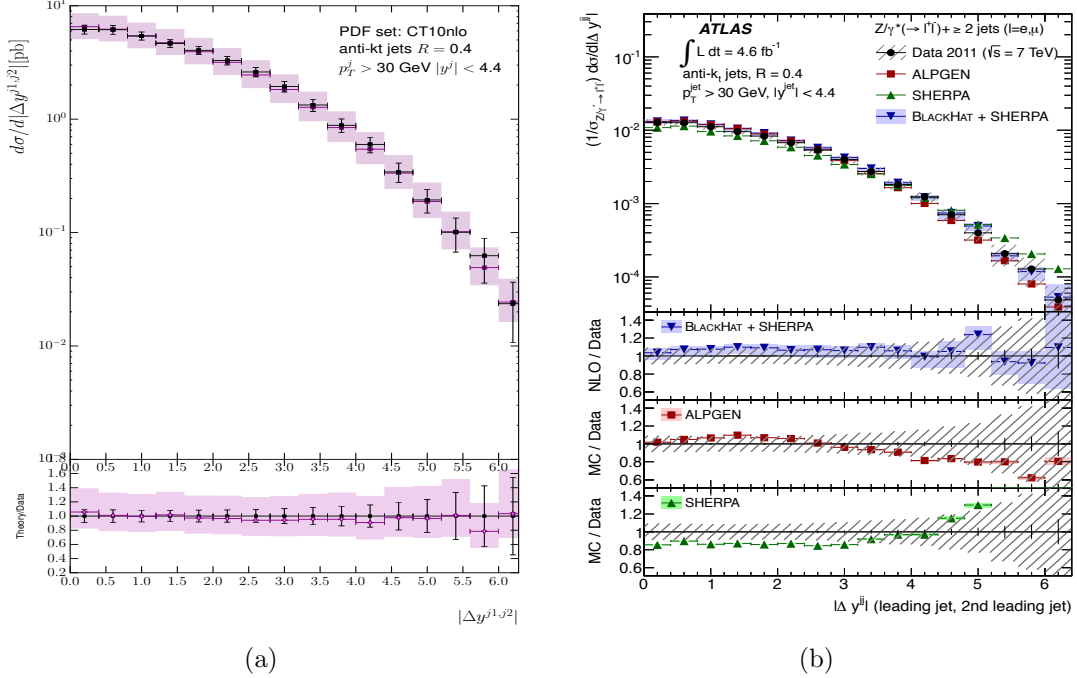


Figure 4.6: The comparison of (a) HEJ and (b) other theoretical descriptions and data [3] to the distribution of the absolute rapidity different between the two leading jets. HEJ and Blackhat+Sherpa give the best description.

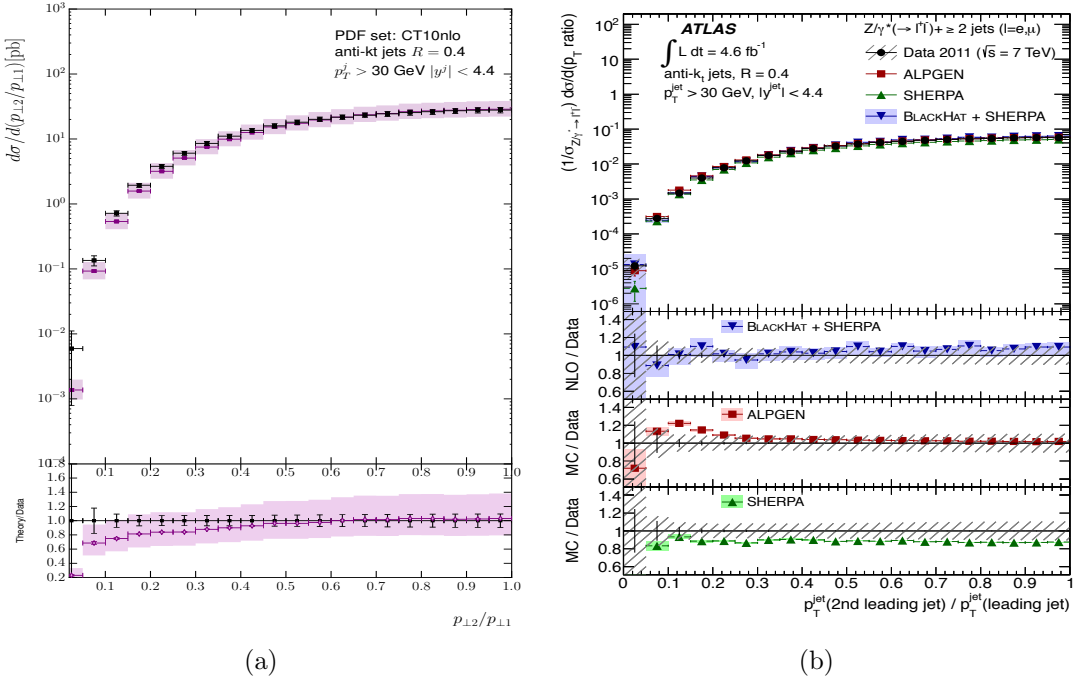


Figure 4.7: These plots show the differential cross section in the ratio of the leading and second leading jet in p_T from (a) HEJ and (b) other theory descriptions and data [3].

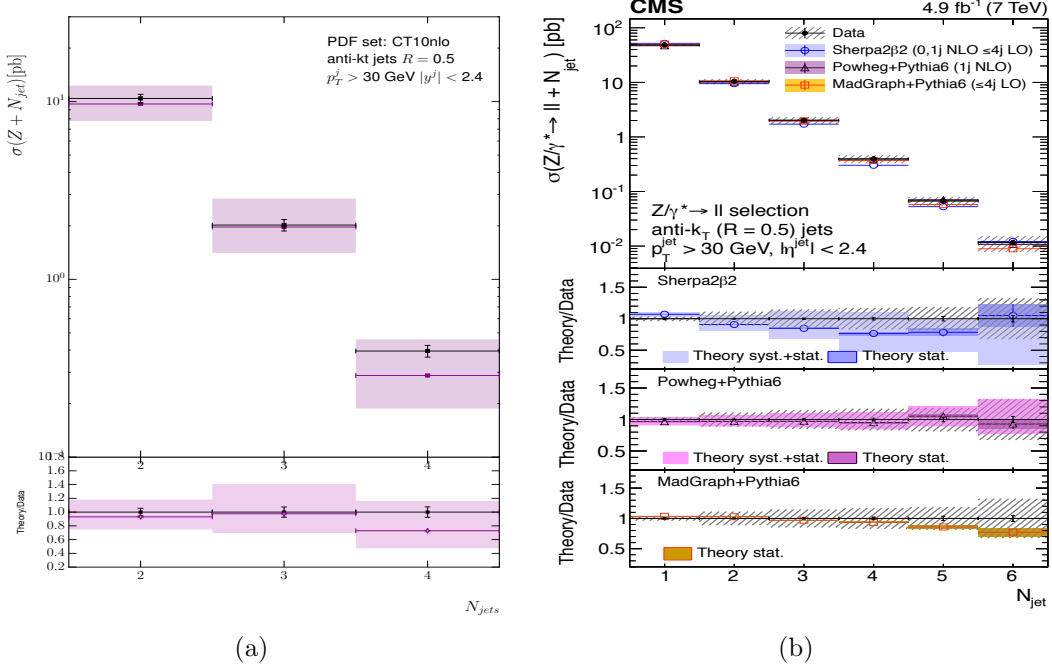


Figure 4.8: The inclusive jet rates as given by (a) the HEJ description and (b) by other theoretical descriptions, both plots compared to the CMS data in [51].

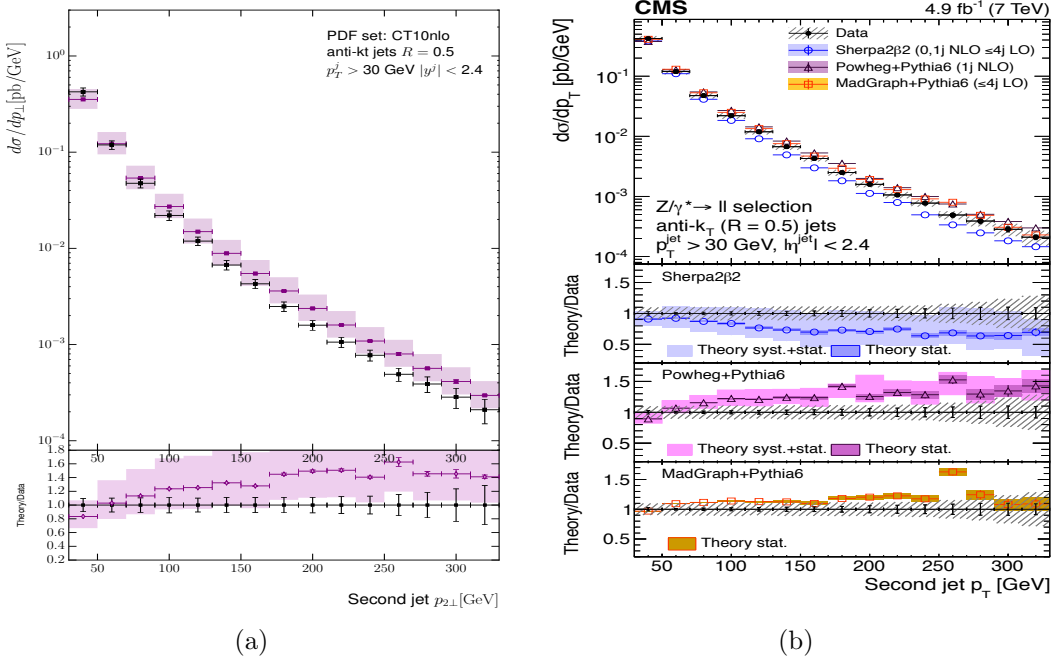


Figure 4.9: The transverse momentum distribution of the second hardest jet in inclusive dijet events in [51], compared to (a) the predictions from HEJ and (b) the predictions from other theory descriptions.

¹³³³ **Chapter 5**

¹³³⁴ **High Multiplicity Jets at ATLAS**

¹³³⁵ Show the ATLAS pure jets analysis and talk a bit about the issues with running the
¹³³⁶ damn thing. Talk about the conclusions about BFKL-like dynamics

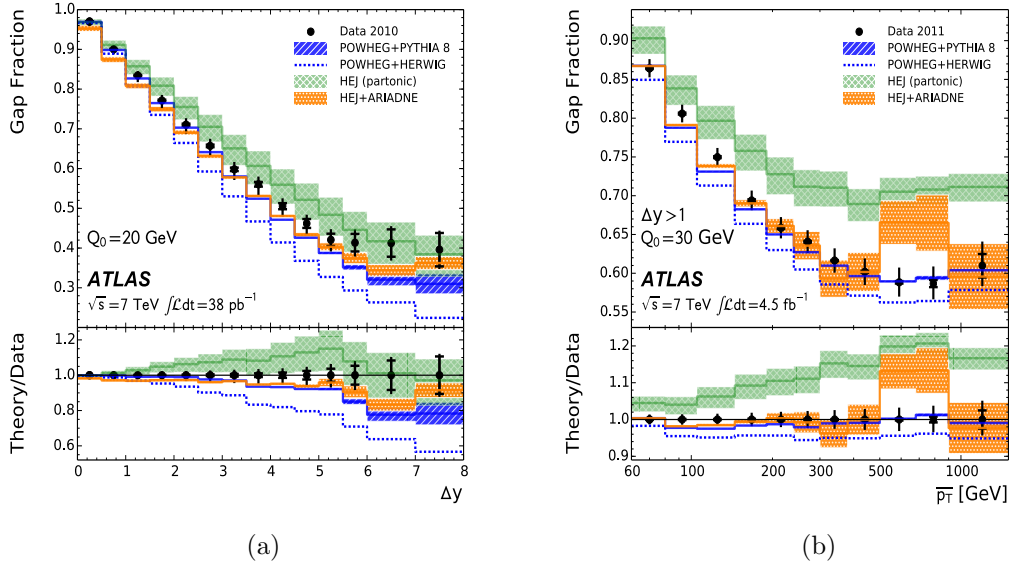


Figure 5.1

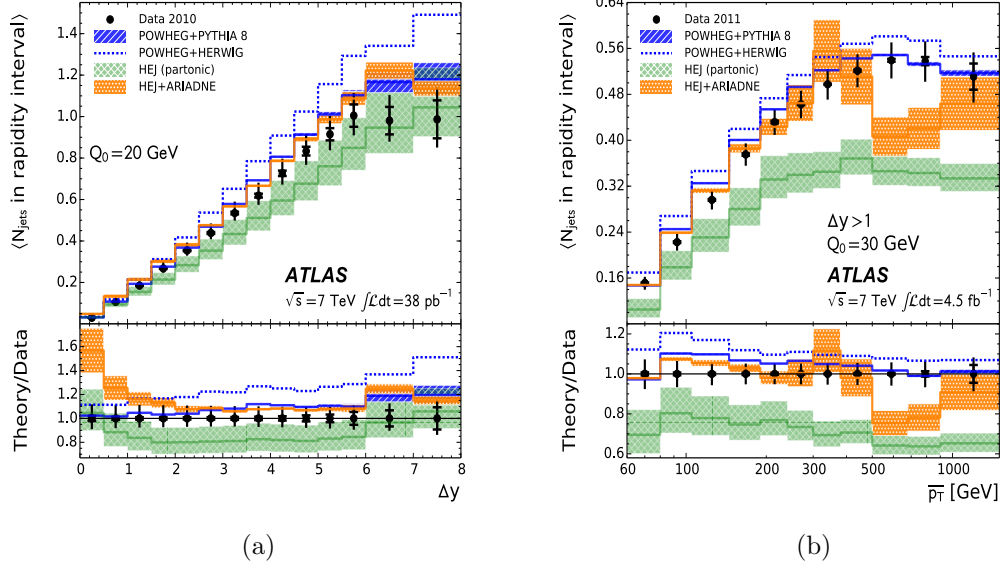


Figure 5.2

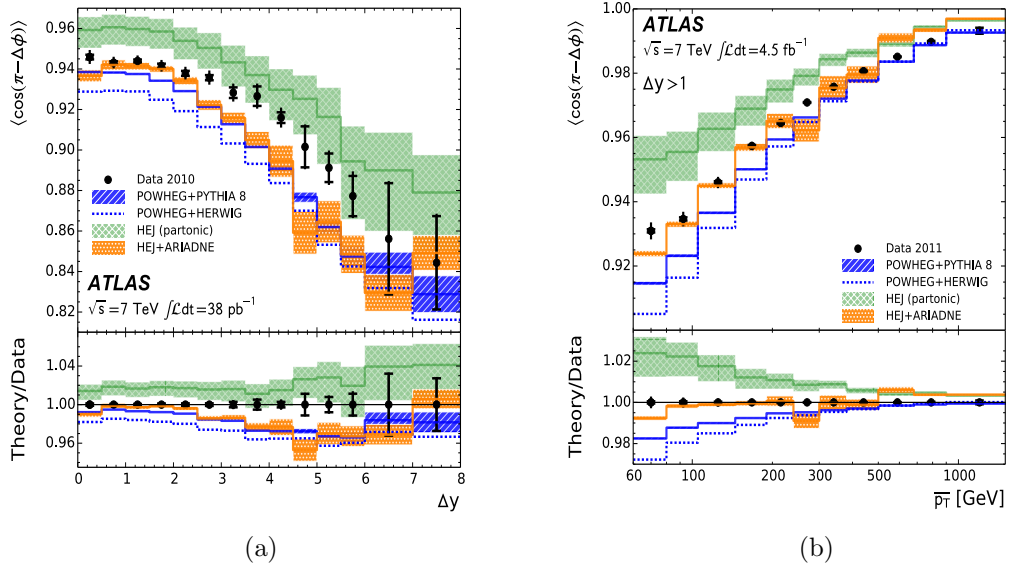


Figure 5.3

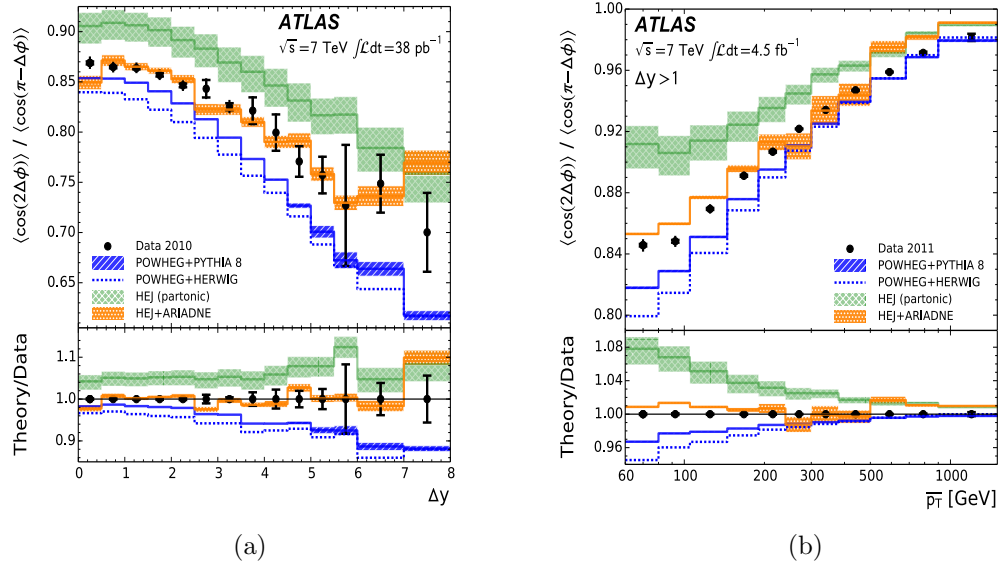


Figure 5.4

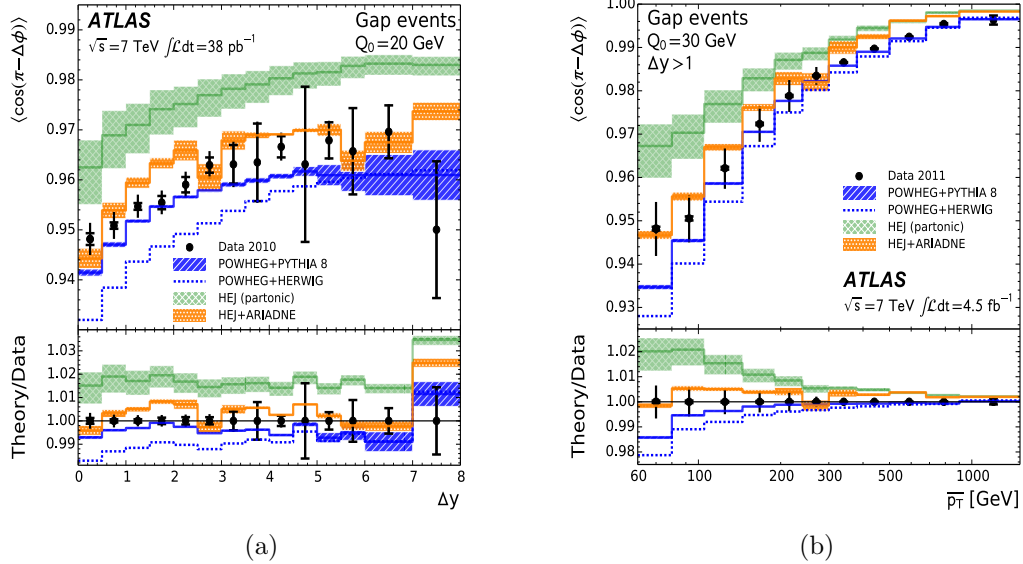


Figure 5.5

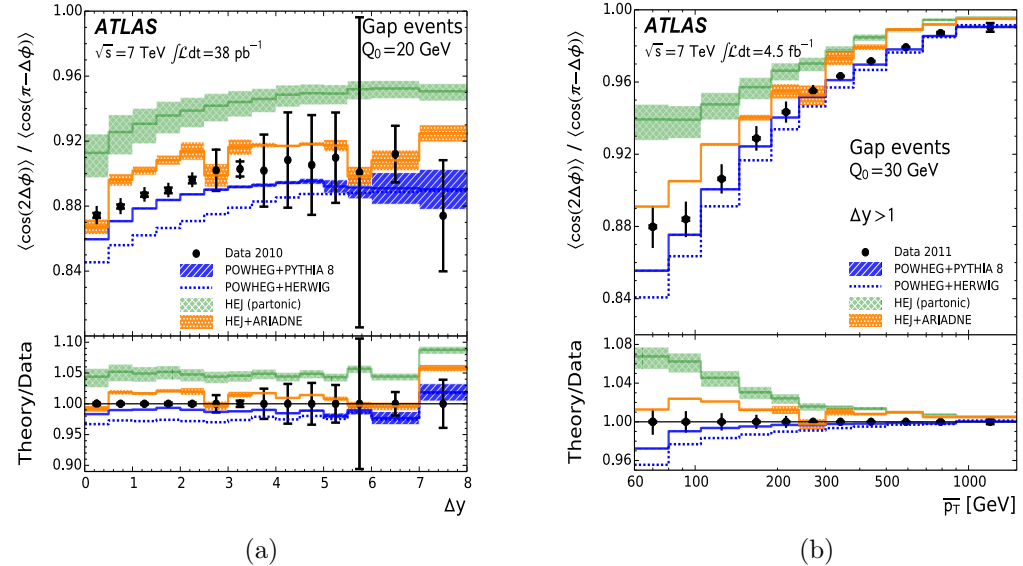


Figure 5.6

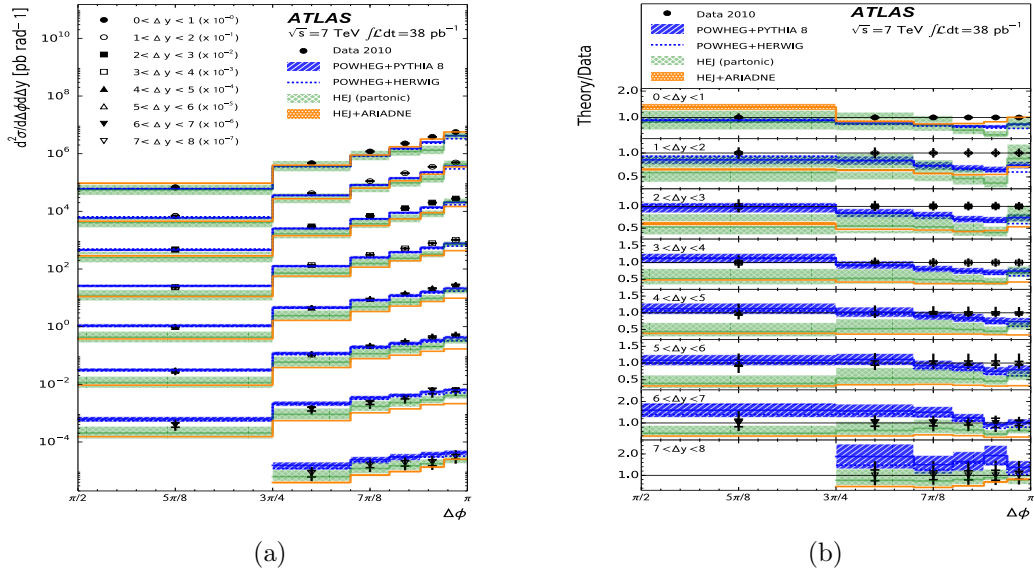


Figure 5.7

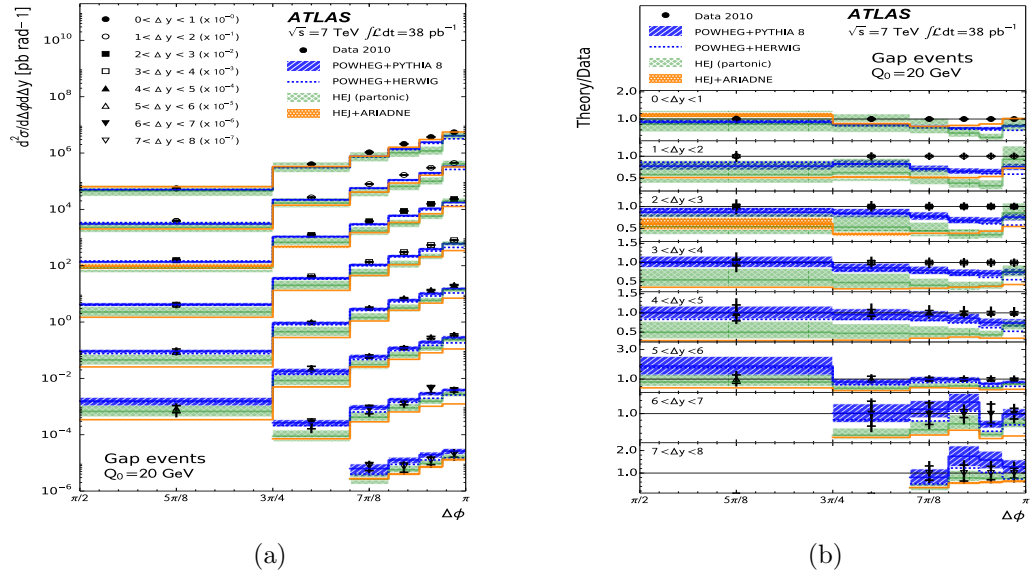


Figure 5.8

₁₃₃₇ **Chapter 6**

₁₃₃₈ **The W^\pm to Z/γ^* Ratio at ATLAS**

₁₃₃₉ Compare HEJ Z+Jets to NJet (NLO predictions) and MadGraph (LO predictions).

₁₃₄₀ ***Is this still worth it? Data/HEJ/MG all very unstable...***

¹³⁴¹ Chapter 7

¹³⁴² $Z/\gamma^* + \text{Jets}$ at 100TeV

- ¹³⁴³ • Talk about the FCC movement and the effect we expect the resummation will have at these energies.
- ¹³⁴⁴ • Put all three lines (30GeV, 60GeV, 100GeV) on the same plots in this section?
- ¹³⁴⁵ • Pros: Can see that we can put more stringent cuts while maintaining x-section.
- ¹³⁴⁶ Also makes the point that we can cut out all the NP physics we cant model.
- ¹³⁴⁷ • Cons: Plots will be very busy.

¹³⁴⁹ Figure (7.1) notes:

- ¹³⁵⁰ • dphi plot
- ¹³⁵¹ • Start with this one because its the most boring,
- ¹³⁵² • i.e. if QCD didnt change with energy scale all plots would be like this one

¹³⁵³ Figure (7.2) notes:

- ¹³⁵⁴ • njets,
- ¹³⁵⁵ • Explicitly shows that the break-down of the perturbative series gets worse at higher energies,
- ¹³⁵⁶ • The contributions from higher-order corrections increase as the energy increases,

¹³⁵⁸ Figure (7.3) notes:

- ¹³⁵⁹ • dy plot,
- ¹³⁶⁰ • O(10) increase in cross-section as we go to large rapidities,

- 1361 • More energy in initial state means we can get more jets further in to the outer
1362 regions of y-space,
1363 • The increase seen is *exactly* the large logs we capture at play

1364 Figure (7.4) notes:

- 1365 • $dm_j j$ plot,
1366 • $O(10)$ increase in cross-section as we go to large invariant masses,
1367 • Invariant masses again correlate with the logs we resum (show this explicitly if
1368 you havent already),
1369 • Similar to figure (7.3)

1370 Figure (7.5a-7.5c) notes:

- 1371 • pT distributions,
1372 • Heavy tails...soooo?
1373 • More energy in initial state means we can get more jets further in to the outer
1374 regions of y-space,
1375 • What effect would a shower have on these distributions? Plenty of spare pT to
1376 radiate.

1377 Figure (7.6a-7.6c) notes:

- 1378 • Not much more to say about these - mostly covered in dy plots,

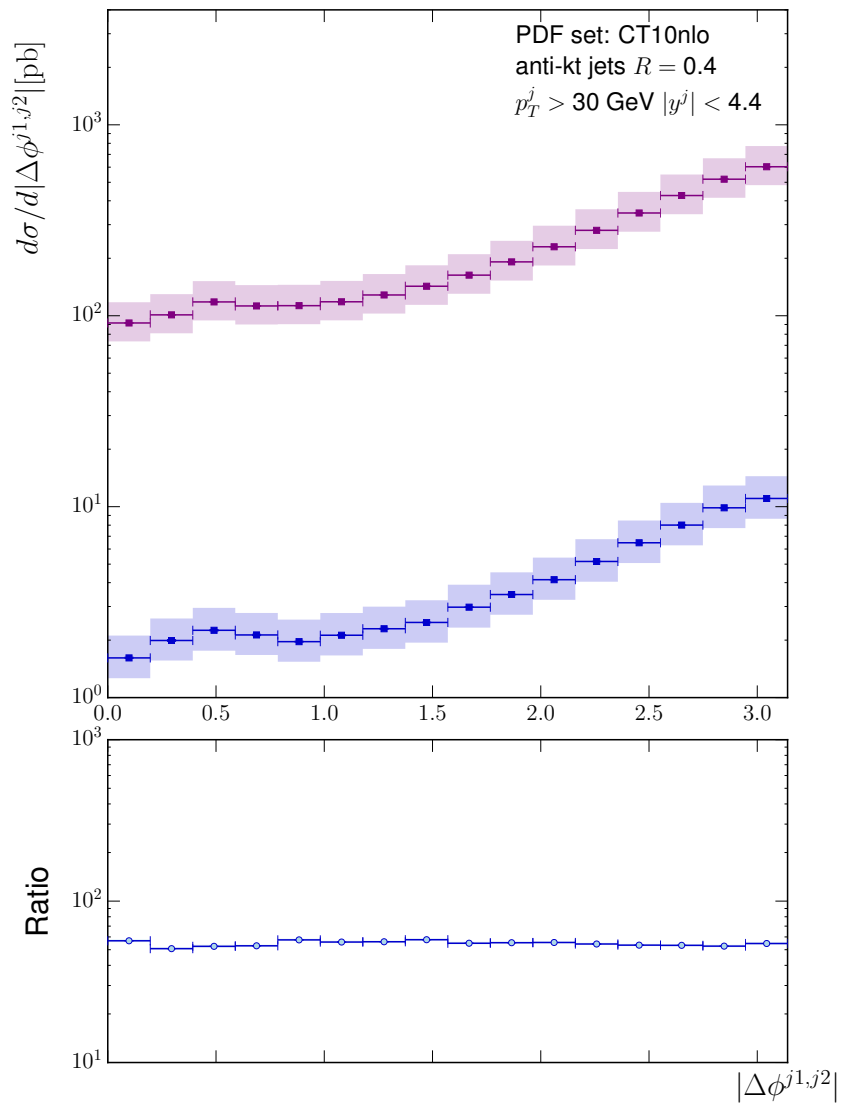


Figure 7.1: 12a

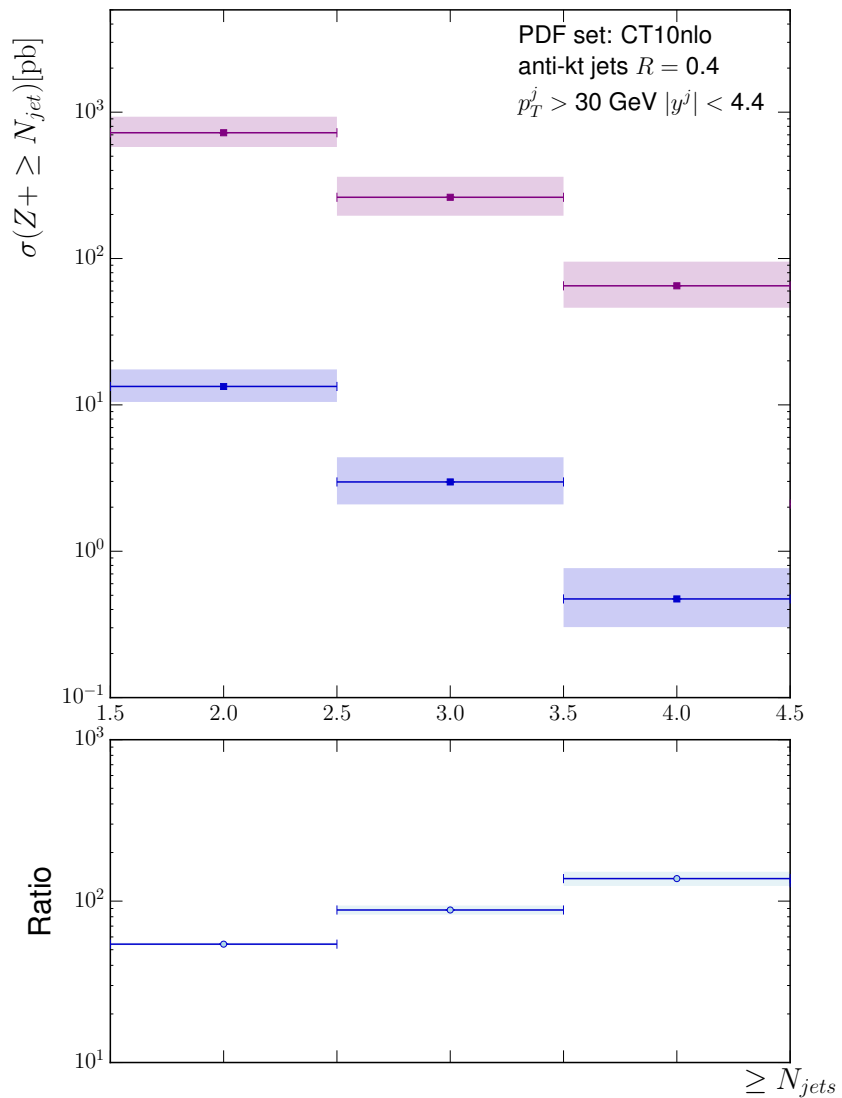


Figure 7.2: 12a

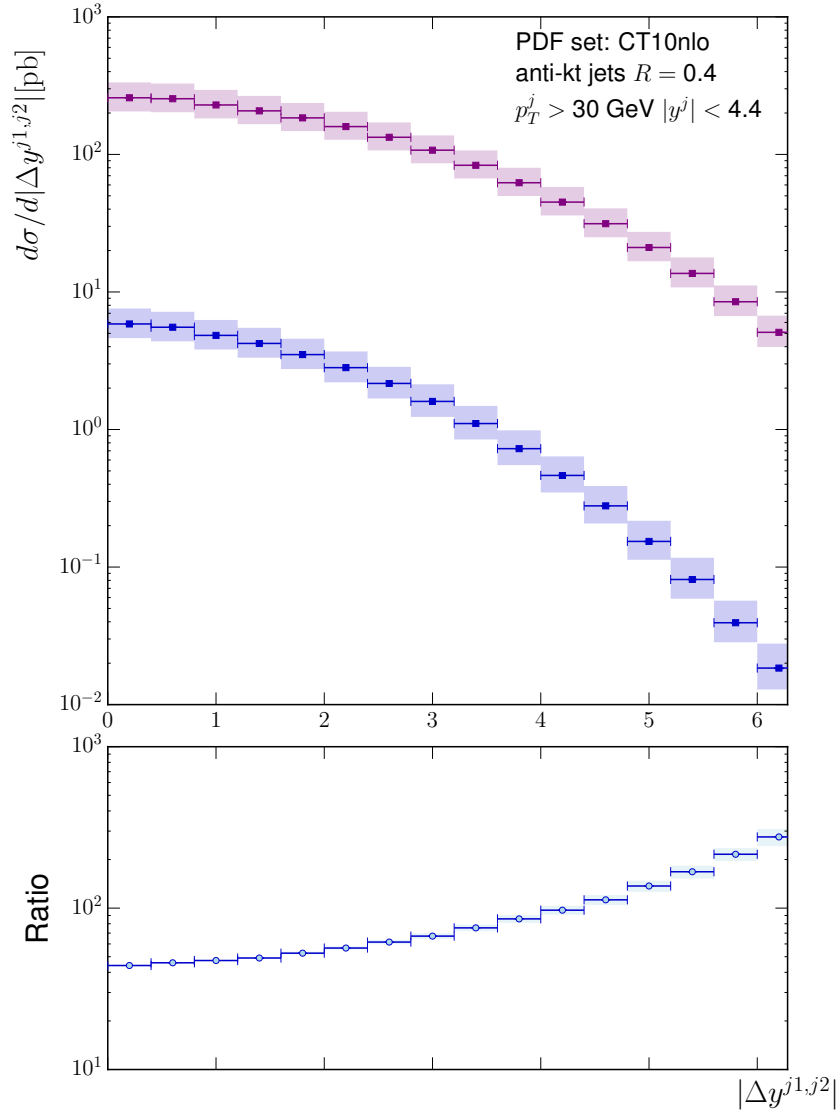


Figure 7.3: 11a

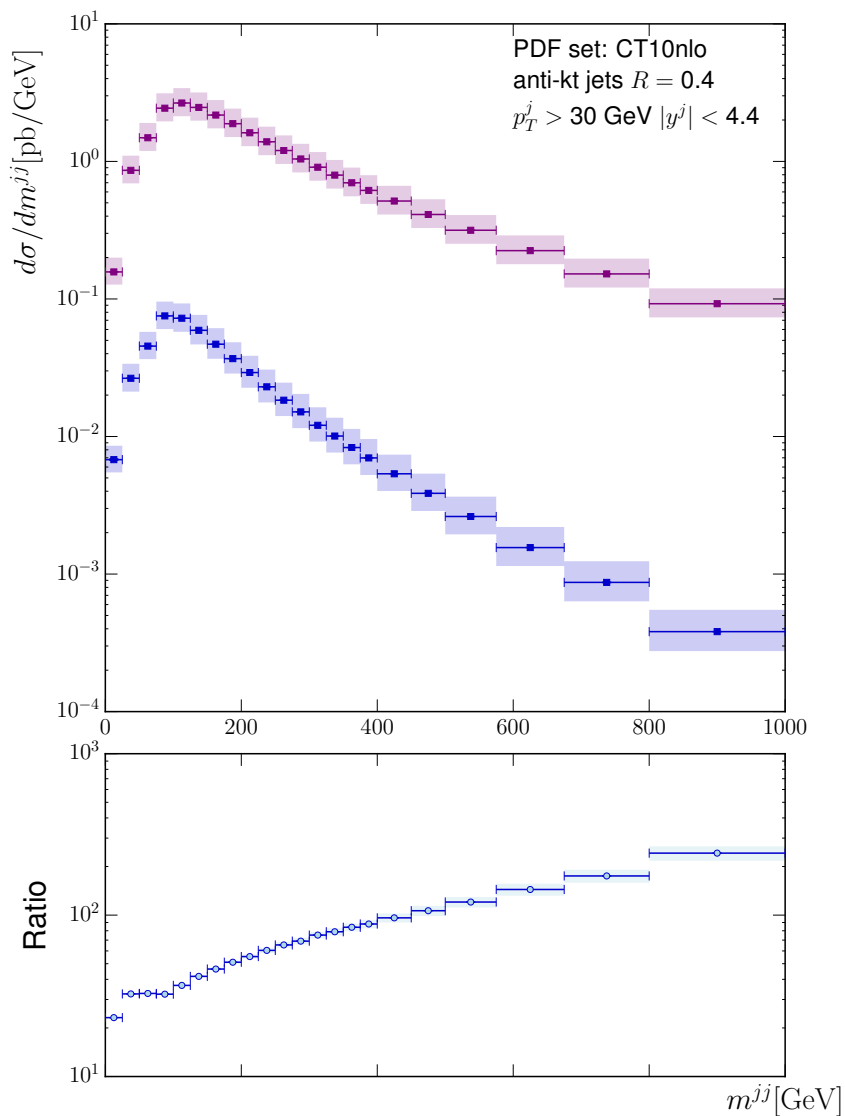
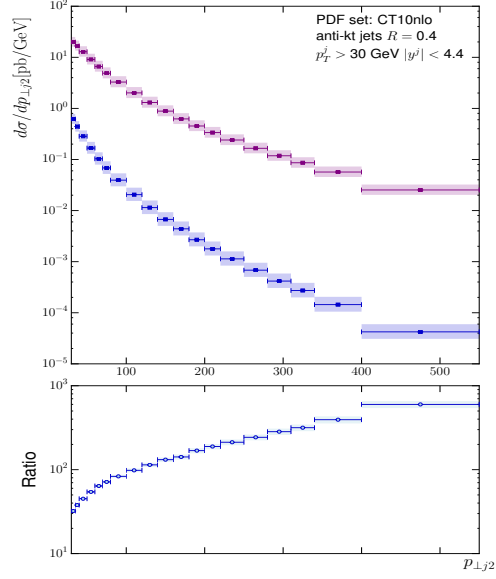
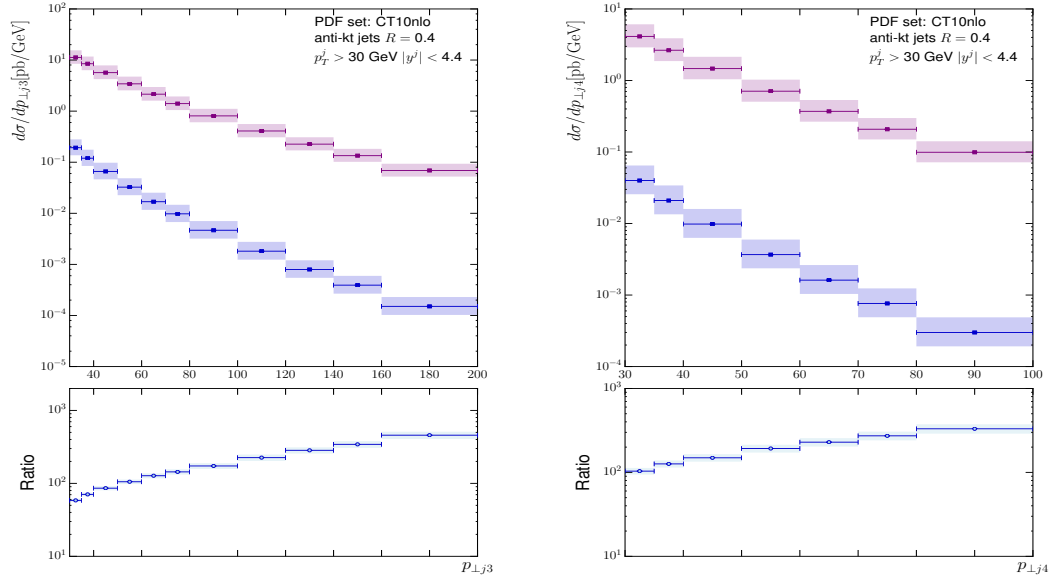


Figure 7.4: 11b



(a)



(b)

(c)

Figure 7.5

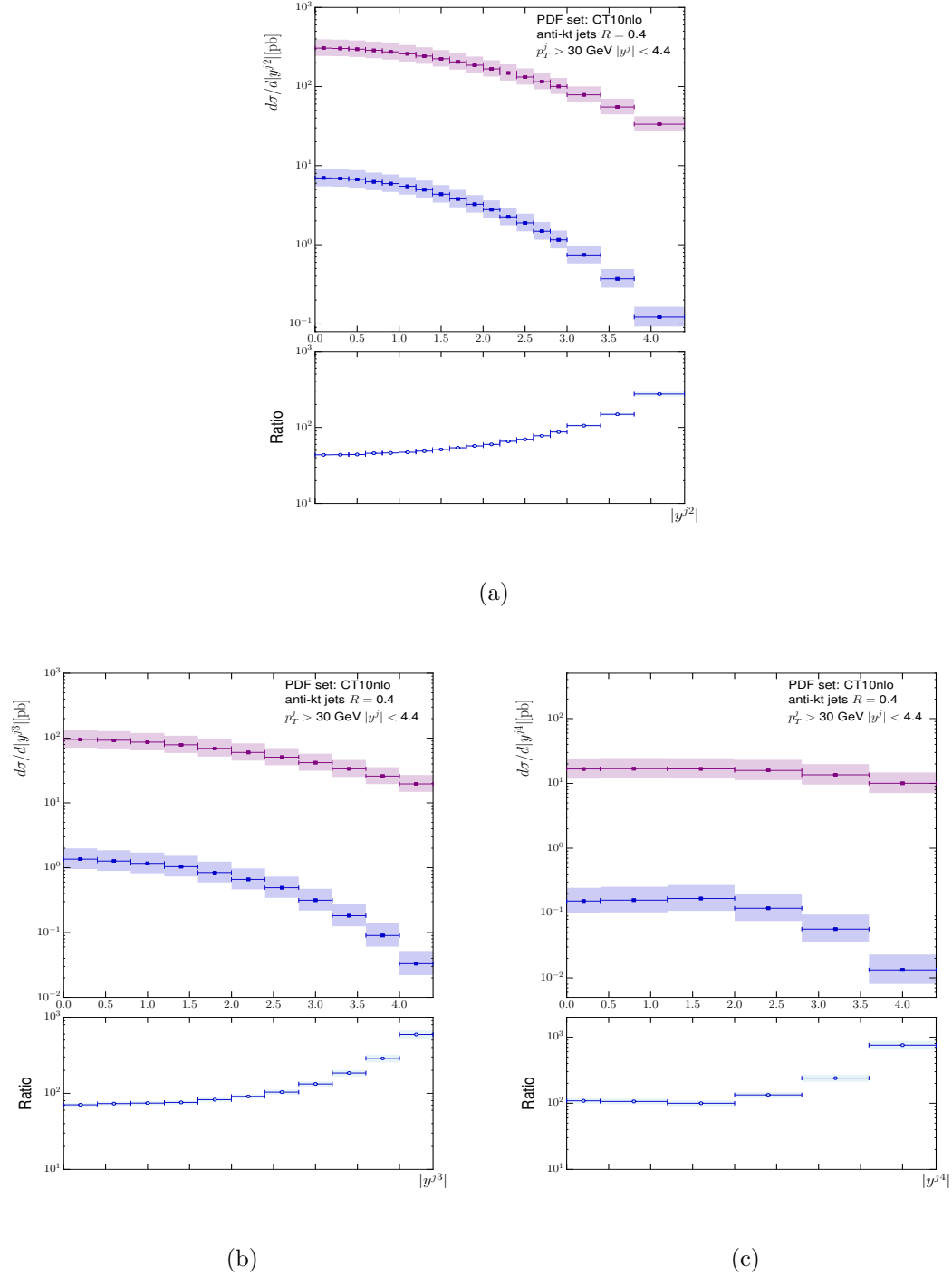


Figure 7.6

¹³⁷⁹ Chapter 8

¹³⁸⁰ Conclusions and Outlook

¹³⁸¹ **Appendix A**

¹³⁸² **The Faddeev-Popov Trick**

¹³⁸³ All that remains to be done is to evaluate the gluon propagator. As in QED when
¹³⁸⁴ trying to compute the propagator of a massless gauge boson we can use the work of
¹³⁸⁵ Faddeev and Popov. The functional integral we want to evaluate is in the form:

$$\int DA e^{-\frac{i}{4} \int d^4x F_{\mu\nu}^a F^{a\mu\nu}}. \quad (\text{A.1})$$

¹³⁸⁶ Where $DA = \prod_x \prod_{a,\mu} dA_\mu^a$. As briefly outlined above we would like to perform a
¹³⁸⁷ functional integration over all possible gauge choices and then pick out the subset of
¹³⁸⁸ gauges we are interested in by enforcing the gauge condition $G(A) = 0$ to eliminate
¹³⁸⁹ over-counting. This constraint may be written as [?]:

$$\int D\alpha(x) \delta(G(A^\alpha)) \text{Det} \left(\frac{\delta G(A^\alpha)}{\delta \alpha(x)} \right) = 1. \quad (\text{A.2})$$

¹³⁹⁰ Where $A_\mu^\alpha = A_\mu - \frac{1}{g_s} \partial_\mu \alpha(x)$. Making a gauge transformation ($A_\mu \rightarrow A_\mu^\alpha$) and inserting
¹³⁹¹ equation (18):

$$\int DA e^{-\frac{i}{4} \int d^4x F_{\mu\nu}^a F^{a\mu\nu}} = \int DA \int D\alpha(x) \delta(G(A^\alpha)) \text{Det} \left(\frac{\delta G(A^\alpha)}{\delta \alpha(x)} \right) e^{-\frac{i}{4} \int d^4x F_{\mu\nu}^a F^{a\mu\nu}}, \quad (\text{A.3a})$$

$$= \int D\alpha(x) \int DA \delta(G(A^\alpha)) \text{Det} \left(\frac{\delta G(A^\alpha)}{\delta \alpha(x)} \right) e^{-\frac{i}{4} \int d^4x F_{\mu\nu}^a F^{a\mu\nu}}. \quad (\text{A.3b})$$

¹³⁹² We are free to change the functional integration variable to A_μ^α since everything is gauge
¹³⁹³ invariant leading to an integrand which *only* depends on A_μ^α . We can therefore simply

1394 relabel back to A_μ :

$$= \left(\int D\alpha(x) \right) \int DA \delta(G(A)) \text{Det} \left(\frac{\delta G(A)}{\delta \alpha(x)} \right) e^{-\frac{i}{4} \int d^4x F_{\mu\nu}^a F^{a\mu\nu}}. \quad (\text{A.4})$$

1395 The functional integration can now just be factored out as a constant and we can choose
1396 the function $G(A)$ as a generalisation of the Lorentz gauge: $G(A) = \partial^\mu A_\mu^a - \omega^a$. This
1397 choice leads us to the correct gluon propagator - along with our free parameter, ξ :

$$\langle 0 | A_a(x) A_b(y) | 0 \rangle = G_F^{\mu\nu}(x-y) = \int \frac{d^4x}{(2\pi)^4} e^{-ik \cdot (x-y)} \delta_{ab} \frac{-i}{k^2 + i\epsilon} \left(g^{\mu\nu} - (1-\xi) \frac{k^\mu k^\nu}{k^2} \right). \quad (\text{A.5})$$

1398 but because the QCD gauge transformation is more involved than the QED equivalent
1399 the determinant term still depends on A_μ :

$$\text{Det} \left(\frac{\delta G(A)}{\delta \alpha(x)} \right) = \text{Det} \left(\frac{\partial_\mu D^\mu}{g_s} \right). \quad (\text{A.6})$$

1400 We can however simply invent another type of field and choose to write out determinant
1401 as

$$\text{Det} \left(\frac{\delta G(A)}{\delta \alpha(x)} \right) = \int D\chi D\bar{\chi} e^{i \int d^4x \bar{\chi} (-\partial_\mu D_\mu) \chi}. \quad (\text{A.7})$$

1402 These non-physical modes are called the Faddeev-Popov ghosts/anti-ghosts and are a
1403 consequence of enforcing gauge invariance - they are represented by the final term in
1404 equation (12a).

¹⁴⁰⁵ Bibliography

- 1406 [1] AAD, G., ET AL. Measurement of dijet production with a veto on additional central jet
1407 activity in pp collisions at $\sqrt{s} = 7$ TeV using the ATLAS detector. *JHEP 09* (2011), 053.
- 1408 [2] AAD, G., ET AL. Measurement of the production cross section for Z/γ^* in association
1409 with jets in pp collisions at $\sqrt{s} = 7$ TeV with the ATLAS detector. *Phys. Rev. D85* (2012),
1410 032009.
- 1411 [3] AAD, G., ET AL. Measurement of the production cross section of jets in association with
1412 a Z boson in pp collisions at $\sqrt{s} = 7$ TeV with the ATLAS detector. *JHEP 1307* (2013),
1413 032.
- 1414 [4] AAD, G., ET AL. A measurement of the ratio of the production cross sections for W and
1415 Z bosons in association with jets with the ATLAS detector. *Eur. Phys. J. C74*, 12 (2014),
1416 3168.
- 1417 [5] AAD, G., ET AL. Measurements of jet vetoes and azimuthal decorrelations in dijet events
1418 produced in pp collisions at $\sqrt{s} = 7$ TeV using the ATLAS detector. *Eur. Phys. J. C74*,
1419 11 (2014), 3117.
- 1420 [6] AAD, G., ET AL. Measurements of the W production cross sections in association with
1421 jets with the ATLAS detector. *Eur. Phys. J. C75*, 2 (2015), 82.
- 1422 [7] AAD, G., ET AL. Search for high-mass diboson resonances with boson-tagged jets in
1423 proton-proton collisions at $\sqrt{s} = 8$ TeV with the ATLAS detector. *JHEP 12* (2015), 055.
- 1424 [8] ABAZOV, V. M., ET AL. Studies of W boson plus jets production in $p\bar{p}$ collisions at
1425 $\sqrt{s} = 1.96$ TeV. *Phys. Rev. D88*, 9 (2013), 092001.
- 1426 [9] ALIOLI, S., NASON, P., OLEARI, C., AND RE, E. A general framework for implementing
1427 NLO calculations in shower Monte Carlo programs: the POWHEG BOX. *JHEP 06* (2010),
1428 043.
- 1429 [10] ALIOLI, S., NASON, P., OLEARI, C., AND RE, E. Vector boson plus one jet production
1430 in POWHEG. *JHEP 01* (2011), 095.
- 1431 [11] ALWALL, J., ET AL. Comparative study of various algorithms for the merging of parton
1432 showers and matrix elements in hadronic collisions. *Eur. Phys. J. C53* (2008), 473–500.
- 1433 [12] ALWALL, J., FREDERIX, R., FRIXIONE, S., HIRSCHI, V., MALTONI, F., MATTELAER,
1434 O., SHAO, H. S., STELZER, T., TORIELLI, P., AND ZARO, M. The automated
1435 computation of tree-level and next-to-leading order differential cross sections, and their
1436 matching to parton shower simulations. *JHEP 07* (2014), 079.
- 1437 [13] ALWALL, J., HERQUET, M., MALTONI, F., MATTELAER, O., AND STELZER, T.
1438 MadGraph 5 : Going Beyond. *JHEP 06* (2011), 128.

BIBLIOGRAPHY

- 1439 [14] ANDERSEN, J. R., LONNBLAD, L., AND SMILLIE, J. M. A Parton Shower for High Energy
1440 Jets. *JHEP* 07 (2011), 110.
- 1441 [15] ANDERSEN, J. R., AND SMILLIE, J. M. Constructing All-Order Corrections to Multi-Jet
1442 Rates. *JHEP* 1001 (2010), 039.
- 1443 [16] ANDERSEN, J. R., AND SMILLIE, J. M. The Factorisation of the t-channel Pole in Quark-
1444 Gluon Scattering. *Phys.Rev. D81* (2010), 114021.
- 1445 [17] ANDERSSON, B., MOHANTY, S., AND SODERBERG, F. Recent developments in the Lund
1446 model. In *36th Annual Winter School on Nuclear and Particle Physics (PINP 2002)*
1447 and *8th St. Petersburg School on Theoretical Physics St. Petersburg, Russia, February*
1448 *25-March 3, 2002* (2002).
- 1449 [18] BALITSKY, I., AND LIPATOV, L. The Pomeranchuk Singularity in Quantum
1450 Chromodynamics. *Sov.J.Nucl.Phys.* 28 (1978), 822–829.
- 1451 [19] BERGER, C. F., BERN, Z., DIXON, L. J., FEBRES CORDERO, F., FORDE, D.,
1452 GLEISBERG, T., ITA, H., KOSOWER, D. A., AND MAITRE, D. Next-to-Leading Order
1453 QCD Predictions for $Z, \gamma^* + 3$ -Jet Distributions at the Tevatron. *Phys. Rev. D82* (2010),
1454 074002.
- 1455 [20] BERINGER, J., ET AL. Review of Particle Physics (RPP). *Phys. Rev. D86* (2012), 010001.
- 1456 [21] BERN, Z., OZEREN, K., DIXON, L. J., HOECHE, S., FEBRES CORDERO, F., ITA, H.,
1457 KOSOWER, D., AND MAITRE, D. High multiplicity processes at NLO with BlackHat and
1458 Sherpa. *PoS LL2012* (2012), 018.
- 1459 [22] BUTTERWORTH, J. M., DAVISON, A. R., RUBIN, M., AND SALAM, G. P. Jet substructure
1460 as a new Higgs search channel at the LHC. *Phys. Rev. Lett.* 100 (2008), 242001.
- 1461 [23] CACCIARI, M., DREYER, F. A., KARLBERG, A., SALAM, G. P., AND ZANDERIGHI,
1462 G. Fully Differential Vector-Boson-Fusion Higgs Production at Next-to-Next-to-Leading
1463 Order. *Phys. Rev. Lett.* 115, 8 (2015), 082002.
- 1464 [24] CACCIARI, M., SALAM, G. P., AND SOYEZ, G. The Anti-k(t) jet clustering algorithm.
1465 *JHEP* 0804 (2008), 063.
- 1466 [25] CAMPBELL, J. M., ELLIS, R. K., NASON, P., AND ZANDERIGHI, G. W and Z bosons in
1467 association with two jets using the POWHEG method. *JHEP* 08 (2013), 005.
- 1468 [26] CAPORALE, F., IVANOV, D. Yu., MURDACA, B., AND PAPA, A. Mueller-Navelet small-
1469 cone jets at LHC in next-to-leading BFKL. *Nucl. Phys. B877* (2013), 73–94.
- 1470 [27] CHATRCHYAN, S., ET AL. Jet Production Rates in Association with W and Z Bosons in
1471 pp Collisions at $\sqrt{s} = 7$ TeV. *JHEP* 01 (2012), 010.
- 1472 [28] CHATRCHYAN, S., ET AL. Measurement of the inclusive production cross sections for
1473 forward jets and for dijet events with one forward and one central jet in pp collisions at
1474 $\sqrt{s} = 7$ TeV. *JHEP* 06 (2012), 036.
- 1475 [29] CHATRCHYAN, S., ET AL. Ratios of dijet production cross sections as a function of the
1476 absolute difference in rapidity between jets in proton-proton collisions at $\sqrt{s} = 7$ TeV.
1477 *Eur. Phys. J. C72* (2012), 2216.
- 1478 [30] CHATRCHYAN, S., ET AL. Event shapes and azimuthal correlations in $Z +$ jets events in
1479 pp collisions at $\sqrt{s} = 7$ TeV. *Phys. Lett. B722* (2013), 238–261.
- 1480 [31] CHATRCHYAN, S., ET AL. Measurement of the ratio of the inclusive 3-jet cross section to
1481 the inclusive 2-jet cross section in pp collisions at $\sqrt{s} = 7$ TeV and first determination of
1482 the strong coupling constant in the TeV range. *Eur. Phys. J. C73*, 10 (2013), 2604.

- 1483 [32] COLFERAI, D., SCHWENNSEN, F., SZYMANOWSKI, L., AND WALLON, S. Mueller Navelet
1484 jets at LHC - complete NLL BFKL calculation. *JHEP* **12** (2010), 026.
- 1485 [33] CORCELLA, G., KNOWLES, I. G., MARCHESEINI, G., MORETTI, S., ODAGIRI, K.,
1486 RICHARDSON, P., SEYMOUR, M. H., AND WEBBER, B. R. HERWIG 6: An Event
1487 generator for hadron emission reactions with interfering gluons (including supersymmetric
1488 processes). *JHEP* **01** (2001), 010.
- 1489 [34] DUCLOUE, B., SZYMANOWSKI, L., AND WALLON, S. Mueller-Navelet jets at LHC: the
1490 first complete NLL BFKL study. *PoS QNP2012* (2012), 165.
- 1491 [35] FIELD, R. *Applications of Perturbative Quantum Chromodynamics*. Addison Wesley
1492 Longman Publishing Co., 1989.
- 1493 [36] FREDERIX, R., FRIXIONE, S., PAPAEFSTATHIOU, A., PRESTEL, S., AND TORRIELLI, P.
1494 A study of multi-jet production in association with an electroweak vector boson.
- 1495 [37] FRIXIONE, S., NASON, P., AND OLEARI, C. Matching NLO QCD computations with
1496 Parton Shower simulations: the POWHEG method. *JHEP* **11** (2007), 070.
- 1497 [38] FRIXIONE, S., STOECKLI, F., TORRIELLI, P., WEBBER, B. R., AND WHITE, C. D. The
1498 MCaNLO 4.0 Event Generator.
- 1499 [39] FRIXIONE, S., AND WEBBER, B. R. Matching NLO QCD computations and parton
1500 shower simulations. *JHEP* **06** (2002), 029.
- 1501 [40] FROLOV, S., AND SLAVNOV, A. An invariant regularization of the standard model. *Physics
1502 Letters B* **309**, 3 (1993), 344 – 350.
- 1503 [41] GEHRMANN, T., GRAZZINI, M., KALLWEIT, S., MAIERHFER, P., VON MANTEUFFEL,
1504 A., POZZORINI, S., RATHLEV, D., AND TANCREDI, L. W^+W^- Production at Hadron
1505 Colliders in Next to Next to Leading Order QCD. *Phys. Rev. Lett.* **113**, 21 (2014), 212001.
- 1506 [42] GLEISBERG, T., HOECHE, S., KRAUSS, F., SCHONHERR, M., SCHUMANN, S., SIEGERT,
1507 F., AND WINTER, J. Event generation with SHERPA 1.1. *JHEP* **02** (2009), 007.
- 1508 [43] GRAZZINI, M., KALLWEIT, S., AND RATHLEV, D. W and Z production at the LHC in
1509 NNLO QCD. *JHEP* **07** (2015), 085.
- 1510 [44] GRIFFITHS, D. *Introduction to Elementary Particles*. Physics Textbook. Wiley, 2008.
- 1511 [45] HOECHE, S., KRAUSS, F., SCHONHERR, M., AND SIEGERT, F. QCD matrix elements +
1512 parton showers: The NLO case. *JHEP* **04** (2013), 027.
- 1513 [46] HCHE, S., KUTTIMALAI, S., SCHUMANN, S., AND SIEGERT, F. Beyond Standard Model
1514 calculations with Sherpa. *Eur. Phys. J. C* **75**, 3 (2015), 135.
- 1515 [47] ITA, H., BERN, Z., DIXON, L. J., FEBRES CORDERO, F., KOSOWER, D. A., AND
1516 MAITRE, D. Precise Predictions for Z + 4 Jets at Hadron Colliders. *Phys. Rev. D* **85**
1517 (2012), 031501.
- 1518 [48] JUNG, H., ET AL. The CCFM Monte Carlo generator CASCADE version 2.2.03. *Eur.
1519 Phys. J. C* **70** (2010), 1237–1249.
- 1520 [49] JUNG, H., AND SALAM, G. P. Hadronic final state predictions from CCFM: The Hadron
1521 level Monte Carlo generator CASCADE. *Eur. Phys. J. C* **19** (2001), 351–360.
- 1522 [50] KHACHATRYAN, V., ET AL. Measurement of electroweak production of two jets in
1523 association with a Z boson in proton-proton collisions at $\sqrt{s} = 8$ TeV. *Eur. Phys. J.
1524 C* **75**, 2 (2015), 66.

BIBLIOGRAPHY

- 1525 [51] KHACHATRYAN, V., ET AL. Measurements of jet multiplicity and differential production
1526 cross sections of $Z +$ jets events in proton-proton collisions at $\sqrt{s} = 7$ TeV. *Phys. Rev.*
1527 *D91*, 5 (2015), 052008.
- 1528 [52] KUIPERS, J., UEDA, T., VERMASEREN, J. A. M., AND VOLINGA, J. Form version 4.0.
1529 *CoRR abs/1203.6543* (2012).
- 1530 [53] KURAEV, E. A., LIPATOV, L. N., AND FADIN, V. S. Multi - Reggeon processes in the
1531 Yang-Mills theory. *Sov. Phys. JETP* 44 (1976), 443–450.
- 1532 [54] LAVESSON, N., AND LONNBLAD, L. W+jets matrix elements and the dipole cascade.
1533 *JHEP* 07 (2005), 054.
- 1534 [55] LONNBLAD, L. ARIADNE version 4: A Program for simulation of QCD cascades
1535 implementing the color dipole model. *Comput. Phys. Commun.* 71 (1992), 15–31.
- 1536 [56] MANGANO, M. L., MORETTI, M., PICCININI, F., PITTAU, R., AND POLOSA, A. D.
1537 ALPGEN, a generator for hard multiparton processes in hadronic collisions. *JHEP* 07
1538 (2003), 001.
- 1539 [57] MUTA, T. *Foundations Of Quantum Chromodynamics: An Introduction to Perturbative*
1540 *Methods in Gauge Theories*. World Scientific lecture notes in physics. World Scientific
1541 Publishing Company Incorporated, 2010.
- 1542 [58] NASON, P. A New method for combining NLO QCD with shower Monte Carlo algorithms.
1543 *JHEP* 11 (2004), 040.
- 1544 [59] PAULI, W., AND VILLARS, F. On the invariant regularization in relativistic quantum
1545 theory. *Rev. Mod. Phys.* 21 (Jul 1949), 434–444.
- 1546 [60] RE, E. NLO corrections merged with parton showers for $Z+2$ jets production using the
1547 POWHEG method. *JHEP* 10 (2012), 031.
- 1548 [61] SALAM, G. P., AND SOYEZ, G. A Practical Seedless Infrared-Safe Cone jet algorithm.
1549 *JHEP* 05 (2007), 086.
- 1550 [62] SJOSTRAND, T., EDEN, P., FRIBERG, C., LONNBLAD, L., MIU, G., MRENNA, S., AND
1551 NORRBIN, E. High-energy physics event generation with PYTHIA 6.1. *Comput. Phys.*
1552 *Commun.* 135 (2001), 238–259.
- 1553 [63] SJOSTRAND, T., MRENNA, S., AND SKANDS, P. Z. A Brief Introduction to PYTHIA 8.1.
1554 *Comput. Phys. Commun.* 178 (2008), 852–867.
- 1555 [64] STERMAN, G. F. Partons, factorization and resummation, TASI 95. In *QCD and beyond. Proceedings, Theoretical Advanced Study Institute in Elementary Particle Physics, TASI-95, Boulder, USA, June 4-30, 1995* (1995).

¹⁵⁵⁸ Publications

¹⁵⁵⁹

¹⁵⁶⁰ Author Name(s). Title of publication. In *Where Published*, Year.

¹⁵⁶¹

¹⁵⁶² Author Name(s). Title of publication. In *Where Published*, Year.

¹⁵⁶³